FACULTY OF ENGINEERING
AND ARCHITECTURE

Design and Control of a Hopping Robot with Series Clutched Actuators

Eline De Groote
Student number: 02007819

Supervisors: Prof. dr. ir. Guillaume Crevecoeur, Dr. ir. Frederik Ostyn

Master's dissertation submitted in order to obtain the academic degree of
Master of Science in Electromechanical Engineering - Control Engineering and Automation

Academic year 2024-2025

GHENT
UNIVERSITY

Design and Control of a Hopper Robot with Series Clutched Actuators

Prof. Dr. Ir Guillaume Crevecoeur, Dr. Ir. Frederik Ostyn, Eline De Groote

***Abstract*—Humanoid robots must be able to navigate complex, unstructured terrain, requiring actuators with high torque density and strong impact resilience, as well as robust control strategies for stable locomotion.**

This work presents the design and control of a planar hopping leg—mimicking a humanoid limb—using newly developed series clutched actuators. The goal is to create an underactuated 3-DOF leg with improved impact resilience and jumping performance compared to state-of-the-art systems.

The resulting 13.62 kg, 0.9 m leg integrates tailored transmission and sensing systems. A three-phase control strategy is used: PD control during flight, impedance control during buffering, and energy shaping during lift-off. Simulation and experimental validation reveal that linear rail friction significantly affects performance. A friction estimation experiment yielded a dimensionless jumping height of 1.28. Notably, the leg achieved a dimensionless stiffness of 14.25 under impedance control, indicating enhanced impact resilience.

I. INTRODUCTION

Multi-legged robots, such as humanoids and quadrupeds, are capable of navigating both structured and unstructured terrain thanks to their high maneuverability. This requires robust and precise control, combined with an optimized mechanical design. As a result, research on multi-legged robots spans multiple domains, including mechanical design, actuation, foot-ground interaction, and control algorithms. To test innovations in design and control, simplified monoped hoppers are often used as experimental platforms.

Control strategies include model based and learning based methods, as discussed in [1] . This thesis uses a model based energy shaping approach, as learning based techniques are more complex and beyond the scope of this work.

In hopper robot design, the primary goals are low weight, minimal link inertia, and high impact resilience. Co-locating the knee and hip actuators reduces inertia but requires a transmission system. Key research areas include actuator choice, transmission design, and sensor integration.

Conventional transmissions like belts and chains can introduce speed ripples and creep, reducing control accuracy. Alternatives such as five-bar mechanisms and cable drives address these issues [2], [3]. Ground contact sensing also varies widely, from simple contact switches to complex force-mapping systems [3]–[6].

Actuator selection focuses on backdrivability and torque density. Hydraulic drives offer both but are heavy and inefficient. Electromagnetic motors, used in series elastic actuators and quasi-direct drives [3], are lighter and more efficient. Series elastic actuators use high gear ratios to boost torque but reduce controllability, while quasi-direct drives increase motor air gap radius and use planetary gearboxes, though they pose scaling challenges for humanoids [7].

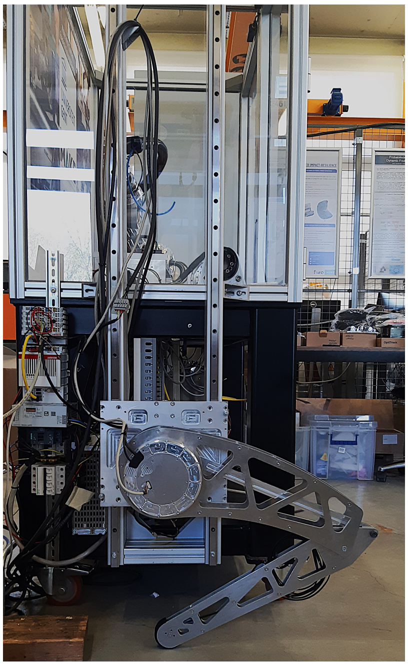

Fig. 1: Hopper setup

To address these challenges, Dr. Ir. Frederik Ostyn developed a series clutched actuator (Figure 2), which enhances torque density through a novel ring gear decoupling mechanism while preserving backdrivability.

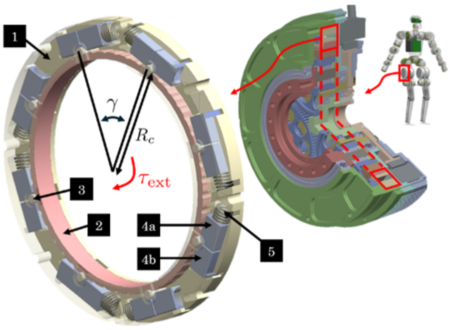

Fig. 2: Series clutched actuators [8]

This work evaluates these actuators in a planar 3-DOF hopper and investigates the following research questions:

How to design an underactuated hopping leg moving in the 2-DOF plane based on in-house developed series clutched actuators, and how can the resulting hopper be controlled? Is the resulting leg more impact-resilient, and can it jump higher than the state-of-the-art?

Reference benchmarks include dimensionless stiffness values (e.g., 10.8 in [4]) and dimensionless jump heights: 1.57 in [9], 1.14 in [10], and 2.4 in [7].

Section II describes the mechanical design, Section III details modeling and control, Section IV covers simulations, and Section V presents experimental validation.

II. DESIGN

This section details the design of the hopper robot, beginning with the design criteria and concluding with the real-life setup.

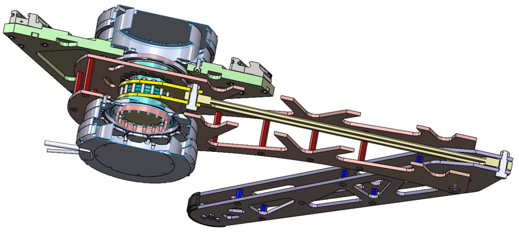

Fig. 3: Cross-section of hopper leg

A. Design Criteria

The hopper design was guided by three main criteria: low weight for jumping efficiency, minimal leg inertia, and sufficient structural robustness for impact forces. These often conflicting goals were addressed using FEM simulations in SolidWorks.

To support this analysis, force estimates were required. Early simulations ran in parallel with the design process and were used for ground reaction force estimations. Assuming a maximum jump height of 1.5 m, a maximum ground reaction force of approximately 750 N was used to evaluate critical components in the FEM analysis.

B. General Design Description

The hopper consists of three primary links: the hip base, the upper leg, and the lower leg.

The hip base, shown as the green plate in Figure 3, serves as the structural interface between the hopper and two linear rails via four low-friction guiding carriages. It also houses the hip actuator and includes provisions for mounting additional weights during testing, which may help evaluate actuator performance limits.

The upper leg, depicted in red in Figure 3, is connected to the hip actuator and holds the knee actuator on the same axis to reduce upper leg inertia. It is constructed from two laser-cut aluminum plates, reinforced with triangular bracing and standoffs for structural rigidity.

The upper leg encloses the transmission system, which comprises two rotating plates and a connecting rod. The plates are mounted to the knee actuator and spaced apart using spacers. A shoulder bolt connects the plates to the rotating rod, which is itself linked to the tip of the lower leg via another shoulder bolt. This configuration forms a mechanical lever about the knee axis, with the lever arm at the lower leg matching the radius of the rotating plates. This system, illustrated in yellow in Figure 3, was chosen for its rigid, fully mechanical linkage to ensure that impact loads are directly transferred to the actuators—an essential requirement for actuator performance evaluation.

The lower leg mirrors the structural concept of the upper leg: two aluminum plates with triangular bracing connected by standoffs. It also houses a sensing system located at the foot, consisting of three contact switches arranged 45° apart. This configuration ensures that one switch aligns with the y-axis and one with the x-axis. Simple contact switches were selected for their ability to detect ground contact without requiring complex mapping systems. A rubber layer covers the switches to protect them during impact.

C. Conclusions on Design

All components were successfully manufactured and assembled. The final hopper leg measures 0.9 m in length and weighs 13.62 kg, including the base plate and guiding carriages (see Table I). Despite its greater mass, the upper leg has a moment of inertia similar to the lower leg due to its center of mass being closer to the joint. The full assembly is shown in Figure 1.

TABLE I: Physical properties of the leg

Property	Value	Unit
Length	0.9	m
Total mass	13.62	kg
Length upper leg	0.45	m
Mass upper leg	5.382	kg
Inertia upper leg	0.1	kgm^2
CoM – joint upper leg	-40.36	mm
Length lower leg	0.45	m
Mass lower leg	0.96	kg
Inertia lower leg	0.06	kgm^2
CoM – joint lower leg	178.63	mm

III. MODELING AND CONTROL

This section presents the kinematic model and resulting equations of motion for the hopper robot, followed by a description of the control approach.

A. Model of the Hopper Robot

As detailed in Section II, the hopper moves along linear rails, with the vertical hip position as the first generalized coordinate. Combined with the hip and knee joint angles, the system has three degrees of freedom (Figure 4) and assumes each link has momentum only about the z-axis.

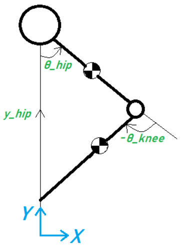

Fig. 4: Kinematic model of the hopper robot

Two distinct sets of equations of motion are applicable, depending on whether the hopper is in contact with the ground. During the flight phase, the hopper is treated as a free body (neglecting friction), whereas during the stance phase, ground reaction forces (GRFs) must be considered. The equations of motion for the two phases are given by:

$$\mathbf{M}\ddot{\mathbf{q}} + \mathbf{C}\dot{\mathbf{q}} + \mathbf{K}\mathbf{q} = \mathbf{0}, \quad \text{(Flight phase)}$$

$$\mathbf{M}\ddot{\mathbf{q}} + \mathbf{C}\dot{\mathbf{q}} + \mathbf{K}\mathbf{q} = \mathbf{J}_{foot}^{\mathrm{T}}\mathbf{F}_{\mathrm{GRF}}, \quad \text{(Stance phase)}$$

with $\mathbf{M} \in \mathbb{R}^{3\times3}$ the mass matrix, $\mathbf{C} \in \mathbb{R}^{3\times3}$ the damping matrix, $\mathbf{K} \in \mathbb{R}^{3\times3}$ the stiffness matrix, $\mathbf{J}_{foot} \in \mathbb{R}^{2\times3}$ the foot Jacobian, $\mathbf{q} \in \mathbb{R}^3$ the generalized coordinate and $\mathbf{F}_{GRF} \in \mathbb{R}^2$ the ground reaction force.

The needed model parameters are listed in Table I.

B. Control Algorithm

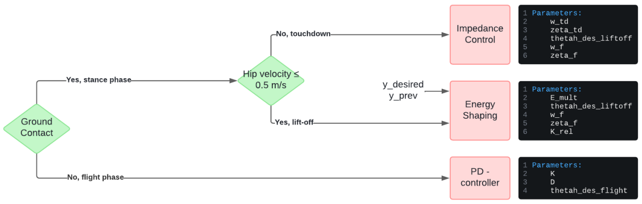

```
Parameters:
    w_td
    zeta_td
    thetah_des_liftoff
    w_f
    zeta_f
```

```
Parameters:
    E_mult
    thetah_des_liftoff
    w_f
    zeta_f
    K_rel
```

```
Parameters:
    K
    D
    thetah_des_flight
```

Fig. 5: Overview of the control algorithm

The control algorithm mirrors the structure of the model and divides the hopping cycle into multiple phases, each governed by a different control strategy. Two stance sub-phases are distinguished:

- Touchdown phase: From the moment of contact with the ground to the desired initial configuration for the next jump.
- Lift-off phase: From the end of the touchdown phase to the moment of take-off (loss of contact).

This segmentation is illustrated in Figure 5, which also highlights the switching criteria. Ground contact detection marks the transition from flight to stance, while the hip's velocity estimate determines the transition from touchdown to lift-off.

Figure 5 also summarizes the control strategies used in each phase, along with the key parameters to be evaluated in the simulations discussed in Section IV.

The energy shaping controller used during lift-off calculates the required torque based on the system's current energy, the desired jumping height, and the previous jump's performance. The two main parameters are the energy scaling factor $E_{\text{mult}} \in \mathbb{R}$ and the adaptive gain $K_{\text{rel}} \in \mathbb{R}$.

An impedance controller is applied both for regulating hip height (leg impedance control) and foot position (foot impedance control). This controller is based on a virtual massless spring-damper system and is characterized by the parameters of natural frequency ω and damping ratio ζ. These can be mapped to physical spring-damper coefficients as follows:

$$K = \omega^2 m_{\text{tot}} \in \mathbb{R}, \quad D = 2m_{\text{tot}}\omega\zeta \in \mathbb{R}$$

where m_{tot} is the total mass of the system.

IV. SIMULATIONS

This section presents the simulation framework used to achieve three primary objectives: (1) evaluating the performance of the proposed control algorithm, (2) studying the effects of various control parameters, and (3) determining whether the results suggest improved performance compared to state-of-the-art approaches.

A. Simulation Evaluation Criteria

To evaluate the control performance, several metrics are employed. The first is the Normalized Root Mean Squared Error (NRMSE) between the actual and desired jumping heights, calculated as:

$$NRMSE = \frac{\sqrt{\sum_{i=1}^{n}(y_{\text{desired},i} - y_{\text{actual},i})^2}}{\bar{y}_{\text{actual}}} \in \mathbb{R}$$

where $y_{\text{desired},i}$ and $y_{\text{actual},i}$ are the desired and actual jump heights at the i-th instance, and $\bar{y}_{\text{actual}}$ is the average of the actual heights. This non-dimensional metric provides a quantitative measure of deviation from the desired performance. The quality of control is classified according to the following NRMSE scale:

$$\begin{cases} NRMSE < 10\% & \text{Excellent} \\ 10\% \leq NRMSE < 20\% & \text{Good} \\ 20\% \leq NRMSE < 30\% & \text{Fair} \\ NRMSE \geq 30\% & \text{Poor} \end{cases}$$

In addition to NRMSE, a slipping criterion is introduced to assess stability. A simulation is considered unstable if either of the following occurs:

1) The robot makes ground contact with its knee.
2) The robot's foot exhibits vibration upon landing.

If either condition is observed, the controller and its associated parameter configuration are considered ineffective.

B. Impedance Control Simulation

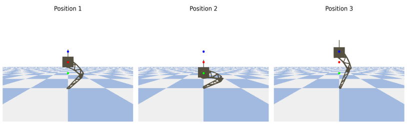

(a) GIF of trajectory following

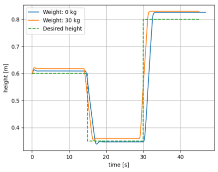

(b) Trajectory heights

Fig. 6: Impedance control simulation

The initial set of simulations focuses exclusively on impedance control in a trajectory-following scenario. A visual example of such a simulation is shown in Figure 6a. To evaluate robustness, the simulation was repeated with varying added masses placed on top of the hopper. As shown in Figure 6b, the results demonstrate that the impedance controller maintains robust performance under varying payloads, namely 0 kg and 30 kg.

To determine the maximum dimensionless stiffness, defined as $\bar{k} = \frac{kl}{mg}$ (with m the total mass, k the virtual leg stiffness, l the leg length and g the gravitational acceleration), the experiment was modified to focus solely on the final step of the trajectory with damping removed. By iteratively increasing the added mass until the leg could no longer complete the step, a maximum $\bar{k}$ value of 14.25 was obtained—surpassing values reported in existing literature.

C. Continuous Jumping Simulation

The full control algorithm was tested in a continuous jumping simulation to assess maximum achievable heights, robustness, and the influence of control parameters. A visualization of this simulation is provided in Figure 7a.

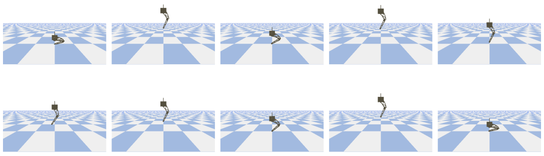

(a) Continuous jumping GIF

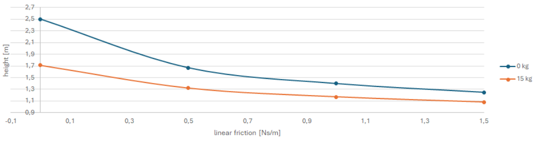

(b) Maximum jumping heights

Fig. 7: Continuous jumping simulation

The robustness of the control strategy with respect to friction was first evaluated. For well-tuned parameters and jumping heights below the maximum limit, very low NRMSE values were achieved (e.g., NRMSE = 0.00267). However, maximum jump height decreased with increasing friction and added mass, as shown in Figure 7b.

Next, the effects of various control parameters were analyzed. Simulations showed that:

- Larger hip starting angles (more bent postures) and smaller hip flight angles (straighter postures) allowed for higher jumps—consistent with human biomechanics.
- A smaller energy shaping parameter E_{mult} resulted in higher possible jumps due to the controller underestimating the current energy.
- A foot offset toward the knee provided more robust control than an offset in the opposite direction. This is due to the system's center of mass being located slightly toward the knee, making this configuration more balanced—again aligning with natural human jumping patterns.

The role of impedance control parameters (natural frequencies and damping ratios) was also studied for both touchdown and foot control. Observations included:

- Low frequencies resulted in slow responses.
- High frequencies induced oscillations.
- Low damping caused undamped oscillations.
- High damping led to overly slow responses.

To better interpret these effects, impedance control parameters were translated into a virtual spring-damper model using:

$$K_{td} = \omega_{td}^2 m_{\text{tot}}, \quad D_{td} = 2m_{\text{tot}}\omega_{td}\zeta_{td}$$

Simulations indicated that achieving higher jumps required greater virtual stiffness and stronger damping, reinforcing the intuitive notion that higher jumps demand greater muscular effort.

Finally, the dimensionless maximum jumping height, defined as $\bar{h} = \frac{\text{maximum jump height}}{\text{leg length}}$, was analyzed under varying levels of linear rail friction. For instance, under ideal (frictionless) conditions, a value of $\bar{h} = 2.8$ was achieved, whereas at a friction level of 1.5 Ns/m, $\bar{h}$ decreased to 1.5. These results highlight the sensitivity of jumping performance to rail friction. Further analysis of the linear rail friction value is required to determine whether the current hopper design can consistently outperform state-of-the-art systems. This analysis is given in Section V-A.

V. EXPERIMENTAL VALIDATION

To validate the system design and investigate improvements with respect to the state-of-the-art, multiple experiments were conducted. First, a simple position controller is applied to experimentally estimate the linear rail friction. Secondly, a second position control experiment was conducted with a limited velocity of 200°/s. This last simulation was also compared with its simulated counterpart. In both experiments, the hopper's base follows a predefined trajectory: starting from an almost fully bent position, moving to an almost fully extended position, transitioning to a squat-like posture, and finally returning to the initial bent configuration. This trajectory is illustrated in Figure 8.

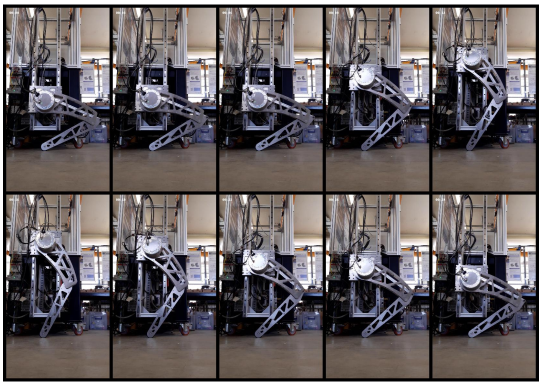

Fig. 8: Video screenshots of experiment 2

A. *Experiment 1: Estimation of linear rail friction value*

In the first experiment, a simple position control is applied, as shown in Figure 8 and described in the paragraph above. The data from the experiment is used to estimate the linear rail friction value.

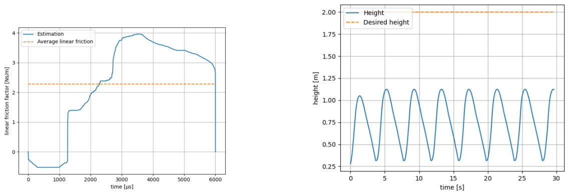

(a) Estimated linear friction values

(b) Corresponding jumping height

Fig. 9: Linear rail friction value estimation

Starting from the encoder data, a power balance is calculated:

$$P_{\text{act}} = P_{\text{jointFrictions}} + P_{\text{jointInertias}} + P_{\text{gravity}} + P_{\text{railFriction}}$$

with:

- $P_{\text{act}} = P_{hip} + P_{knee} = \tau_{hip} \cdot \dot{\theta}_{hip} + \tau_{knee} \cdot \dot{\theta}_{knee}$, the sum of the powers delivered by the two actuators
- $P_{\text{jointFrictions}} = c_{act} \cdot (\dot{\theta}_{hip}^2 + \dot{\theta}_{knee}^2)$, the sum of the lost power in the actuators due to joint friction, with $c_{act} = 5\,\text{Nms/rad}$ the joint friction
- $P_{\text{jointInertias}} = I_{act} \cdot (\ddot{\theta}_{hip} \cdot \dot{\theta}_{hip} + \ddot{\theta}_{knee} \cdot \dot{\theta}_{knee})$, the sum of the power going to the inertia of the actuators, with $I_{act} = 0.43\,\text{kgm}^2$
- $P_{\text{gravity}} = \frac{dE_{\text{grav}}}{dt}$, the power needed to change the hip base height from one gravitational potential energy to the next
- $P_{\text{railFriction}} = -b_{rail} \cdot v_{hip}^2$, the power lost to linear rail friction with b_{rail} the linear rail friction value

At every timestep, the linear friction value can be estimated using

$$b_{rail,i} = -\frac{P_{\text{act},i} - P_{\text{jointFrictions},i} - P_{\text{jointInertias},i} - P_{\text{gravity},i}}{v_{hip,i}^2}$$

when $v_{hip,i} \neq 0$ and using $b_{rail,i} = 0$ when $v_{hip,i} = 0$.

After applying smoothing techniques to reduce numerical noise, the estimated rail friction is plotted in Figure 9a. The average value is found to be $2.28\,\text{Ns/m}$, which is subsequently used in simulations to evaluate hopper performance. Using simulations, the newly estimated maximum jumping height is $1.15\,\text{m}$, as shown in Figure 9b, yielding a dimensionless jumping height $\bar{h} = \frac{1.15\,\text{m}}{0.9\,\text{m}} = 1.28$.

Compared to the state-of-the-art, this value is average: [7] reports $\bar{h} = 2.4$, [9] reports $\bar{h} = 1.57$, and [10] reports $\bar{h} = 1.14$.

The relatively high friction is likely due to early assembly choices: the linear rails were mounted with only two bolts, allowing midsection vibrations, and the cable routing was not optimized for dynamic motion, adding resistance.

B. *Experiment 2: Validation of improved dimensionless stiffness*

The second experiment is conducted to validate whether the improvement in dimensionless stiffness found in the simulations in Section IV-B is realistic. Due to the unavailability of large masses, a massless experiment is performed and compared with its simulated counterpart under identical conditions.

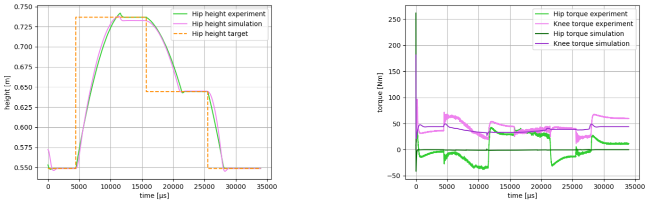

(a) Heights

(b) Torques

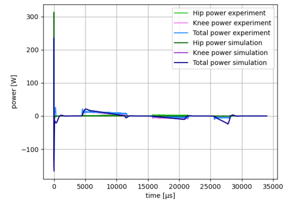

(c) Powers

Fig. 10: Comparison between simulation and experimental results

Figure 10 compares experimental and simulated results for joint torques, powers, and hip heights. While the simulation shows smoother torque transitions, both follow similar trends. Experimentally, torque is more evenly distributed between the hip and knee, whereas the simulation suggests a higher knee load—also reflected in the power profiles.

Although the simulated torques are slightly lower than those measured experimentally, this difference may be partially attributed to Coulomb friction present in the physical system, which was not explicitly modeled in the simulation. The simulation uses a viscous friction coefficient of 5 Nms/rad, which may not capture the full resistive forces encountered in the joints. The real system's frictional effects could result in higher measured torques, especially during low-speed or direction-changing phases of motion. Despite this, the total actuator power required in the experiment is found to be lower than in the simulation, suggesting that the real system may achieve similar or improved dimensionless stiffness values compared to the simulated model. These findings support the hypothesis that the newly developed actuators could offer enhanced performance relative to existing state-of-the-art solutions.

VI. FUTURE WORK

Future work could focus on improving the mechanical design for greater performance and robustness and completing experimental validation—especially for continuous jumping.

VII. CONCLUSION

This work presented the design and control of a hopper robot optimized for low mass and inertia using series clutched actuators. The resulting system demonstrated sufficient robustness for experimental testing.

A three-phase control strategy was proposed and evaluated through simulations, highlighting the impact of the different control parameters. Experimental validation showed a maximum dimensionless stiffness of 14.25, exceeding the state-of-the-art value of 10.8 [4], indicating enhanced impact resilience during touchdown.

Friction estimation experiments yielded a dimensionless jumping height of 1.28—comparable to existing designs (ranging from 1.14 to 2.4 [10], [7],[9]). Reducing linear rail friction could further improve performance. These results suggest the proposed hopper has potential to outperform current designs in both stiffness and jump height with further refinement.

ACKNOWLEDGMENTS

I would like to express my sincere gratitude to Dr. Ir. Frederik Ostyn, my research supervisor, for his continuous support, patient guidance, and insightful feedback throughout this project. His expertise and encouragement were invaluable in shaping the quality and direction of this work.

Special thanks to Prof. Dr. Ir. Guillaume Crevecoeur, my thesis promotor, for his support, approachability, and for providing both the opportunity and funding to conduct research in Bremen.

I am also grateful to the Underactuated Lab at DFKI Bremen for their warm welcome and collaborative environment. My sincere thanks to Ir. Shubham Vyas and Dr. Ir. Dennis Mronga for their direct supervision and support, and to Ir. Franek Stark and Ir. Jonas Haack for the great teamwork during my stay.

REFERENCES

[1] R. Soni, D. Harnack, H. Isermann, S. Fushimi, S. Kumar, and F. Kirchner, "End-to-End Reinforcement Learning for Torque Based Variable Height Hopping," in *2023 IEEE/RSJ International Conference on Intelligent Robots and Systems (IROS)*, Detroit, MI, USA: IEEE, Oct. 1, 2023, pp. 7531–7538. (visited on 10/01/2024).

[2] J. Hwangbo, V. Tsounis, H. Kolvenbach, and M. Hutter, "Cable-Driven Actuation for Highly Dynamic Robotic Systems," in *2018 IEEE/RSJ International Conference on Intelligent Robots and Systems (IROS)*, Madrid: IEEE, Oct. 2018, pp. 8543–8550. (visited on 10/01/2024).

[3] J. He and F. Gao, "Mechanism, Actuation, Perception, and Control of Highly Dynamic Multilegged Robots: A Review," *Chinese Journal of Mechanical Engineering*, vol. 33, no. 1, p. 79, Dec. 2020. (visited on 11/11/2024).

[4] F. Grimminger, A. Meduri, M. Khadiv, *et al.*, "An Open Torque-Controlled Modular Robot Architecture for Legged Locomotion Research," *IEEE Robotics and Automation Letters*, vol. 5, no. 2, pp. 3650–3657, Apr. 2020. (visited on 10/01/2024).

[5] M. Y. Chuah and S. Kim, "Enabling Force Sensing During Ground Locomotion: A Bio-Inspired, Multi-Axis, Composite Force Sensor Using Discrete Pressure Mapping," *IEEE Sensors Journal*, vol. 14, no. 5, pp. 1693–1703, May 2014. (visited on 11/16/2024).

[6] J. Ramos, B. Katz, M. Y. M. Chuah, and S. Kim, "Facilitating Model-Based Control Through Software-Hardware Co-Design," in *2018 IEEE International Conference on Robotics and Automation (ICRA)*, Brisbane, QLD: IEEE, May 2018, pp. 566–572. (visited on 10/02/2024).

[7] Y. Ding and H.-W. Park, "Design and experimental implementation of a quasi-direct-drive leg for optimized jumping," in *2017 IEEE/RSJ International Conference on Intelligent Robots and Systems (IROS)*, Vancouver, BC: IEEE, Sep. 2017, pp. 300–305. (visited on 10/01/2024).

[8] F. Ostyn, "Impact-Resilient High Performance Robot Actuators via Lightweight Overload Clutch Design with Wedged Rollers," in *2024 IEEE-RAS 23rd International Conference on Humanoid Robots (Humanoids)*, Nancy, France: IEEE, Nov. 22, 2024, pp. 32–36. (visited on 12/13/2024).

[9] J. Zhang, M. Li, J. Cao, Y. Dou, and X. Xiong, "Research on Bionic Jumping and Soft Landing of Single Leg System in Quadruped Robot," *Journal of Bionic Engineering*, vol. 20, no. 5, pp. 2088–2107, Sep. 2023. (visited on 10/01/2024).

[10] A. Khakpour Komarsofla, E. Azadi Yazdi, and M. Eghtesad, "Dynamic Modeling and Control of a Novel One-Legged Hopping Robot," *Robotica*, vol. 39, no. 9, pp. 1692–1710, Sep. 2021. (visited on 10/25/2024).

Contents

Acknowledgments

I would like to express my deepest gratitude to Dr. Ir. Frederik Ostyn, my research supervisor, for his unwavering support, patient guidance, and insightful feedback throughout every stage of this research. His passion for the subject and commitment to academic excellence have been both inspiring and instrumental in shaping the direction and quality of this work. I have greatly benefited from his deep expertise and thoughtful critiques, which consistently challenged me to refine my ideas and improve my writing.

I would like to extend my sincere thanks to Prof. Dr. Ir. Guillaume Crevecoeur, my thesis promotor, for his availability, kindness, and willingness to engage in thoughtful discussions throughout this process. I am especially grateful to him for the opportunity to go to Bremen and for the funding that made it possible.

I am also sincerely grateful to the team at the Underactuated Lab at the Deutsches Forschungszentrum für Künstliche Intelligenz (DFKI) in Bremen for their warm hospitality and for fostering a dynamic and collaborative research environment during my stay. Their support, constructive feedback, and openness to interdisciplinary exchange significantly enriched my research experience and broadened my perspective. In particular, I would like to thank Ir. Shubham Vyas and Dr. Ir. Dennis Mronga, my direct supervisors during the research internship, for their guidance and encouragement. I am also thankful to Ir. Franek Stark and Ir. Jonas Haack for the enjoyable and productive teamwork.

Lastly, I would like to thank the technicians of the 131 building, namely Vincent and Tony, for their help and for the fast and high-quality production of the components for the hopper robot.

Chapter 1

Introduction

Multi-legged robots are capable of navigating both structured and unstructured terrain due to their high maneuverability. Unlike wheeled and tracked robots, they can traverse obstacles and operate in challenging environments. However, their ability to execute complex movements requires robust, dynamic, and precise control, along with an optimized design. Therefore, research on multi-legged robots spans multiple domains, including design, mechanics, foot-ground interaction, and control algorithms.

Two primary control methodologies exist: model based control methods and learning based approaches [1, 2, 3]. Another essential focus of study is actuator design, as legged robots require actuators with high torque density, impact resilience, and efficient torque and motion transmission [4, 5, 6, 7, 8]. Research on contact sensing further explores how sensor feedback enhances control strategies [9].

Many research projects employ a monoped experimental setup to validate their design and control strategies. This allows researchers to, for example, experimentally assess newly developed actuators or validate control algorithms. In this context, Dr. Ir. Frederik Ostyn developed series clutched actuators with high impact resilience and large output torques, intended for future use in humanoid robots. Before deployment in a full humanoid system, these actuators are evaluated in a hopper setup in this master's thesis and compared with the state-of-the-art.

The following sections will provide an in-depth discussion of the current knowledge and methodologies for studying multi-legged robots, with a particular focus on the design, modeling, and control of a single humanoid robot leg, as this is most relevant for this work.

1.1 Design in legged robots

The design of a humanoid leg should satisfy multiple requirements. First, the leg should be easy to control. Secondly, the combination of the actuator and transmission system must be strong enough to perform the hopping motions and to withstand impact. Next, the leg should be as light as possible and the inertia of both parts of the leg should be as low as possible.

A common method to achieve low inertia is by centralizing most of the weight close to the joints. An obvious choice is therefore to put both the knee-actuator and the hip-actuator on the same axis. This necessitates the use of a transmission system. Although this transmission system adds complexity to the system, this design choice seems to be used in most quadruped and humanoid leg designs, as exemplified by [5, 10, 6, 11, 9].

To meet the aforementioned characteristics, design of legged robots involves key considerations related to actuation, transmission systems and sensors. The following chapters summarize the current state-of-the-art in each of these areas.

1.1.1 Actuation

Legged robots often demonstrate high-speed locomotion, which involves high accelerations and excessive loading on the actuators, resulting from the ground-leg interaction. In many applications, this ground interaction is unexpected due to inaccurate state estimations. Therefore, the actuators should demonstrate high robustness against impacts, meaning high backdrivability, and accurate controllability. In addition, high torque density and transmission transparency are desired. To achieve this, multiple combinations of actuators and transmission systems can be used [6, 4, 7, 5, 8, 12]. This section lists the most common actuator types, and the next section explains different types of transmission.

With high torque density and high backdrivability considered as the most important requirements, multiple types of actuators have been developed. In particular, three main types of actuation are used for dynamic locomotion in legged robots, namely hydraulic actuation, quasi-direct drives and serial elastic actuation. [12]

Hydraulic actuators can provide extremely high power density and are robust against impulsive loads. The robustness to impulsive loads follows from the energy of the impulse being absorbed by the hydraulic oil. In addition, this hydraulic oil allows accurate force controllability due to the high-frequency servo valves with precise pressure sensors. However, hydraulic actuators tend to be used in large and heavy robots, which is not the type of robot that will be studied in this thesis. Furthermore, hydraulic actuators can be less energetically efficient than electrical actuators due to the fluid viscous loss and internal leakage of the valves.[12]

A second actuation method is using electromagnetic (EM) actuators in direct drives. However, these actuators have a very low torque density. Although torque density could be increased by increasing reduction ratio of gears, this is often avoided due to the effects of this increased reduction ratio on the backdrivability of the actuator. Both the quasi-direct drive and series elastic actuation compensate this low torque output while still using electromagnetic motors. [12, 6, 7]

In serial elastic actuation the compensation is implemented by adding series elasticity to the conventional systems where a high gear reduction is used to create a low speed/ high torque characteristic. This method introduces a force-controllable actuator with low impedance and low friction, thus allowing high-quality force control. Additionally, the elastic element can be used to store energy and increase peak power when the servo motor and elastic element deliver power in the same direction. However, the implementation of serial elastic actuation turns torque control into position control. This position control has a limited bandwidth and comes with a substantial amount of delay as a result of the elasticity. [12]

Similarly to the serial elastic actuators, quasi-direct drive (QDD) actuators aim to improve the torque density of direct driving systems using electromagnetic actuators. In the context of the research on the MIT Cheetah actuators, it was found that electromagnetic motors with a large air gap radius allow a high torque output. This linear relation between air gap radius and torque output can be used in the actuators of legged robots as it leads to a lower required reduction in gear-ratio. The resulting actuator design is called a quasi-direct drive actuator, and it allows transparent transmission, good backdrivability and a high torque output. Therefore, multiple researches have studied the best combinations between motor choice and gear reduction choice for their legged robot applications. Though effective for small quadrupeds, scaling quasi-direct drive actuators to larger humanoid robots presents challenges, particularly in achieving sufficient torque while maintaining backdrivability and energy efficiency. [12, 6, 7, 4]

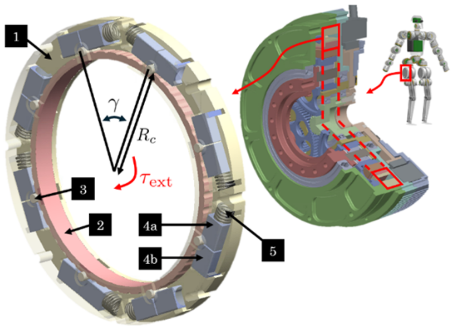

Figure 1.1: Series clutched actuators

Inspired by the quasi-direct drive actuators, Dr. Ir. Frederik Ostyn developed series clutched actuators, which integrate a planetary gearbox similar to the ones used in quasi-direct drives. However, the usually stationary ring of the planetary gear box is connected to a decoupling system which decouples when the output torque exceeds a certain threshold torque. This innovation, presented in Figure 1.1, enables higher gear ratios without compromising for the safety of the gears, making it a promising solution for humanoid robots. [8].

In this thesis, these series clutched actuators will be tested in a monoped hopper setup, evaluating their performance as hip and knee actuators in hopping scenarios.

1.1.2 Motion transmission

The efficiency of the hopper movement depends not only on the chosen actuators, but also on the method of transmission of torque and motion. Commonly used transmission methods are harmonic drives, planetary gears, belts and chains, etc. Some of the listed methods are already incorporated in actuator designs. However, transmission is also needed to transfer the torque and motion from the knee actuator, located at the hip, to the knee joint. This chapter covers different possibilities for the actuator-joint transmission and compares them with each other.

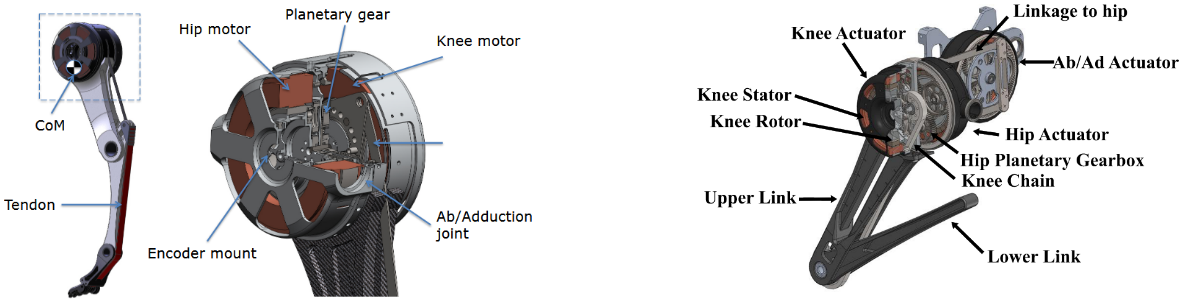

(a) Link transmission MIT Cheetah [6]

(b) Chain transmission MIT Cheetah 3 [10]

(c) Belt transmission hopper DFKI [2]

(d) Cable transmission system [5]

Figure 1.2: Transmission systems

The first option is a five-bar parallel kinematic system that mimics the main kinematic features of the mammalian leg [6, 12]. An example of this is shown in Figure 1.2a. The main advantage of this structure, which is also called a pantograph mechanism, is that it can maintain the relative angular orientation between the actuator and the lower leg segments, allowing very precise control. However, the pantograph also has drawbacks, such as limited angular movement and the weight of the link.

Secondly, chain drives can be used, as depicted in Figure 1.2b. An example of a robot using this, is the MIT Cheetah 3 [10]. Compared to the linkage system, the chain drive provides more angular freedom for the lower leg. However, the chain introduces some speed ripple at the lower link and adds impedance between the actuator and the lower link making control more challenging.

Similar to chain drives, belt drives can be used, as is for example the case in [9]. Another example of the use of belt drives is illustrated in Figure 1.2c. Although belts are lighter than chains, they are more likely to slip and suffer from creep, making control less accurate [5].

To avoid belt slippage and creep, a cable pulley system can be used as presented in [5]. The proposed system is demonstrated in Figure 1.2d. The cable pulley system combines the light-weight properties of belts with the non-slipping property of the stiff rod, while still having a large motion range. A disadvantage of the cable pulley-system proposed in [5] is its size because of the relatively large pulleys required for transmission.

All the aforementioned transmission systems are noncompliant. However, multiple researches also focus on incorporating flexible elements in the transmission design. Flexible elements can be added in the joints, such as in serial elastic actuators, or in the mechanical structures. Such designs are often inspired by the bi-articular muscles in animals [13]. The introduced leg compliance facilitates long-distance running and improves energy efficiency as the compliant elements are used for shock absorption and soft landings [12]. Furthermore, the elastic elements can be used to store energy at the moment of impact as is the case in serial elastic actuators.

1.1.3 Sensors

Accurate control of robots with legs requires feedback from the sensors employed in the robot. The most common sensors in multi-legged robots are encoders, which are necessary for position and velocity measurements. Furthermore, current or torque sensors are often used for feedback in torque control. Both encoders and current or torque sensors can be integrated into actuator designs, as exemplified by [8].

Additionally, sensors for ground detection or for ground reaction force measurements are often used in legged robots. In some researches, those sensors are added to the ground plate in the setup to evaluate a self designed force sensing mechanism or force estimations [14]. The choice of contact detection sensor will have an influence on the controller and on the design of the hopper foot.

First, force sensors, which can measure forces in both normal and tangential directions, can be employed for ground detection. These sensors can be utilized at the bottom of the foot or connected to the metal structures in the leg in the form of strain gauges. However, those sensors at the end of the leg increase inertia due to their mass and are very prone to inertial noise as a result of the highly dynamic movements of hopper robots.[15]

More simple options, which can only measure contact in one direction, are force sensing resistors and contact switches. However, force-sensing resistors tend to fail under large contact forces, so these sensors still need a relatively thick layer of protection. This thick layer of protection increases inertia of the lower leg, which is not desired in legged robots. [16] solved the issue of force sensors by using the more robust contact switches.

As a result of the limiting factors of conventional sensing systems, some more complex sensing mechanisms are designed. [14] designed a foot contact switch with a sensing rate of 270° utilizing a LED, a light sensor and a spring-loaded aperture. The resulting system, illustrated in Figure 1.3a, has a mass of 10 g and detects reliably at 3 Nm within 3 ms of contact.

[9] proposes the use of four piezo-resistive sensors all oriented at a 45 degrees angle from the vertical. Additionally, the sensors are embedded in a rubber sphere to protect them. Inside this sphere, the four sensors are oriented tangential to the surface of the sphere for optimal contact detection. The result is shown in Figure 1.3b.

Lastly, in [15] a more complex force sensing foot is designed for quadrupeds in which a matrix of pressure sensors is embedded in a layer of polyurethane rubber to achieve force mapping. The use of the pressure sensors in combination with the rubber allows high sensitivity and accurate measurements up to 300 N in the y-axis and 80 N in the x- and z-axis. The concept is displayed in Figure 1.3c.

Aside from using sensors for ground contact detection, ground can also be detected by torque sensors

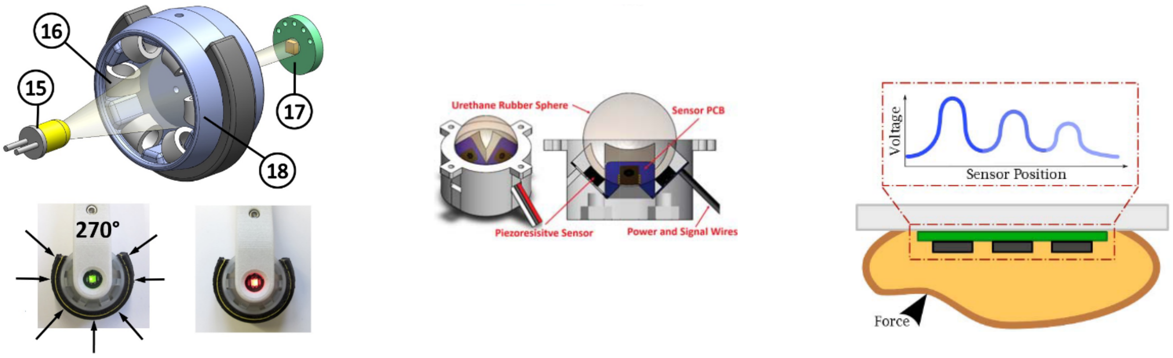

(a) Sensing system based on light sensor [14]

(b) Sensing system based on piezo-resistive elements [9]

(c) Sensing system based on pressure sensors [15]

Figure 1.3: Sensing systems

or current sensors in the actuators by comparing the sensed torque or current with the expected torque or current in case of ground-contact [2].

1.2 Modeling and control methods

For the control aspect of this master's thesis, some insight into the commonly used models and control strategies is useful. Therefore, this chapter will dive deeper into those topics.

1.2.1 Modeling

Although more complex models can be used, the most common models utilized for a hopper leg are the knee extensor model, proposed in [4] and illustrated in Figure 1.4a, and its further elaborated form, namely the spring-loaded inverted pendulum model (SLIP), applied in [17], represented in Figure 1.4b and explained in [18].

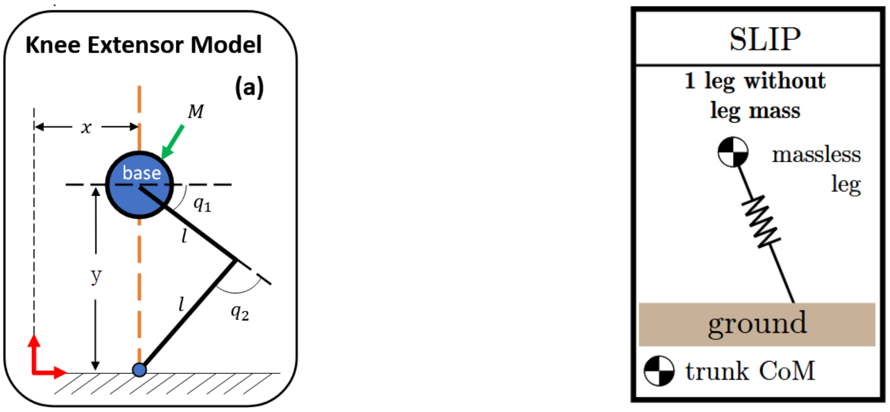

(a) Knee extensor model [4]

(b) SLIP model (spring-loaded inverted pendulum) [18]

Figure 1.4: Modeling methods

The knee extensor model assumes that the entire mass is concentrated at the hip joint, which moves along a frictionless vertical rail. Additionally, the model neglects limb inertia and horizontal displacement of the foot upon ground contact. Consequently, the hopper is dynamically simplified to a point mass. The equations of motion are defined as follows:

$$m\ddot{y} + mg = 0, \quad \text{in flight phase}$$

$$m\ddot{y} + mg = F_y, \quad \text{in stance phase}$$

where $m \in \mathbb{R}$ is the total mass, $\ddot{y} \in \mathbb{R}$ is the vertical acceleration, g is the gravitational acceleration, and $F_y \in \mathbb{R}$ is the vertical ground reaction force. [4]

Similarly, the Spring-Loaded Inverted Pendulum (SLIP) model assumes all mass is concentrated at the hip and neglects limb inertia. In this model, the leg is represented as a massless spring with virtual stiffness $k_{leg} \in \mathbb{R}$. Unlike the knee extensor model, the SLIP model allows movement in both the horizontal and vertical directions, representing the hip position as a vector $\mathbf{r}_{hip} \in \mathbb{R}^2$. This leads to the following equations of motion:

$$m\ddot{\mathbf{r}}_{hip} = \mathbf{F}_g, \quad \text{in flight phase}$$

$$m\ddot{\mathbf{r}}_{hip} = \mathbf{F}_g + \mathbf{F}_{\text{leg}}, \quad \text{in stance phase}$$

Here, $\mathbf{F}_g \in \mathbb{R}^2$ denotes the gravitational force, and $\mathbf{F}_{\text{leg}} \in \mathbb{R}^2$ is the force exerted by the compressed virtual spring. The spring force depends on the leg compression Δy and the stiffness k_{leg}. This model is known for being self-stable and energy-efficient [18]. Additionally, it is well-suited for model based control approaches and forms the foundation of impedance control strategies.

1.2.2 Control methods

There are two main categories of controllers used in the control of legged robots namely learning based methods and model based methods.

In learning based methods, no model is used and a neural network is trained to control the leg optimally. [2] claims that the biggest challenges in model based methods are the detection of the different phases, height estimation and hand tuning all parameters. Using a neural network would overcome these issues. Additionally, [2] states that a reinforcement learning controller could be used for mapping actuator positions and velocities onto a direct torque control. The proposed rewards include energy gain, a height barrier penalty and a joint constraint penalty.

On the other hand, a controller could be based on a model. [14] proposes impedance control for a 2-DOF leg, using only joint angles as generalized coordinates while the leg is in contact with the ground. In impedance control, the stiffness and damping of the foot with respect to the hip is controlled in Cartesian space as follows:

$$\boldsymbol{\tau} = \mathbf{J}^{\mathbf{T}}(\mathbf{K}(\mathbf{r}_d - \mathbf{r}) - \mathbf{D}\dot{\mathbf{r}}),$$

with $\mathbf{r}_d \in \mathbb{R}^2$ the set point of the foot with respect to the hip, $\mathbf{r} \in \mathbb{R}^2$ the actual foot position with respect to the hip, $\mathbf{J} \in \mathbb{R}^{2\times2}$ the foot Jacobian, $\mathbf{K} \in \mathbb{R}^{2\times2}$ and $\mathbf{D} \in \mathbb{R}^{2\times2}$ the desired leg stiffness and damping matrices and $\boldsymbol{\tau} \in \mathbb{R}^2$ the actuator torques. This torque controller is based on encoder position and velocity measurements and motor current measurements.

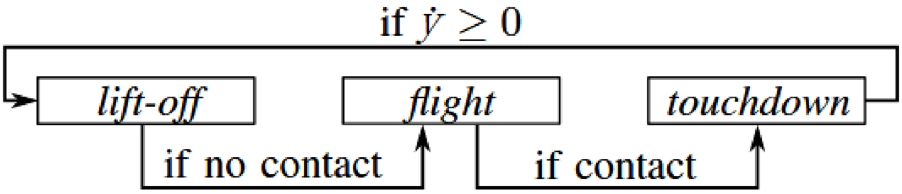

Figure 1.5: Phases in energy shaping [2]

A more advanced model based controller is the energy based control method explained in [2]. The controller shifts between three phases namely lift-off, flight and touchdown, as illustrated in Figure 1.5. For both lift-off and touchdown a stance phase model is used and for the flight phase controller a flight phase model is used. In every phase, a different type of control is applied. In touchdown, the aforementioned impedance controller is used. Once the hip velocity starts increasing, it is assumed to start its lift-off phase and an energy shape controller is used. The energy shape controller is explained in further detail in Section 4.1.2.

When no contact is detected, the controller transitions to a flight-phase PD controller. Upon re-establishing contact, it switches back to the touchdown impedance controller.

1.3 Experiments

As this master's thesis aims to analyze whether the new actuators outperform the state-of-the-art, certain benchmark values are required for comparison. Two common experiments used in the literature to evaluate the performance of hopper robots are vertical jumping and the application of a static vertical force on the hopper to determine the maximum dimensionless stiffness, defined as

$$\bar{k} = \frac{kl}{mg} \in \mathbb{R}$$

where k is the virtual leg stiffness, l is the leg length, m is the mass of the leg, and g is the standard acceleration due to gravity.

In the vertical jumping experiment, the dimensionless maximum jumping height is calculated by

$$\bar{h} = \frac{\text{maximum jump height}}{\text{leg length}} \in \mathbb{R}$$

Reported values for the dimensionless maximum jumping height are 1.14 in [19], 1.57 in [3], and 2.4 in [4]. For the dimensionless stiffness, [14] reports a value of 10.8. These dimensionless values will be used for comparison with the performance of the hopper designed in this work.

1.4 Research question

As discussed in Section 1.1.1, commonly used actuator types each exhibit certain limitations when applied in humanoid robots. For example, series elastic actuators introduce control delays due to their inherent compliance, while hydraulic actuators tend to be heavy and less energy-efficient compared to electromagnetic motor-driven actuators. Quasi-direct drives are effective in quadrupeds but pose challenges when scaling to larger humanoid systems, particularly with respect to maintaining backdrivability and torque density. Furthermore, Section 1.1.1 highlights the potential of the actuators introduced in [8] as a promising alternative for use in humanoid robots. To investigate this proposition, the central research question of this thesis is formulated as follows:

> *How to design an underactuated hopping leg moving in the 2-DOF plane based on in-house developed series clutched actuators, and how can the resulting hopper be controlled? Is the resulting leg more impact-resilient, and can it jump higher than the state-of-the-art?*

The subsequent chapters present the development and evaluation of a hopper incorporating the novel series clutched actuators. Chapter 2 details the design, while Chapters 3 and 4 address system modeling and control strategies, respectively. Chapter 5 then applies these methods in simulation to assess performance, analyze the impact of various control parameters, and benchmark the hopper against existing technologies. Finally, Chapter 6 integrates the findings into an experimental evaluation to determine whether the proposed actuator concept delivers improved performance over conventional approaches.

Chapter 2

Design

This chapter describes the design of the hopper robot developed for this master's thesis. The design was inspired by various approaches found in the literature, while also considering the specific characteristics of the series clutched actuators and the objectives of this research. For instance, to accurately evaluate the performance limits of the actuators, no additional elastic elements were included in the design, as they would dampen the hopping dynamics. The only exception is a slightly elastic 3D-printed layer at the foot, which was added to protect both the foot and the ground during impact.

2.1 Design criteria

Before starting the design process, it is essential to define the main criteria guiding the design choices.

First, the hopper must be as light as possible such that a minimal amount of energy is needed for the hopping. This will primarily be achieved through the material choices and design features of the different components.

Next, the different leg parts—namely, the upper and lower leg—should have the lowest possible inertia. This is achieved by concentrating the mass of the leg parts near the joints. For example, placing the knee actuator on the same axis as the hip actuator minimizes the upper leg inertia.

Additionally, the leg must move stably in the vertical direction with minimal friction. To accomplish this, the hopper is connected to vertical rails via guide carriages.

Lastly, since this work focuses on identifying the performance limits of the actuators, an additional feature was incorporated: a weight rod designed to hold multiple gym weights of up to 5 kg. For instance, a total added mass of 15 kg can be used to simulate the load of a humanoid robot on the hopper.

2.2 General design description

Using the aforementioned criteria, the final design, which is displayed in Figure 2.1, is created. In general, the hopper robot consists of three main parts: the hip base plate, the upper leg, and the lower leg. However, several additional components are also included, such as a transmission system and a sensing system. This section explains the full robot design.

Starting from the rails and moving down to the foot, the first elements encountered are the guide carriages. These carriages connect the leg to the rails and ensure low-friction movement through the use of recirculating ball bearings. Specifically, they are attached to the hip base plate, which carries the hip actuator and the weight rod capable of holding gym weights. The weight rod is connected to the base plate via a small block, referred to as the weight block in the bill of materials.

Next, one plate of the upper leg is mounted to the hip actuator axis. A spacer is used to ensure a safe clearance between the base plate and the upper leg plate, while also aligning the hip joint with the actuator axis. This side of the upper leg is then connected to the opposite side — which holds the knee actuator — using standoffs.

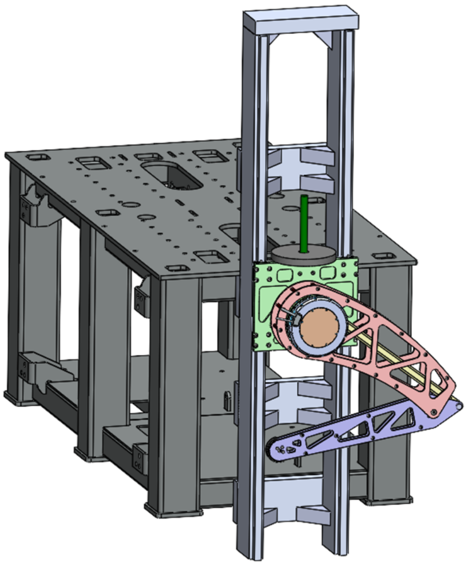

Figure 2.1: Hopper leg setup

On the knee actuator axis, a centering spacer, identical to the one used at the hip, is added to connect the knee actuator to the rotating plates. These two rotating plates are separated by a different type of spacer. Furthermore, the rotating plates are connected to the rotating rod via a shoulder bolt, which also links the two rotating plates. To minimize friction, a bushing and two plain bearings are included at the shoulder bolt connection.

Next, the rotating rod — the main torque and motion transmission element — is connected to the highest point of the lower leg. Its purpose is to push or pull at this point, causing the lower leg to rotate around the knee axis like a lever. For simplicity, the lever arm at the lower leg matches the radius of the rotating plates. The knee axis is fixed at the end of the upper leg. To enable rotation, a hollow axis connected to the lower leg is positioned around the knee axis with bushings in between. This hollow knee axis, called the knee stability part in the bill of materials, is bolted onto both lower leg plates to ensure a secure connection. Additional standoffs reinforce this lower leg assembly.

At the end of the lower leg, between its two plates, is the foot sensing mechanism. It consists of three contact switches and a 3D-printed component that attaches them to one lower leg plate. To protect the contact switches, a 3D-printed elastic cover is included. This cover also transmits displacement to the controller by compressing one or more of the contact switches at the moment of ground contact.

All parts described above can be found in the bill of materials and with corresponding numbers on the parts drawing, which are respectively given in Appendix A and B.

2.3 Designs of different components

Equally important to the overall design is the design of the individual components. This section outlines the design decisions made for each component and the manufacturing methods employed. Strength analyses were performed on the most critical components to ensure structural safety, and the results of these analyses are also discussed. The components identified as critical—those subjected to strength analysis—include the upper and lower leg segments, various elements of the transmission system, and the bolts used within this system.

Conducting the strength analyses required a rough estimation of the expected ground reaction forces. As a result, the initial simulations and design process were carried out in parallel.

2.3.1 Rails

A rough estimation of maximum jumping height led to selecting rails with a height of 1.5 m, as achieving this hopping height would be considered highly successful. This rail height serves as the basis for an initial estimation of the ground reaction forces.

First, the take-off velocity required to reach a given height can be estimated using the conservation of energy:

$$\frac{1}{2}mv^2 = mgh \quad \Rightarrow \quad v = \sqrt{2gh}$$

with m the hopper mass, v the take-off velocity, h the given height to reach and g the gravitational acceleration.

Assuming the lift-off starts from rest ($v_0 = 0$), the following kinematic relations apply:

$$v = at, \quad d = \frac{1}{2}at^2 \quad \Rightarrow \quad t = \frac{v}{a}, \quad d = \frac{v^2}{2a} \quad \Rightarrow \quad a = \frac{v^2}{2d} = \frac{gh}{d}$$

where d is the distance covered during lift-off and a is the required vertical acceleration while in contact with the ground to reach the desired height h. The corresponding ground reaction force (GRF) is then given by:

$$F_{\text{GRF}} = F_{\text{inertial}} + F_{\text{gravity}} = m_{\text{tot}}(g + a)$$

Assuming the hip travels a vertical distance of approximately $d = 0.5\,\text{m}$ (from $0.3\,\text{m}$ to $0.8\,\text{m}$) during lift-off and the total mass $m = 13.62\,\text{kg}$ is concentrated at the hip, as in the knee extensor model, we compute:

$$a = \frac{9.81\,\text{m/s}^2 \cdot 1.5\,\text{m}}{0.5\,\text{m}} = 29.43\,\text{m/s}^2$$

$$F_{\text{GRF}} = 13.62\,\text{kg} \cdot (9.81\,\text{m/s}^2 + 29.43\,\text{m/s}^2) = 534.45\,\text{N}$$

Hence, the estimated ground reaction force required for the jump is approximately 534.45 N. However, as detailed in Chapter 5, simulation results show higher peak ground reaction forces, as illustrated in Figure 2.2. These peaks are likely influenced by numerical artifacts. From the simulation plot, a conservative estimate for the maximum GRF is 750 N, denoted by the orange reference line in the graph.

To ensure structural integrity under these loads, the finite element strength analyses in SolidWorks apply a minimum load of 750 N to all components. Depending on the criticality of each component, some may be tested under even higher forces.

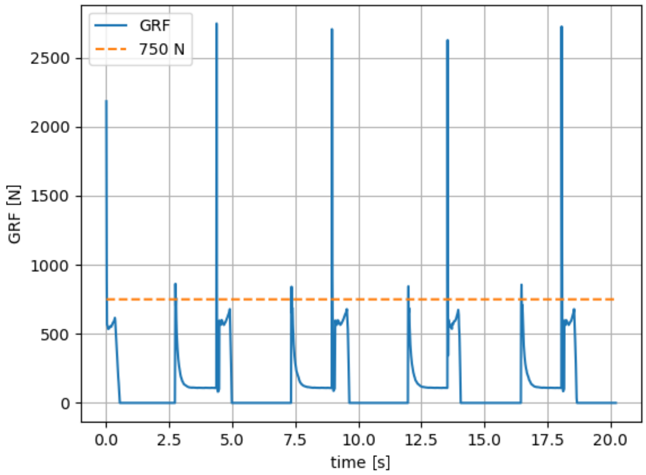

Figure 2.2: Ground reaction forces when hopping to 1.5 m

2.3.2 Hip base plate

The hip base plate is the component that connects the leg to the rails via four guide carriages and is depicted in Figure 2.3 as the green plate. It holds the hip actuator and the weight rod. To ensure structural stability while minimizing weight, the plate is made of aluminum and designed with a thickness of 14 mm. Unnecessary material was machined away to reduce weight without compromising integrity. In addition to weight reduction, the plate required specific machining for efficient assembly.

First, the hole for the actuator must be perpendicular to the plate surface, with a maximum roughness of 1.6 µm. The bolting holes connecting the actuator to the plate must not deviate by more than 0.2° in alignment, and the radius at which the holes are drilled must not deviate by more than 0.2 mm.

Furthermore, the mounting areas for the guide carriages must lie on the same plane on both sides of the plate, also with a surface roughness of 1.6 µm or better. The reference edge used for carriage alignment must be completely straight and perpendicular to the mounting surface. Finally, the surface where the weight rod connects via the weight block must be flat and parallel to the guide carriage mounting surfaces, though it does not require a polished finish.

Additional manufacturing constraints and tolerances are detailed in the technical drawing provided in Appendix C.

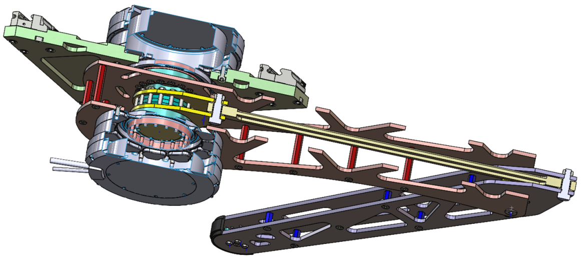

Figure 2.3: Cross-section upper leg

A technical drawing was also required for the weight block, which carries the weight rod. This drawing is provided in Appendix D.

2.3.3 Hip joint

The hip joint, which can be seen in Figure 2.3, located on the hip actuator axis, consists of multiple components, namely two types of spacers, two rotating plates, and the knee actuator.

The first type of spacers, displayed in the lighter blue on Figure 2.3, centralize the upper leg with respect to the hip actuator and centralize the rotating plates with respect to the knee actuator. Moreover, they maintain a safe distance between the aforementioned components. These spacers, made of aluminum, are manufactured by turning and require only parallelism and smoothness of the surfaces connecting to the other parts. A technical drawing of the hip spacers is provided in Appendix E.

The second type of spacers, displayed in the darker blue in Figure 2.3, are designed to maintain a fixed distance between the rotating plates. This distance equals the width of the rotating rod plus the combined width of the two plain bushings. Three of these spacers are used to cover this width. These components are laser cut from the same 5 mm aluminum plate as the upper and lower leg plates to minimize manufacturing costs. The design features cut-outs for the bolts used to connect the rotating plates to the knee actuator, which also holds the spacers in place.

Lastly, the two rotating plates are centered within the hip joint. They are part of the transmission system, which will be explained in Section 2.3.4. The two rotating plates are identical and are laser cut from the same 5 mm aluminum plate as the upper and lower leg plates to minimize manufacturing costs.

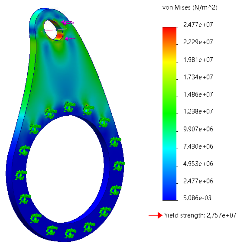

Figure 2.4: Strength analysis rotating plates

A key design feature of the rotating plates is the radius at which the hole is positioned for connection to the rotating rod. This radius was selected to be short enough to fit within the upper leg while being as large as possible to maximize the lower leg's angular motion range. This trade-off resulted in a radius of 78 mm and an angular motion range of 116°for the lower leg.

Due to the high torque transmission through these components, they are considered critical, thus requiring a strength analysis. The finite element analysis in SolidWorks, using an aluminum yield strength of 27.6 MPa and an applied force of 750 N, produced the results shown in Figure 2.4. The analysis proves that each rotating plate can withstand a force of up to 750 N. Assuming an equal load distribution, the two plates can collectively withstand an impact force of 1500 N.

2.3.4 Transmission system

In addition to the rotating plates, the transmission system consists of a rotating rod, two shoulder bolts, and the necessary bushings and plain bearings to minimize friction. One shoulder bolt connects the rotating plates to the rotating rod, while the other connects the rod to the lower leg. This configuration enables the lower leg to rotate around the knee axis, as described in Section 2.3.6.

The rotating rod is considered the most critical component of the transmission system and was therefore subjected to a finite element analysis in SolidWorks. A load of 2500 N was applied, and the yield strength was set to 27.6 MPa, corresponding to the aluminum material used for the rod.

Since the rod is subjected to both compressive and tensile forces—during leg extension and bending, respectively—two separate strength analyses were performed. The results are shown in Figure 2.5.

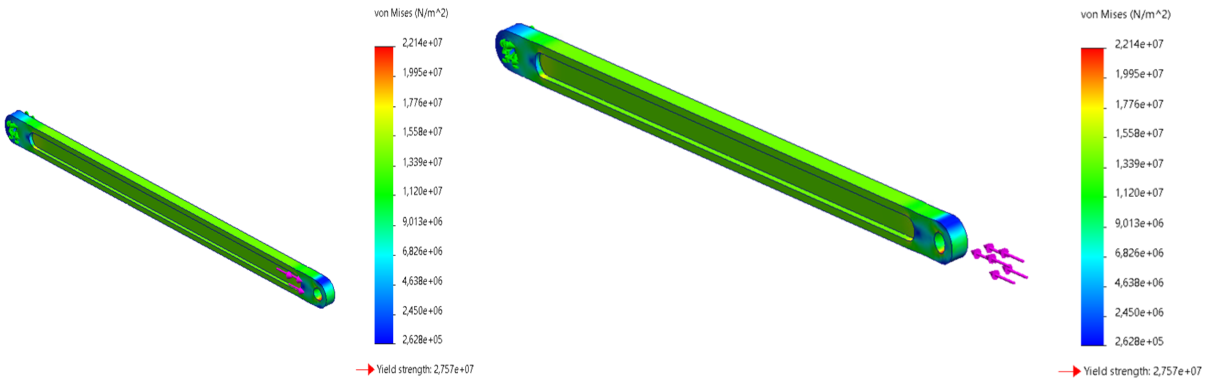

(a) Tension force

(b) Compression force

Figure 2.5: Strength analyses rotating rod

The rod is manufactured by removing material from its center, creating an I-beam profile along the middle section. This I-profile reduces mass while increasing bending stiffness. Additionally, the ends of the rod are rounded to eliminate sharp corners and avoid potential safety hazards. A detailed technical drawing of this component is included in Appendix F.

Other critical components of the transmission system are the shoulder bolts. The two bolts should be able to withstand the ground reaction forces at the moment of impact. The chosen diameter was based on the calculation shown below, using an impact force of 2500 N, a yield strength of 250 MPa and a safety factor SF = 3.

$$\sigma_{\text{design}} = \frac{\sigma_{\text{allow}}}{SF} = \frac{250 \cdot 10^6\ \text{N/m}^2}{3} = 83.33 \cdot 10^6\ \text{N/m}^2$$

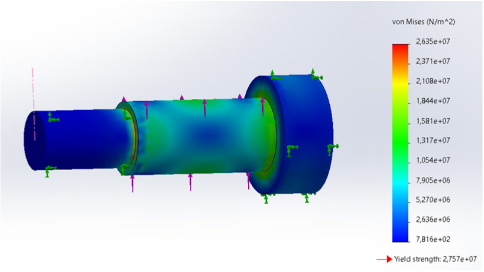

Figure 2.6: Strength analysis shoulder bolt

The bolts carry the rotating rod and connect it on both sides to two surfaces, meaning the bolts are loaded under double shear. The formula for double shear stress is:

$$\tau = \frac{F}{2A} \quad \text{with} \quad A = \frac{\pi d^2}{4}$$

The bolt will fail when the Von Mises shear stress is exceeded, which equals $\sqrt{3}\tau$.

$$\sqrt{3}\tau = \sigma_{design} \implies d = \sqrt{\frac{4 \cdot F_{\text{impact}} \cdot \sqrt{3}}{2 \cdot \pi \cdot \sigma_{\text{design}}}}$$

$$\implies d = \sqrt{\frac{4 \cdot 2500 \text{ N} \cdot \sqrt{3}}{2 \cdot \pi \cdot 83.33 \cdot 10^6 \text{ N/m}^2}} \implies d \approx 0.00575m = 5.75mm$$

As a result, an M8 shoulder bolt with a nominal shoulder diameter of 10 mm was selected. In addition, the bolts were subjected to a finite element analysis in SolidWorks. The analysis considered an impact force of 1000 N and a yield strength of 27.6 MPa, assuming that if an aluminum bolt could withstand the impact, a steel bolt would definitely be sufficiently strong. The results, shown in Figure 2.6, confirm that the selected bolts meet the required strength criteria.

2.3.5 Upper leg

The transmission system described in the previous section is enclosed in the upper leg. The upper leg structure consists of two upper leg plates and multiple standoffs connecting them to each other. In addition, it has cutouts for connection to the two actuators and the knee joint. The two plates are similarly designed with some differences in the connection places for the actuators. The plates are laser cut, have a thickness of 5 mm and are made of aluminum. To lower the mass, triangular shaped elements are removed. The triangular structure was chosen due to its force distributing properties.

As the knee joint is directly connected to this upper leg, it is assumed that the upper leg will also be subjected to large forces. Therefore, a SolidWorks finite element strength analysis is performed in which the upper leg is subjected to a 750 N impact and the yield strength is set equal to 27.6 MPa.

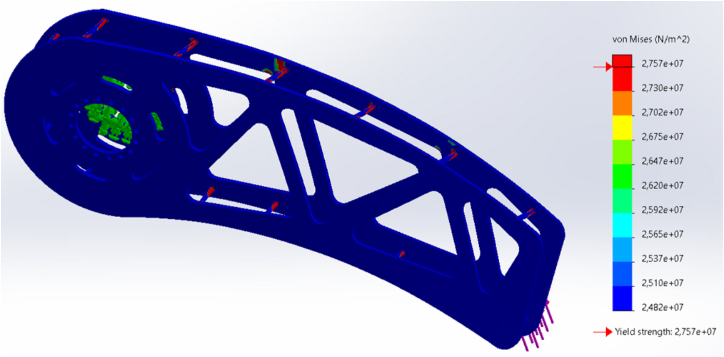

Figure 2.7: Strength analysis upper leg

The results demonstrate that the yield strength is exceeded at several locations, which can be observed by the red areas in Figure 2.7. However, upon evaluating these stresses, it becomes clear that they occur either in the standoffs themselves or at the points where the standoffs meet the plates. The stresses at the standoff-plate junctions are a result of modeling the upper leg as a single component, which causes stress concentrations at the sharp corners where the standoffs meet the plates. In the actual system, this connection will not be fixed, so these stress concentrations will not be present. Furthermore, the exceeding stresses in the standoffs themselves are not expected to cause problems in the real setup. While the standoffs are modeled in aluminum here, in reality, they are made of steel, which has a higher yield strength than the aluminum used in the model.

2.3.6 Knee joint

The knee joint consists of a knee axis, which is connected to the upper leg, and a knee stability part, which is connected to the lower leg. Between the knee stability part and the knee axis, two flanged bearings minimize the friction in the knee joint.

Both the knee stability component and the knee axis were manufactured from aluminum. Technical drawings were created for their production and are included in Appendix G and H respectively. For the knee axis, the tolerance on the inner diameter of the flanged bushing was critical. On the contrary, for the knee stability component, the tolerance on the outer diameter of the flanged bushing was essential. Additionally, for the knee stability part, the axis had to be perpendicular to the surfaces used to connect it to the lower leg plates.

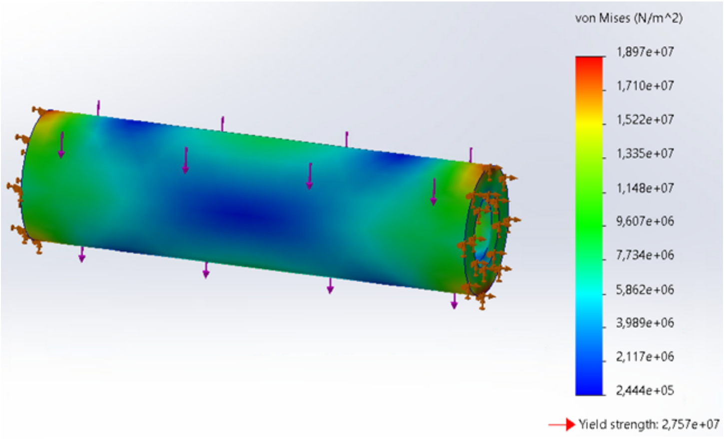

Figure 2.8: Knee axis strength analysis

As the knee axis will be subjected to the ground impact forces, a finite element analysis in SolidWorks was executed. In the analysis, it was subjected to a force of 1000 N and the yield strength was set to 27.6 MPa. The results, displayed in Figure 2.8, prove that the axis is strong enough.

The bolts connecting the knee axis to the upper leg were dimensioned based on an assumed impact force of 2500 N, distributed over two bolts. The selected bolt material has a yield strength of 250 MPa, and a safety factor of $SF = 3$ is applied.

$$\sigma_{\text{design}} = \frac{\sigma_{\text{allow}}}{SF} = \frac{250 \cdot 10^6 \ \text{N/m}^2}{3} = 83.33 \cdot 10^6 \, \text{N/m}^2$$

The bolts are primarily subjected to shear stress τ, with the corresponding Von Mises stress approximated as $\sigma_{\text{VM}} = 3\tau$ for conservative design. The shear stress is given by:

$$\tau = \frac{F}{A}, \quad \text{where} \quad A = \frac{\pi d^2}{4}$$

Solving for the required bolt diameter d under the Von Mises criterion yields:

$$\sigma_{\text{vM}} = \sigma_{\text{design}} \quad \Rightarrow \quad \sqrt{3}\tau = \sigma_{\text{design}} \quad \Rightarrow \quad \tau = \frac{\sigma_{\text{design}}}{\sqrt{3}}$$

$$\frac{F}{\frac{\pi d^2}{4}} = \frac{\sigma_{\text{design}}}{\sqrt{3}} \quad \Rightarrow \quad d = \sqrt{\frac{4F\sqrt{3}}{\pi \sigma_{\text{design}}}}$$

Using $F = 1250$ N per bolt, the required diameter is:

$$d = \sqrt{\frac{4 \cdot 1250 \ \text{N} \cdot \sqrt{3}}{\pi \cdot 83.33 \cdot 10^6 \ \text{N/m}^2}} \approx 0.00575 \, \text{m} = 5.75 \, \text{mm}$$

To be safe, two standard M8 bolts are selected.

2.3.7 Lower leg

The lower leg consists of two identical lower leg plates, multiple standoffs to maintain a fixed distance between the plates, and a sensing system, described in Section 2.3.8. The plates are manufactured by laser cutting a 5 mm thick aluminum sheet and, like the upper leg plates, they feature a triangular structure.

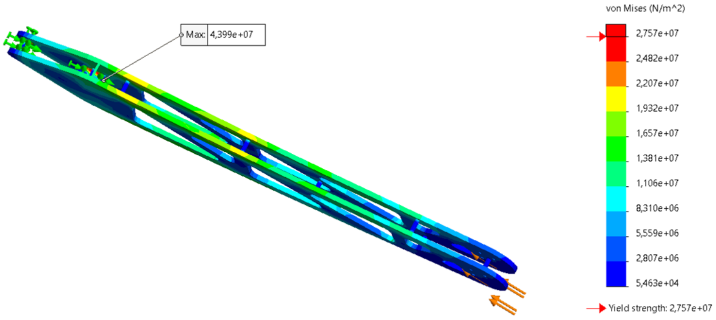

Figure 2.9: Lower leg strength analysis

At the top of the lower leg, a hole is included to connect the rotating rod from the transmission system, as described in Section 2.3.4. The lever up to this hole is designed to match the radius of the rotating plates. This choice was made for simplicity, as it eliminates the need for reduction calculations for the motion and torque transmitted by the knee actuator.

The lower leg is also considered a critical component in the hopping process, and therefore a strength analysis has been performed. For the analysis, the lower leg is subjected to a load of 750 N, and the yield strength is set to 27.6 MPa.

Similar to the strength analysis of the upper leg, the yield strength is exceeded in certain areas, as demonstrated on Figure 2.9. This appears to be the result of modeling the lower leg as a single component, as the problematic stresses occur at the intersection of two parts, creating stress concentrations. These stress concentrations will not be present in the real system, as the lower leg is not a single component. Therefore, it can be concluded that the lower leg is strong enough.

2.3.8 Sensing system

The sensing system, shown on Figure 2.10, is located at the lowest point of the lower leg. It consists of three contact switches, connected to a 3D-printed component and protected by an elastic 3D-printed component.

The choice of using simple contact switches was based on the fact that a more complex sensing mechanism was not necessary for this master's thesis. While mapping the forces at the foot at the moment of impact could be useful for understanding the forces involved, it is not required for basic control and, therefore, was not incorporated into this design. The controller only needs a sensing mechanism to detect whether contact is made, and contact switches are sufficient for this purpose.

The contact switches should be glued onto the 3D-printed blue part, which is attached to one side of the lower leg. The black 3D-printed part is made from a more elastic material and is designed to compress one or more of the contact switches upon impact. To ensure adequate coverage for ground detection, the three sensors are positioned at a 45° angle relative to each other, with the leftmost sensor aligned with the y-direction and the rightmost sensor aligned with the x-direction.

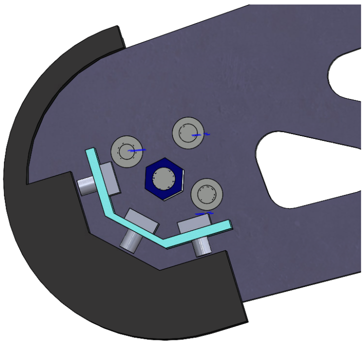

Figure 2.10: Sensing system

2.4 Conclusion on design

2.4.1 Leg properties

The resulting design is shown in Figure 2.1, and its properties are listed in Table 2.1. The most notable properties are the leg length, which is 0.9 m, and the leg mass, which is 13.62 kg. This total mass includes all the described components, such as the base plate and guide carriages, but excludes the rails. In other words, the total mass of 13.62 kg represents the mass that the actuators will need to move during the experiments. Additionally, the inertia of both leg segments is relatively low, with the values being quite similar for the upper and lower limbs. This is because, in the upper leg—which has a greater mass—the center of mass is positioned closer to the joint, while in the lower leg—which has a smaller mass—the center of mass is located farther from the joint.

Table 2.1: Physical properties of the leg

Property	**Value**	**Unit**
Length	0.9	m
Total mass	13.62	kg
Mass upper leg	5.382	kg
Inertia upper leg	0.1	$\mathrm{kgm^2}$
CoM – joint upper leg	-40.36	mm
Mass lower leg	0.96	kg
Inertia lower leg	0.06	$\mathrm{kgm^2}$
CoM – joint lower leg	178.63	mm

2.4.2 Assembly of the design

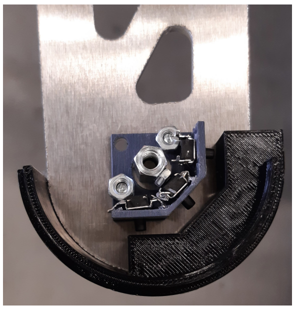

Figure 2.11: Sensing system real setup

After the design was completed, all components were ordered, and the leg was assembled. During the assembly process, it became clear that some design choices could have been improved and should be avoided in future work.

Initially, gluing the contact switches onto the 3D-printed part proved problematic. Specifically, the adhesive caused the switches to become stuck in the open or closed position. As a result, a mechanical fixation method was implemented, as shown in Figure 2.11. However, this solution is likely not robust enough to withstand dynamic hopping motions. In addition, the elastic 3D-printed layer covering the foot was too thin. As a consequence, the contact switches fail to activate when the foot is compressed. Therefore, a redesign of this component is necessary to ensure reliable activation of the foot contact sensors.

Another issue with the design of the sensing system is that if a problem arises, the entire leg must be disassembled. This makes it labor-intensive to address damage to one of the sensors. In future design iterations, this should be avoided, as sensors are fragile and problems are most likely to occur during the dynamic motions of hopping.

Secondly, the knee axis is currently connected to the upper leg by a single bolt on each side. However, since the axis can freely rotate within the knee joint, this single-bolt attachment makes it difficult to tightly secure the knee axis. As a result, the knee joint is not as stable as it could be, which may lead to vibrations in the leg during hopping.

Despite these issues, the resulting design was easy to assemble. The final assembly is shown in Figure 2.12.

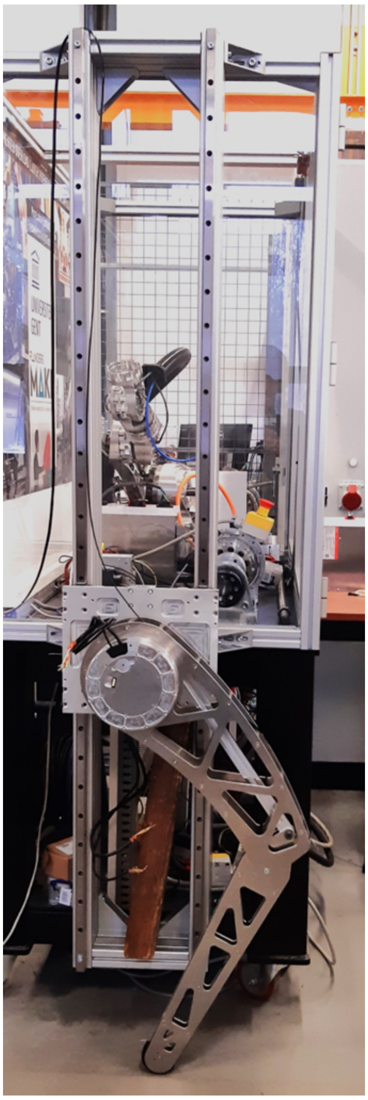

Figure 2.12: Setup result

Chapter 3

Model of the hopper robot

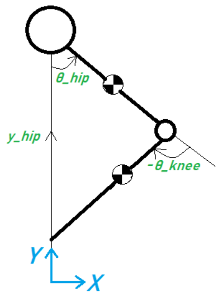

Figure 3.1: Kinematic model of hopper robot

Kinematically, the hopper is modeled as a 3 degree of freedom (DOF) system as demonstrated in Figure 3.1. It has three generalized coordinates, namely the hip height, the hip angle and the knee angle. Only two of those coordinates are actuated, making the hopper robot an underactuated robot. The model consists of three main links, namely the hip base, the upper leg and the lower leg. It is assumed that links only have a momentum around the z-axis for simplicity. Furthermore, the hip only moves along the y-axis, because it is connected to a linear rail via guide carriages as described in Chapter 2.

The kinematic design is used to calculate the equations of motion. By ignoring friction in the flight phase, the hopper can be modeled as a free body with no external forces. On the contrary, during stance phase, there will be an external force, namely the ground reaction force. As a result, the system needs two sets of equations of motions:

$$\mathbf{M}\ddot{\mathbf{q}} + \mathbf{C}\dot{\mathbf{q}} + \mathbf{K}\mathbf{q} = \mathbf{0}, \quad \text{in flight phase}$$

$$\mathbf{M}\ddot{\mathbf{q}} + \mathbf{C}\dot{\mathbf{q}} + \mathbf{K}\mathbf{q} = \mathbf{J}_{foot}^{T}\mathbf{F}_{GRF}, \quad \text{in stance phase}$$

with $\mathbf{M} \in \mathbb{R}^{3\times3}$ the mass matrix, $\mathbf{C} \in \mathbb{R}^{3\times3}$ the damping matrix, $\mathbf{K} \in \mathbb{R}^{3x3}$ the stiffness matrix, $\mathbf{q} \in \mathbb{R}^3$ the coordinate vector, $\mathbf{J}_{foot} \in \mathbb{R}^{2\times3}$ the foot Jacobian and $\mathbf{F}_{GRF} \in \mathbb{R}^2$ the ground reaction force. The transpose of the foot Jacobian is equal to

$$\mathbf{J}_{foot}^{T} = \begin{bmatrix} l_{upp}\cos(\theta_{hip}) + l_{low}\cos(\theta_{hip}+\theta_{knee}) & l_{upp}\sin(\theta_{hip}) + l_{low}\sin(\theta_{hip}+\theta_{knee}) \\ 0 & 1 \\ l_{low}\cos(\theta_{hip}+\theta_{knee}) & l_{low}\sin(\theta_{hip}+\theta_{knee}) \end{bmatrix} \tag{3.1}$$

with l_{upp} the length of the upper leg, l_{low} the length of the lower leg and $\theta_{hip} \in \mathbb{R}$ and $\theta_{knee} \in \mathbb{R}$ the joint coordinates.

When friction is considered, an external friction force is introduced at the hip base during both the stance and flight phases. This force arises from the linear rail along the vertical (y) axis and is computed as:

$$F_{y,\text{fr}} = -b_{\text{rail}} \cdot \left(-l_{\text{upp}}\dot{\theta}_{\text{hip}}\sin(\theta_{\text{hip}}) - l_{\text{low}}(\dot{\theta}_{\text{hip}} + \dot{\theta}_{\text{knee}})\sin(\theta_{\text{hip}} + \theta_{\text{knee}})\right)$$

This expression is derived from the vertical position of the hip:

$$y_{\text{hip}} = l_{\text{upp}}\cos(\theta_{\text{hip}}) + l_{\text{low}}\cos(\theta_{\text{hip}} + \theta_{\text{knee}}) \tag{3.2}$$

$$\Rightarrow v_{y,\text{hip}} = \frac{dy_{\text{hip}}}{dt} = -l_{\text{upp}}\dot{\theta}_{\text{hip}}\sin(\theta_{\text{hip}}) - l_{\text{low}}(\dot{\theta}_{\text{hip}} + \dot{\theta}_{\text{knee}})\sin(\theta_{\text{hip}} + \theta_{\text{knee}}) \tag{3.3}$$

$$\Rightarrow F_{y,fr} = -b_{\text{rail}} \cdot v_{y,\text{hip}}$$

with b_{rail} in $\frac{N \cdot s}{m}$. The resulting friction force vector becomes:

$$\mathbf{F}_{\text{fr}} = \begin{bmatrix} 0 \\ F_{y,\text{fr}} \end{bmatrix} \in \mathbb{R}^2$$

This modifies the equations of motion, which now incorporate the friction force via the Jacobian at the hip:

$$\mathbf{M}\ddot{\mathbf{q}} + \mathbf{C}\dot{\mathbf{q}} + \mathbf{K}\mathbf{q} = \begin{cases} \mathbf{J}_{\text{hip}}^T \mathbf{F}_{\text{fr}}, & \text{flight phase} \\ \mathbf{J}_{\text{foot}}^T \mathbf{F}_{\text{GRF}} + \mathbf{J}_{\text{hip}}^T \mathbf{F}_{\text{fr}}, & \text{stance phase} \end{cases} \tag{3.4}$$

where $\mathbf{J}_{\text{hip}}$ is the Jacobian mapping forces at the hip base to generalized coordinates:

$$\mathbf{J}_{\text{hip}} = \begin{bmatrix} 0 & 0 & 0 \\ 0 & 1 & 0 \end{bmatrix} \in \mathbb{R}^{2\times 3}$$

This ensures that the friction force is correctly applied in the vertical direction through the hip constraint.

3.1 Model parameters

The model defined in Equation 3.4 is employed in Chapter 5 and Chapter 6 for both simulations and experimental validation. The associated model parameters are summarized in Table 3.1.

The first column of the table lists the parameters for the hopper located in Ghent, which is utilized in all simulations and in the experiments described in Section 6.1. The second column provides the parameters for the hopper at the Deutsches Forschungszentrum für Künstliche Intelligenz (DFKI) in Bremen, which is employed in a separate set of experiments discussed in Section 4.2 and 6.2.

Table 3.1: Model parameters

Parameter	**Ghent**	**DFKI**	**Unit**
Length upper leg	0.45	0.15	m
Length lower leg	0.45	0.14	m
Mass hip base	6.66	0.913	kg
Mass upper leg	5.57	1.28	kg
Mass lower leg	0.97	0.13	kg
Inertia upper leg	0.11	0.0016	kgm^2
Inertia lower leg	0.06	$6.3 \cdot 10^{-5}$	kgm^2

Chapter 4

Control algorithms

This chapter describes the different control algorithms used to control the hopper robot designed in Chapter 2. First, the general control approach is explained. Next, a possible expansion of the control algorithm is proposed, namely the control of the hopper on an elastic ground support. Later, in Chapter 5, the effect of changing different control parameters will be studied by evaluating them in simulations.

All the proposed control algorithms in this thesis are torque controllers, which is a type of control algorithm designed to directly regulate the torque output of an actuator, rather than controlling position or velocity.

4.1 General control method

Inspired by the multiphase control algorithm proposed in [2], a control architecture consisting of three phases is used, as illustrated in Figure 4.1.

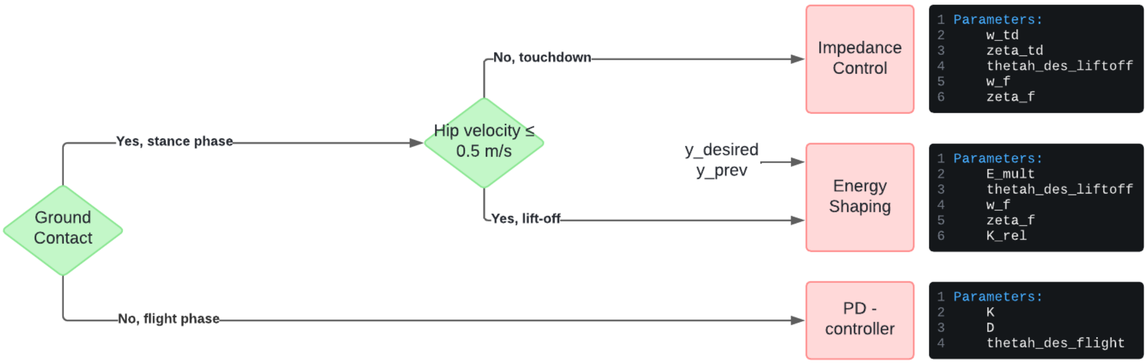

```
Parameters:
    w_td
    zeta_td
    thetah_des_liftoff
    w_f
    zeta_f
```

```
Parameters:
    E_mult
    thetah_des_liftoff
    w_f
    zeta_f
    K_rel
```

```
Parameters:
    K
    D
    thetah_des_flight
```

Figure 4.1: General control architecture

The three distinct phases are flight phase, touchdown phase and lift-off phase. Depending on the phase, a different control method is used. Additionally, the control architecture incorporates a state machine to determine the transition between the different phases.

The flight phase uses a simple PD control towards the desired flight angle, using

$$\boldsymbol{\tau} = \begin{bmatrix} \tau_{hip} \\ \tau_{knee} \end{bmatrix} = K_p \begin{bmatrix} \theta_{hip,des} - \theta_{hip} \\ \theta_{knee,des} - \theta_{knee} \end{bmatrix} + K_d \begin{bmatrix} 0 - \dot{\theta}_{hip} \\ 0 - \dot{\theta}_{knee} \end{bmatrix}$$

with $K_p \in \mathbb{R}$, $K_d \in \mathbb{R}$ and $\boldsymbol{\tau} \in \mathbb{R}^2$.

The touchdown phase, also called the buffering phase, which is the phase between the moment of touchdown and the start of lift-off, uses an impedance control as explained in 4.1.1. Lastly, the lift-off phase, between the leg being at its lowest point (exertion point) and the moment of take-off, uses an energy shaping controller, as explained in 4.1.2. By alternating between these three control methods, an advanced controller is formed allowing accurate control of the hopper robot.

The next sections describe the different controllers and the methods used for determining phase changes.

4.1.1 Impedance control

The concept of the impedance control method is depicted in Figure 4.2. The controller assumes that all the mass of the hopper is concentrated at its base and that a virtual spring-damper system the base to the hopper foot connects, similar to the spring system in the SLIP-model explained in [18]. In addition, a virtual spring-damper system can be added between the foot and a virtual wall to have impedance control over the foot position with respect to the y-axis. Both spring-damper systems can be tuned such that the hip and foot go to desired positions, namely a desired hip height and a desired foot offset. The control parameters for the combined impedance controller are: ω_{leg}, ζ_{leg}, desired angle for lift-off ($\theta_{lift-off,des}$), ω_{foot}, ζ_{foot} and desired foot offset (e).

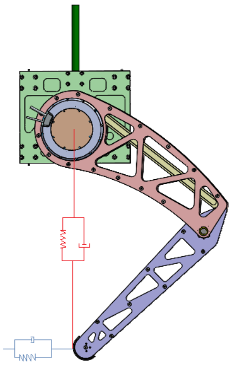

Figure 4.2: Impedance control model

The first two parameters, namely ω_{leg} and ζ_{leg}, are converted into a virtual spring and damper. The spring stiffness is calculated as $K_{leg} = \omega_{leg}^2 m_{tot}$, and the damping coefficient as $D_{leg} = 2m_{tot}\omega_{leg}\zeta_{leg}$, with m_{tot} the total mass of the hopper. These values are used as the proportional and derivative gains, respectively, in a PD controller.

The desired hip angle at lift-off, denoted $\theta_{lift\text{-}off,des,hip}$, is specified, and the desired knee angle is defined as $\theta_{lift\text{-}off,des,knee} = -2\theta_{lift\text{-}off,des} = -2\theta_{lift\text{-}off,des,hip}$.

The leg impedance controller is implemented in joint space, leading to the following expressions for the required joint torques used in torque control:

$$\boldsymbol{\tau}_{leg} = K_{leg} \begin{bmatrix} \theta_{lift\text{-}off,des,hip} - \theta_{hip} \\ \theta_{lift\text{-}off,des,knee} - \theta_{knee} \end{bmatrix} + D_{leg} \begin{bmatrix} 0 - \dot{\theta}_{hip} \\ 0 - \dot{\theta}_{knee} \end{bmatrix}$$

with $K_{leg} \in \mathbb{R}$, $D_{leg} \in \mathbb{R}$ and $\boldsymbol{\tau}_{leg} \in \mathbb{R}^2$.

Similarly, ω_{foot} and ζ_{foot} can be converted into a corresponding spring-damper system, with stiffness $K_{foot} = \omega_{foot}^2 m_{tot}$ and damping coefficient $D_{foot} = 2m_{tot}\omega_{foot}\zeta_{foot}$. However, this controller is implemented in the Cartesian space. Therefore, the transpose of the foot Jacobian, given in equation 3.1 is also required.

The torques needed for the foot-impedance controller are:

$$\begin{aligned} \boldsymbol{\tau}_{\text{foot}} = \mathbf{S}\Bigg(\mathbf{J}_{\text{foot}}^T \Bigg(& K_{\text{foot}} \begin{bmatrix} -l_{\text{upp}}\sin(\theta_{\text{hip}}) - l_{\text{low}}\sin(\theta_{\text{hip}} + \theta_{\text{knee}}) - e \\ 0 \end{bmatrix} \\ & + D_{\text{foot}} \begin{bmatrix} -l_{\text{upp}}\dot{\theta}_{\text{hip}}\cos(\theta_{\text{hip}}) - l_{\text{low}}(\dot{\theta}_{\text{hip}} + \dot{\theta}_{\text{knee}})\cos(\theta_{\text{hip}} + \theta_{\text{knee}}) \\ 0 \end{bmatrix} \Bigg)\Bigg) \end{aligned}$$

with $K_{foot} \in \mathbb{R}$, $D_{foot} \in \mathbb{R}$ and

$$\mathbf{S} = \begin{bmatrix} 1 & 0 & 0 \\ 0 & 0 & 1 \end{bmatrix} \in \mathbb{R}^{2\times 3} \tag{4.1}$$

Combining the foot and leg impedance control results in the torque calculation for the impedance torque controller:

$$\boldsymbol{\tau}_{impedance} = \boldsymbol{\tau}_{leg} + \boldsymbol{\tau}_{foot} \in \mathbb{R}^2$$

The proposed impedance controller is used in the touchdown phase of the jumping control algorithm. However, it can also be used for trajectory following on the ground as demonstrated in Section 5.3.

Using ω (natural frequency) and ζ (damping ratio) for tuning the impedance controller, rather than directly adjusting the proportional (P) and derivative (D) gains, provides a more intuitive and systematic approach. The parameter ω directly influences the system's response speed, while ζ governs the damping behavior, allowing for more intuitive tuning.

4.1.2 Energy shaping control algorithm

Energy shaping is the control strategy employed during the lift-off phase of the general controller. Based on the desired height, the current energy, and the previous jump height, the controller calculates the energy and corresponding torques that must be provided by the actuators to reach the target height in the next jump.

Since direct measurement of height is not possible due to the absence of a linear sensor, a height estimation method is used. To compensate for potential inaccuracies in this estimation, a control parameter $E_{mult} \in \mathbb{R}$ is introduced in the calculation of the current energy in Step 1 of the controller calculations listed below. Additionally, a dynamic control parameter $K_{rel} \in \mathbb{R}$ is used to slightly adjust the target energy based on height estimations of previous jumps. The controller follows these steps:

Step 1: Energy calculations

$$E_{\text{current}} = E_{mult} \left(m_{tot} \cdot y_{hip} \cdot g + \frac{1}{2} \cdot m_{tot} \cdot \dot{y}_{hip}^2 \right)$$

$$E_{\text{previous}} = m_{tot} \cdot y_{\text{last peak}} \cdot g$$

$$E_{\text{desired}} = m_{tot} \cdot y_{\text{desired}} \cdot g$$

with m_{tot} the total mass of the hopper, g the gravitational acceleration, y_{hip} the current position of the hip, $y_{\text{last peak}}$ the maximum hip height during the previous jump and y_{desired} the desired jumping height.

Step 2: Calculation of K_{rel}

$$K_{rel} = \frac{E_{desired}}{E_{previous}}$$

Step 3: Calculation of the needed leg force

$$F_{step} = K_{rel} \frac{E_{desired} - E_{current}}{y_{lift-off,desired} - y_{hip}}$$

Step 4: Calculation of the corresponding torques

$$\boldsymbol{\tau}_{ES} = \mathbf{S}\mathbf{J}_{foot}^T \begin{bmatrix} 0 \\ F_{step} \end{bmatrix} \in \mathbb{R}^2$$

with $\mathbf{S}$ given in Eq. 4.1 and $\mathbf{J}_{foot}^T$ given in Eq. 3.1.

Step 5: Cartesian space control of foot to desired position, same as in impedance control (see Section 4.1.1)

$$\boldsymbol{\tau}_{foot} = \mathbf{SJ}_{foot}^T \left(K_{foot} \begin{bmatrix} 0 - l_{upp}\sin(\theta_{hip}) - l_{low}\sin(\theta_{hip} + \theta_{knee}) - e \\ 0 \\ 0 \end{bmatrix} \right.$$
$$\left. + D_{foot} \begin{bmatrix} 0 - l_{upp}\dot{\theta}_{hip}\cos(\theta_{hip}) - l_{low}(\dot{\theta}_{hip} + \dot{\theta}_{knee})\cos(\theta_{hip} + \theta_{knee}) \\ 0 \\ 0 \end{bmatrix} \right) \in \mathbb{R}^2$$

Step 6: Calculation of needed torque for torque control

$$\boldsymbol{\tau}_{control} = \boldsymbol{\tau}_{foot} + \boldsymbol{\tau}_{ES} \in \mathbb{R}^2$$

The above proposed control strategy requires height estimations during both the stance and flight phases. During the stance phase, forward kinematics are used to compute the hip height and velocity, as in Equation 3.2 and 3.3. In the flight phase, the height is estimated using the free-body motion equation:

$$y_{hip} = y_0 + v_0(t - t_{lo}) - \frac{g}{2}(t - t_{lo})^2$$

with y_{hip} the hip height, y_0 the hip height at the moment of lift-off, v_0 the vertical hip velocity at the moment of lift-off, t the current time, g the standard acceleration of gravity and t_{lo} the time at the moment of lift-off.

However, this estimation does not account for friction in the rail system, which introduces errors. To compensate for these inaccuracies, the parameter E_{mult} was introduced in Step 1 as a correction factor.

4.1.3 Phase transitions

As explained at the beginning of this chapter, the control algorithm alternates between three control modes. Therefore, it must incorporate a state machine to determine when to switch between these phases. Ground contact is detected using contact switches embedded in the hopper's foot, allowing the system to distinguish between the flight and stance phases—specifically, to detect transitions from flight to touchdown and from lift-off to flight.

However, during the stance phase, a distinction must also be made between the touchdown and lift-off phases. This is achieved by estimating the vertical velocity of the hip using the deriviation starting from the hip position as a function of actuator angles (see also Equation 3.2 and 3.3):

$$y_{hip} = l_{upp}\cos(\theta_{hip}) + l_{low}\cos(\theta_{hip} + \theta_{knee})$$

$$\Rightarrow \dot{y}_{hip} = v_{y,hip} = -l_{upp}\sin(\theta_{hip})\dot{\theta}_{hip} - l_{low}\sin(\theta_{hip} + \theta_{knee})(\dot{\theta}_{hip} + \dot{\theta}_{knee})$$

When the vertical hip velocity goes below 0.5 m/s, the leg is assumed to have reached its lowest point and is considered ready for lift-off.

4.2 Control method for jumping on trampoline

The control algorithm described above can be extended when it is known that the hopper is jumping on an elastic surface, such as a trampoline. The goal of studying this extension is to determine if a future design would benefit from using a spring under the foot. The extended controller incorporates the elasticity of the ground into both the energy shaping controller and the impedance controller.

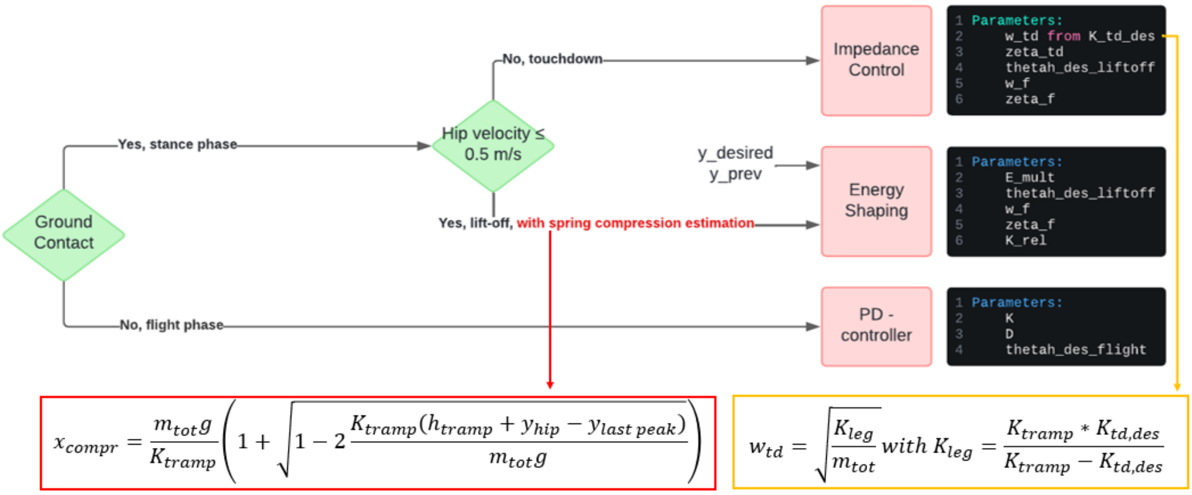

```
Parameters:
    w_td from K_td_des
    zeta_td
    thetah_des_liftoff
    w_f
    zeta_f
```

```
Parameters:
    E_mult
    thetah_des_liftoff
    w_f
    zeta_f
    K_rel
```

```
Parameters:
    K
    D
    thetah_des_flight
```

$$x_{compr} = \frac{m_{tot} g}{K_{tramp}} \left(1 + \sqrt{1 - 2 \frac{K_{tramp}(h_{tramp} + y_{hip} - y_{last\,peak})}{m_{tot} g}} \right)$$

$$w_{td} = \sqrt{\frac{K_{leg}}{m_{tot}}} \, with \; K_{leg} = \frac{K_{tramp} * K_{td,des}}{K_{tramp} - K_{td,des}}$$

Figure 4.3: Control architecture for jumping on trampoline

In the impedance controller, the parameter ω_{td} can be recalculated from its desired value while taking into account the stiffness of the trampoline spring, as indicated in the yellow box in Figure 4.3. This formula is attained by using the formula for two springs in series, namely

$$\frac{1}{K_{leg,des}} = \frac{1}{K_{leg}} + \frac{1}{K_{tramp}}$$

with $K_{td,des} \in \mathbb{R}$ the desired equivalent spring stiffness for the new system, K_{leg} the virtual spring stiffness of the leg and $K_{tramp} \in \mathbb{R}$ the real ground stiffness.

In the energy shaping controller, the calculation of the current energy must also be modified to account for the trampoline's spring compression. Assuming all potential energy at the previous peak is converted into spring energy and gravitational potential energy at the moment of maximum compression, the spring compression can be calculated from the energy balance:

$$\frac{1}{2} \cdot K_{\text{tramp}} \cdot x_{\text{compression}}^2 + m_{\text{tot}} \cdot y_{\text{current}} \cdot g = m_{\text{tot}} \cdot y_{\text{last peak}} \cdot g, \quad \text{with} \quad y_{\text{current}} = h_{\text{tramp}} + y_{\text{hip}} - x_{\text{compression}}$$

with h_{tramp} the unloaded height of the trampoline and y_{hip}, calculated using Equation 3.2, the height difference between hopper hip and hopper foot.

Rewriting this leads to the quadratic equation:

$$x_{\text{compression}}^2 - \frac{2 \cdot m_{\text{tot}} \cdot g}{K_{\text{tramp}}} x_{\text{compression}} + \frac{2 \cdot m_{\text{tot}} \cdot g}{K_{\text{tramp}}} (h_{\text{tramp}} + y_{\text{hip}} - y_{\text{last peak}}) = 0$$

Solving the equation results in:

$$x_{\text{compression}} = \frac{m_{\text{tot}} \cdot g}{K_{\text{tramp}}} \left(1 + \sqrt{1 - 2 \frac{K_{\text{tramp}}(h_{\text{tramp}} + y_{\text{hip}} - y_{\text{last peak}})}{m_{\text{tot}} g}} \right)$$

This expression is highlighted in the red box in Figure 4.3.

Chapter 5

Simulations

In this chapter, the model described in Chapter 3 and the control algorithms presented in Chapter 4 are integrated within the simulation environment.

All simulations take into account the torque and velocity limits of the actuators. In the physical setup, when the torque exceeds the maximum value of 270 Nm, the decoupling system will slip until the torque falls back below this threshold due to the properties of the series clutched actuators. Accordingly, in the simulations, any torque that exceeds 270 Nm is clipped to this maximum value. Actuator velocity is similarly limited to 57 rpm, consistent with the hardware constraints.

Furthermore, the code accounts for the fact that the effective maximum torque may be lower in practice due to actuator inertia $I_{\text{actuator}} = 0.43\, kg\, m^2$. This is modeled using the following relation:

$$T_{\max} = 270\,\mathrm{Nm} - I_{\text{actuator}} \cdot \ddot{q} = 270\,\mathrm{Nm} - 0.43\,\mathrm{kg\,m^2} \cdot \ddot{q}$$

where $\ddot{q}$ is the motor acceleration.

In what follows, the simulation methodology is explained. Next, various experiments are conducted with three main objectives: (1) to evaluate the proposed control strategies, (2) to analyze the impact of different control parameters, and (3) to assess whether the newly developed series clutched actuators improve performance compared to the state-of-the-art.

5.1 Simulation methods

During this master's thesis, two different simulation methods were used. In the initial design phase, a basic self-written simulator was employed to obtain a first estimation of the jumping height and ground reaction forces. However, to evaluate the control algorithms more accurately, a more advanced simulation environment was needed. For this purpose, the PyBullet library in Python was utilized. The two simulation methods differ in their approaches to modeling the equations of motion and in how they integrate motion from a given initial condition.

5.1.1 Self-written simulator

Initially, a self-written simulator was used to perform basic simulations. The mass matrix and forcing matrix were derived using the Euler-Lagrange formulation, with symbolic computation facilitated by the SimPy library in Python. The resulting equations of motion were integrated using a fourth-order Runge-Kutta method. To model ground contact and prevent foot penetration below the ground plane, a virtual spring was implemented beneath the surface.

While this spring-based ground model produced qualitatively realistic jumping motions, it introduced challenges in accurately evaluating control algorithms. Specifically, the presence of a virtual ground spring, which is absent in real-world rigid ground conditions, made direct comparison with physical experiments difficult. Consequently, a more realistic simulation framework was required for control evaluation.

5.1.2 PyBullet simulator

The second simulation method utilizes the PyBullet library in Python. PyBullet employs a Unified Robot Description Format (URDF) file to define the robot's structure and automatically computes the mass matrix and forcing terms. It uses the Euler method for numerical integration and includes built-in functionality for contact detection between multiple objects, as well as the ability to model friction in joints. This simulation framework enables significantly more realistic and accurate simulations compared to the self-written simulator.

As noted above, PyBullet simulations require a detailed URDF file of the robot. In this file, properties of individual links and joints are specified, including link masses, inertias, and actuator constraints such as torque and velocity limits. The URDF connects the physical links by importing STL files and defining their spatial relationships using the robot's Denavit-Hartenberg (DH) parameters.

The DH parameters used in the model are presented in Table 5.1, and the associated coordinate axes are illustrated in Figure 5.1.

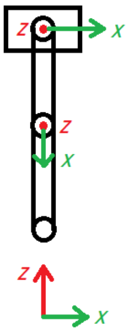

Figure 5.1: Denavit-Hartenberg axes

Table 5.1: Denavit-Hartenberg parameters

Link	d_i **[mm]**	θ_i **[rad]**	a_i **[mm]**	α_i **[rad]**
1	$l_{\text{upp}} + l_{\text{low}} + y_{\text{hip}}$	0	0	$\frac{\pi}{2}$
2	0	$\theta_{\text{hip}} - \frac{\pi}{2}$	l_{upp}	0
3	0	θ_{hip}	0	0

Furthermore, `PyBullet` allows the inclusion of dynamic properties in the simulation. This is particularly useful for modeling joint friction. In all subsequent simulations, unless stated otherwise, the friction values are set to 0.5 Ns/m for the rail—modeled as a prismatic joint—and 5 Nms/rad for the rotational joints. The rail friction value was chosen based on an estimation of the low-friction behavior expected from guiding carriages. The joint friction value was based on a friction analysis of the actuators conducted by Dr. Ostyn prior to the start of this thesis.

5.2 Criteria used to evaluate simulations

Before conducting the actual simulations, it is crucial to establish an evaluation method. The simulations are intended to assess the hopper's potential performance, but certain behaviors must be avoided. The following sections outline those criteria.

5.2.1 Normalized Root Mean Squared Error (NRMSE)

The first criterion for evaluation uses the Normalized Root Mean Squared Error (NRMSE) to compare the actual jump height to the desired height. The NRMSE is calculated as follows:

$$NRMSE = \frac{\sqrt{\sum_{i=1}^{n}(y_{desired,i} - y_{actual,i})^2}}{\bar{y}_{actual}} \in \mathbb{R}$$

where $y_{desired,i}$ and $y_{actual,i}$ are the desired and actual jump heights at the i-th instance, and $\bar{y}_{actual}$ is the average of the actual heights. The result is a non-dimensional value that quantifies the deviation between the desired and actual performance. The NRMSE is used to evaluate the control method according to the following scale:

$$\begin{cases} NRMSE < 10\% & \text{Excellent} \\ 10\% \leq NRMSE < 20\% & \text{Good} \\ 20\% \leq NRMSE < 30\% & \text{Fair} \\ NRMSE \geq 30\% & \text{Poor} \end{cases}$$

5.2.2 Slipping condition

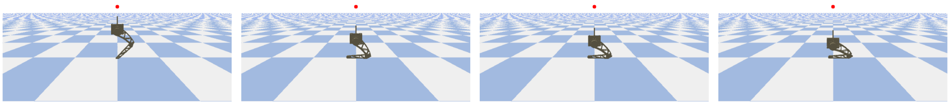

(a) Slip condition: knee touches ground

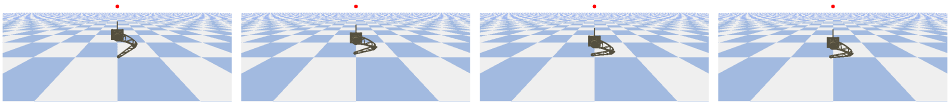

(b) Slip condition: foot vibrates when in contact with ground

Figure 5.2: GIF's of slipping conditions

In addition to the NRMSE, a slipping criterion is used to evaluate the system's performance. The system is considered to slip if one of the following two cases occurs:

1. The robot touches the ground with its knee, as demonstrated in Figure 5.2a.
2. The robot's foot vibrates during landing, as illustrated in Figure 5.2b.

If either of the above conditions occurs during the simulation, it is assumed that the applied controller with those specific control parameters is ineffective, and the control performance is deemed poor.

5.3 Simulation impedance control

For the first simulation, only the leg impedance controller is employed to evaluate this specific part of the control algorithm. Additionally, the simulation is used to identify the impedance limits of the actuators. First, the controller is tested in a trajectory-following task. Then, the same controller is used to determine the maximum achievable dimensionless stiffness.

5.3.1 Position control: following predetermined trajectory

This simulation applies the impedance controller described in Section 4.1.1 for position control. The desired position trajectory is defined in Cartesian space as:

$$y_{\text{desired}} = \begin{cases} 0.6\,\text{m} & 0 \leq t < \frac{T}{3} \\ 0.35\,\text{m} & \frac{T}{3} \leq t < \frac{2T}{3} \\ 0.8\,\text{m} & \frac{2T}{3} \leq t < T \end{cases}$$

where T is the total duration of the simulation.

Since the impedance controller operates in both joint space and Cartesian space, the Cartesian foot position controller can be directly applied. However, for the joint space controller, the desired vertical trajectory must first be translated into joint angles. The following equations are used, assuming a foot offset $e = 0.0\,m$:

$$\theta_{\text{hip, desired}} = \arccos\left(\frac{y_{\text{desired}}}{2l_{\text{upp}}}\right) \qquad \theta_{\text{knee, desired}} = -2\theta_{\text{hip, desired}}$$

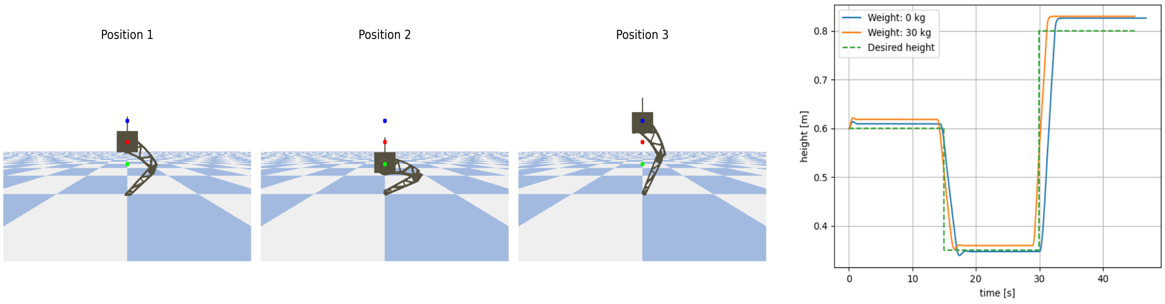

(a) GIF trajectory following

(b) Height plot trajectory following

Figure 5.3: Trajectory following simulation

Figure 5.3a presents selected frames from the simulation GIF, while Figure 5.3b illustrates the trajectory-following performance. As demonstrated in Figure 5.3b, the controller performs accurately and remains robust even when an additional mass of 30 kg is added to the hopper base.

5.3.2 Maximum impedance

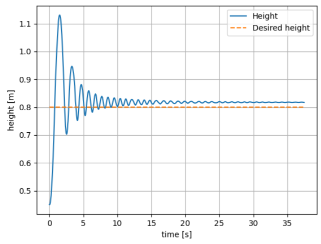

Figure 5.4: Step response in no damping simulation

To enable a comparison between the developed actuators and the state-of-the-art, the maximum dimensionless stiffness is determined. In [14], a dimensionless stiffness $\bar{k} = \frac{kl}{mg} = 10.8$ was achieved in an experiment without damping. This thesis aims to evaluate whether the hopper design can match or exceed this performance. Therefore, the previously described trajectory-following experiment is simplified to a single step—from 0.35 m to 0.8 m—without leg damping. Additionally, the added weight is varied to identify the actuator limits in simulation. The maximum impedance is defined as the highest added weight for which the hopper can still reach the 0.8 m target height.

Due to the absence of damping, some oscillations occur in the system. However, as long as the normalized root mean square error (NRMSE) remains below 0.2, the performance is considered acceptable. Table 5.2 presents the simulation results, while Figure 5.4 illustrates the oscillations observed in the experiment with a 30 kg mass, caused by the lack of damping. The stiffness values listed in Table 5.2 correspond to those used in the simulation experiments.

Table 5.2: Results of the dimensionless stiffness experiment

Mass [kg]	**Stiffness [N/m]**	**Dimensionless Stiffness [-]**	**NRMSE [-]**
0	121	0.815	0.0612
15	289	1.94	0.07
30	484	3.26	0.0707
45	1444	9.72	0.0999
50	2116	14.25	0.134

Table 5.2 demonstrates that the achievable dimensionless stiffness with the newly designed series clutched actuators is 14.25, which is better than the state-of-the-art.

5.4 Simulation of continuous jumping

Once the performance of the impedance controller has been evaluated, the simulation framework is extended to incorporate the full control algorithm. This expanded simulation serves three main purposes: (1) to determine the maximum achievable jumping height of the hopper robot, (2) to analyze the robustness of the controller under varying friction levels and added mass, and (3) to study the influence of different control parameters on performance. An illustration of this simulated experiment is shown in Figure 5.5.

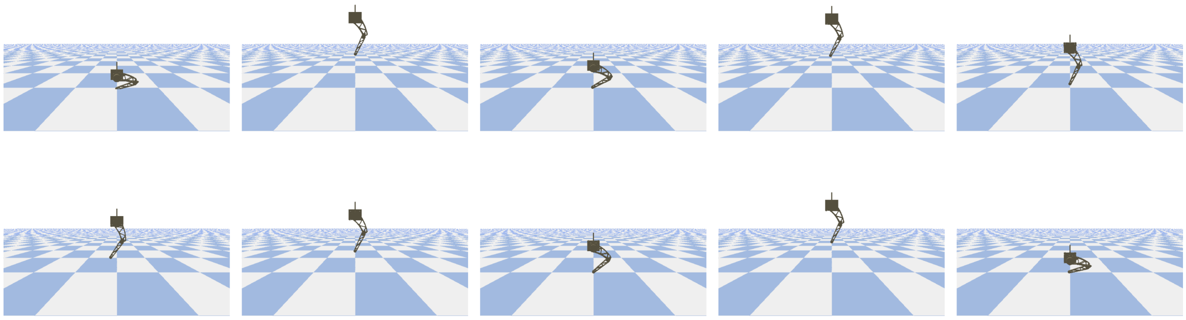

Figure 5.5: GIF of continuous jumping experiment

5.4.1 Maximum jumping height

The maximum jumping height of the hopper robot is a key performance metric. To investigate this, a plot is generated showing the maximum achievable jump height as a function of both linear rail friction and angular joint friction, without any added mass. In this analysis, the slip criterion, explained in Section 5.2, is not considered. The results, shown in Figure 5.6, serve to validate the friction implementation in PyBullet. As anticipated, increasing either form of friction results in a reduced maximum jumping height, confirming the expected behavior.

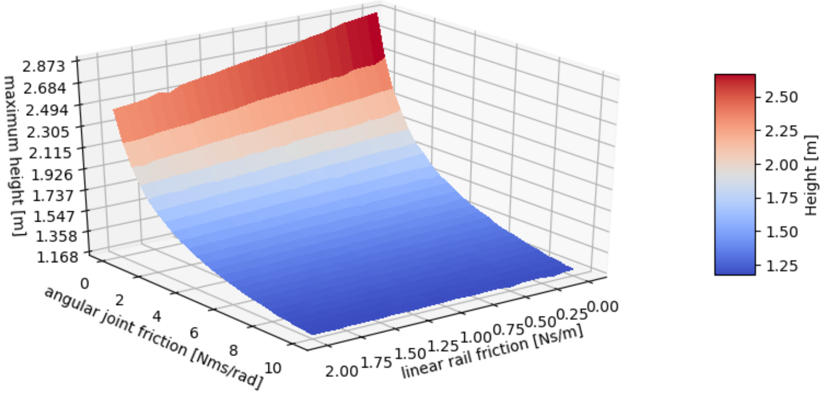

Figure 5.6: Effect of friction on maximum jumping height

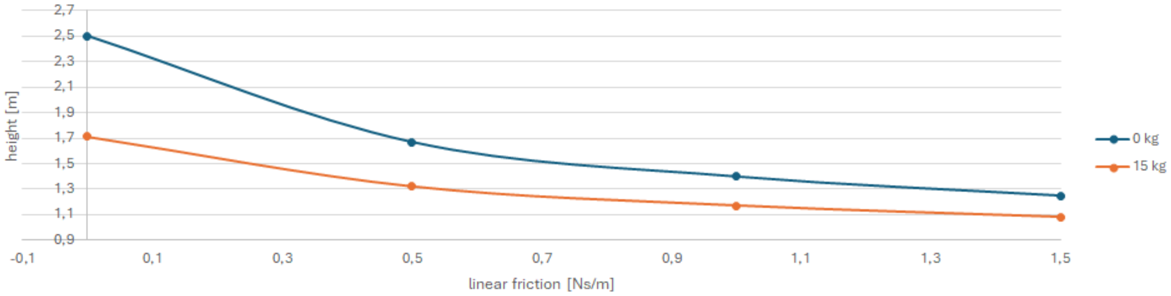

Figure 5.7: Maximum jumping height of hopper robot as a function of friction and added mass

Since the previous plot does not account for slip, it cannot be used to fully evaluate the controller's performance. To address this, an additional analysis was conducted to determine the maximum continuous jumping height of the hopper. In this experiment, the desired jumping height was set to 3 m, and the hopper's ability to repeatedly reach a certain maximum jumping height without slipping was evaluated. This analysis was repeated for multiple values of linear rail friction and varying amounts of added mass, namely 0 kg and 15 kg. The resulting maximum jumping heights are shown in Figure 5.7. As expected, an increase in linear rail friction results in a lower jumping height, and the addition of more weight further reduces the maximum jumping height.

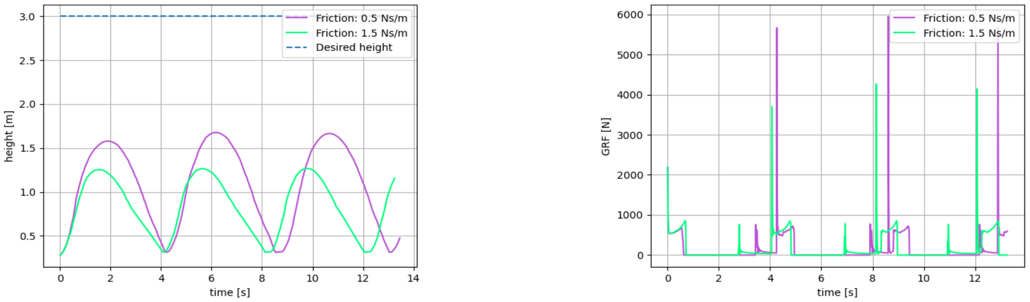

(a) Jumping heights (b) Ground reaction forces

Figure 5.8: Comparison of two continuous jumping experiments with different friction values

Next, two simulations are compared in greater detail: the experiments with 0 kg of added mass and friction values of 0.5 Ns/m and 1.5 Ns/m, respectively. Figure 5.8 presents the jumping heights and ground reaction forces for both experiments. A key observation is that, although the jump with 0.5 Ns/m friction is higher, both jumps take nearly the same amount of time. This is due to the higher friction, which results in lower velocities for the 1.5 Ns/m case. Additionally, as shown in Figure 5.8b, the touchdown ground reaction force is highest for the 0.5 Ns/m case. This can be attributed to the hopper's greater downward acceleration in this scenario resulting in a larger ground reaction force.

5.4.2 Robustness of controller with respect to friction

Continuing with the continuous jumping controller, the performance for a desired height of 1.5 m is analyzed. Initially, by ignoring linear rail friction, the controller is tuned to reach a height of 1.5 m with a resulting NRMSE of 0.00267, as shown in Figure 5.9a. Next, the same simulation is run without retuning, but with a linear rail friction of 0.5 Ns/m. The resulting simulation shows a higher NRMSE value, specifically NRMSE = 0.244, as illustrated in Figure 5.9b. Finally, the experiment is repeated with friction, but this time with the parameter E_{mult} retuned. The result, depicted in Figure 5.9c, demonstrates a performance similar to the first experiment without friction, with an NRMSE of 0.00547. In conclusion, the controller proves to be robust with respect to friction when properly tuned.

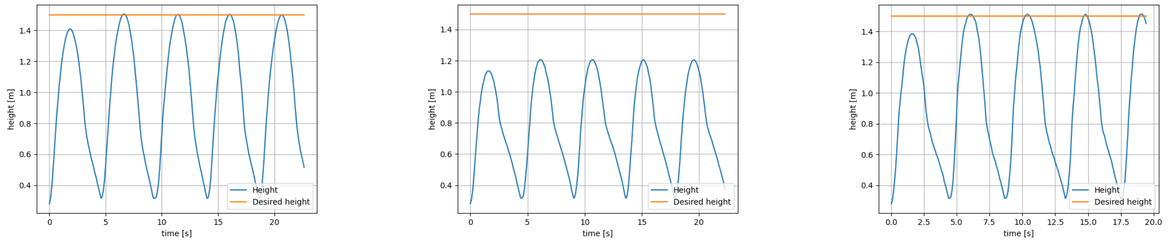

(a) No friction (b) Friction, no change in E_{mult} (c) Friction, change in E_{mult}

Figure 5.9: Robustness of controller with respect to friction

5.4.3 Effect of energy shaping parameter E_{mult}

E_{mult} is the main tuning factor in energy shaping, together with the desired jumping height. In the previous section, it was implied that changing E_{mult} influences the jumping height during tuning. This is because E_{mult} is used in the calculation of the current energy. A very small value of E_{mult} leads to a significant underestimation of the current energy during lift-off phase, which in turn results in the controller calculating higher required torques. This effect is demonstrated in Figure 5.10.

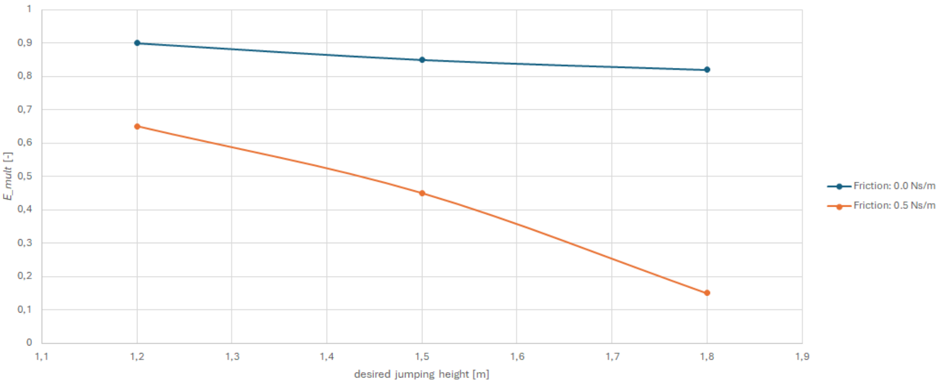

Figure 5.10: Needed values of E_{mult} to reach a certain desired jumping height

Figure 5.10 indeed illustrates that higher desired jumps require a lower value of E_{mult}. Additionally, the figure demonstrates that for higher linear rail friction, the decrease in the needed value of E_{mult} is more pronounced. This is because higher friction introduces more difficulty in reaching the desired heights, necessitating an even lower E_{mult} to compensate.

5.4.4 Effect of leg impedance control parameters

The three parameters for leg impedance control are the frequency, damping ratio, and the desired angle at lift-off. As explained in Section 4.1.1, the frequency and damping ratio are recalculated into a virtual spring-damper system, which controls the hip to the desired position for lift-off. In the following, the optimal values for these parameters will be studied, and the necessary values for continuous jumping will be analyzed.

Figure 5.11 shows how ω_{td} and ζ_{td} influence the NRMSE of the continuous jumping experiment. The graph in Figure 5.11a was generated with a fixed value of $\zeta_{td} = 0.2$, while the graph in Figure 5.11b was generated with a fixed value of $\omega_{td} = 1.0$.

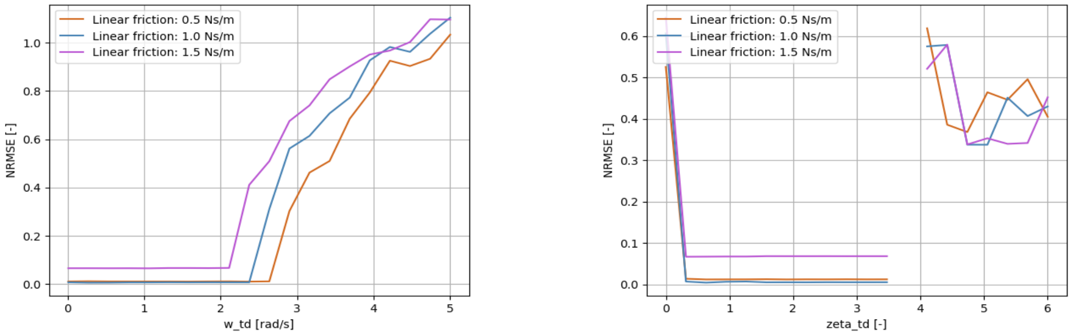

(a) Effect of ω_{td} on NRMSE

(b) Effect of ζ_{td} on NRMSE

Figure 5.11: Effect of ω_{td} and ζ_{td} on the NRMSE of actual jump height compared to desired jump height

In general, if the frequency is too low, the system responds too slowly, while if the frequency is too high, oscillations are induced. Similarly, a low damping ratio results in oscillations that are not damped, while a high damping ratio leads to a slow response. Figure 5.11a demonstrates that ω_{td} only results in good NRMSE values within a limited range. However, lower values of ω_{td} do not seem to cause significant issues, likely because the low frequency, combined with the low damping ratio (ζ=0.2), results in a stable system. A similar optimal range for ζ_{td} is evident in Figure 5.11b. When ζ_{td} is too low, oscillations are prominent, whereas excessively high values lead to a slow response, as expected.

Next, the leg stiffness ($K_{td} = \omega_{td}^2 m_{tot}$) and damping ($D_{td} = 2m_{tot}\omega_{td}\zeta_{td}$) are analyzed. Figures 5.12a and 5.12b respectively show the leg stiffness and damping used in simulations to achieve the maximum continuous jumping heights, as presented in Figure 5.7.

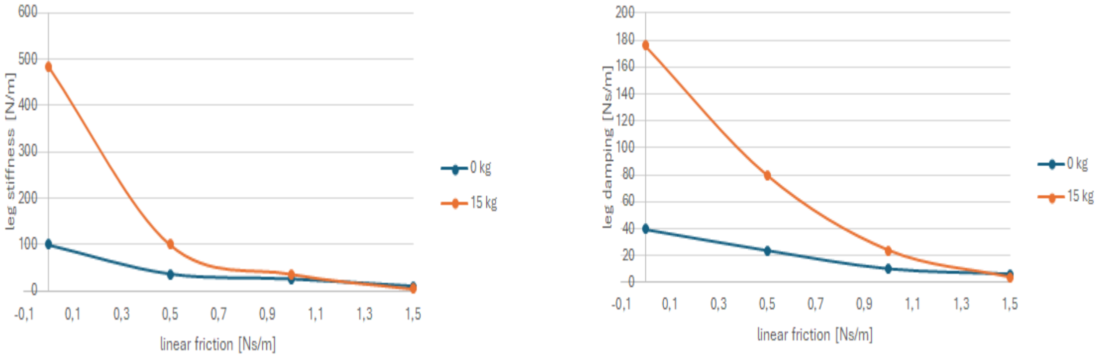

(a) Needed values of K_{td}

(b) Needed values of D_{td}

Figure 5.12: Needed values of K_{td} and D_{td} for continuous jumping experiments

A lower friction coefficient results in a greater continuous jumping height, leading to a higher maximum gravitational potential energy at the peak height. This energy must be transformed into virtual spring energy during buffering, with some portion dissipated through damping. Consequently, higher jumps require both a stiffer virtual spring and a stronger virtual damper. These increased stiffness and damping values demand higher torques from the actuators, aligning with the intuitive notion that jumping higher or landing from greater heights requires more muscle energy. Similarly, when additional weight is applied, even greater muscle effort is needed.

This trend is evident in Figures 5.12a and 5.12b, where larger virtual spring stiffness and damping values correspond to larger jumping heights and added weight.

5.4.5 Effect of the desired angles in different phases

Besides the desired jumping height, there are three other general desired values in the control algorithm: the foot offset (analyzed in Section 5.4.6), the flight angle, and the start angle. The flight angle refers to the angle of the hip during the flight phase, while the start angle is the desired angle of the hip at the moment of switching from the touchdown phase to the lift-off phase.

Figure 5.13 shows the normalized root mean squared error (NRMSE) of the actual jumping height compared to the desired jumping height for a continuous jumping experiment. The graph clearly indicates that a small start angle results in large discrepancies between the actual and desired jump heights, as reflected by high NRMSE values. This observation aligns with intuition: smaller hip angles—corresponding to nearly straight legs—impede effective jumping. Analogous to human jumping behavior, higher jumps are typically achieved by bending the knees, which corresponds to larger start angles. Accordingly, the lowest NRMSE values are observed for the highest start angle value.

Furthermore, the graph reveals an interesting pattern: combinations of small start angles and large flight angles tend to yield lower NRMSE values than a combination of both small start and flight angles. In these scenarios, the leg transitions from an almost straight position to a significantly bent posture during flight, and then extends again for takeoff. Although it is an improvement over the other solutions for small starting angles, it still leads to an NRMSE value of 0.9.

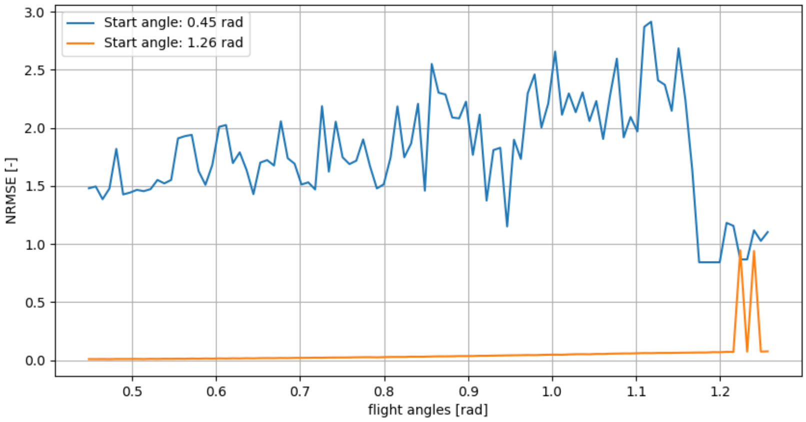

Figure 5.13: Effect of desired angles on NRMSE of actual jump height compared to desired jump height

Additionally, the figure suggests that smaller flight angles generally lead to better NRMSE values than larger ones. This trend is intuitively explained by the fact that landing with straighter knees provides more time for energy buffering. However, at the largest flight angle, the NRMSE improves again. This occurs because the start and flight angles are equal, allowing a jump at constant angle. This is conceptually similar to crouched jumping.

In conclusion, the optimal performance—represented by the lowest NRMSE—is achieved with the largest start angle and the smallest flight angle, as illustrated in Figure 5.13. Additionally, Figure 5.13 shows that the NRMSE is more sensitive to variations in the start angle than in the flight angle.

5.4.6 Effect of foot impedance control parameters

The foot impedance control, as described in Section 4.1.1, is governed by three parameters: a frequency, a damping ratio, and a desired foot offset.

Figure 5.14 illustrates the effect of foot position on controller performance. As shown in the graph, there exists a limited range of stable foot offset values, and the influence of linear rail friction appears to be minimal. The stable region, indicated by the lighter dots in the plot, spans from approximately -2.5 cm to 5.0 cm. This suggests that positioning the foot closer to the knee is generally more stable than shifting it in the opposite direction. Intuitively, this behavior can be explained by the hopper's center of gravity being slightly biased toward the knee side. As a result, the stable interval appears to be centered around the hopper's center of gravity in its fully bent configuration. This behavior mirrors human biomechanics, where stability during jumping and landing is achieved by balancing mass distribution around the contact point.

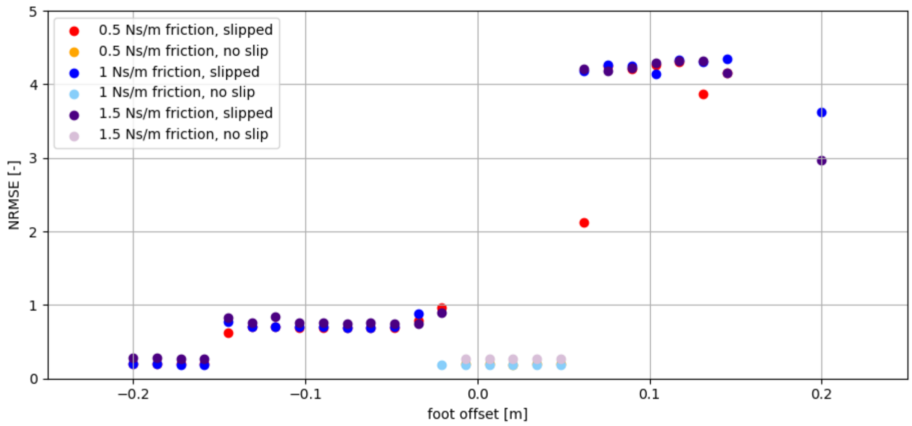

Figure 5.14: Effect of foot offset on NRMSE of actual jump height compared to desired jump height

A virtual spring-damper system, characterized by the frequency ω_{foot} and damping ratio ζ_{foot}, is employed to control the foot's position during the buffering and lift-off phases, preventing slipping. As is typical with spring-damper systems, a low frequency results in a slow response, while an excessively high frequency introduces oscillations. Similarly, a low damping ratio fails to adequately suppress these oscillations, whereas a high damping ratio leads to a sluggish system response. The effects of these parameters are clearly observable in the simulations: a slow foot response due to low ω_{foot}, as well as a fast foot response caused by high ω_{foot}, both contribute to increased slipping and, consequently, higher NRMSE values, as illustrated in Figure 5.15a. Similarly, Figure 5.15b shows that an overly damped system leads to performance degradation, which is again reflected in increased NRMSE.

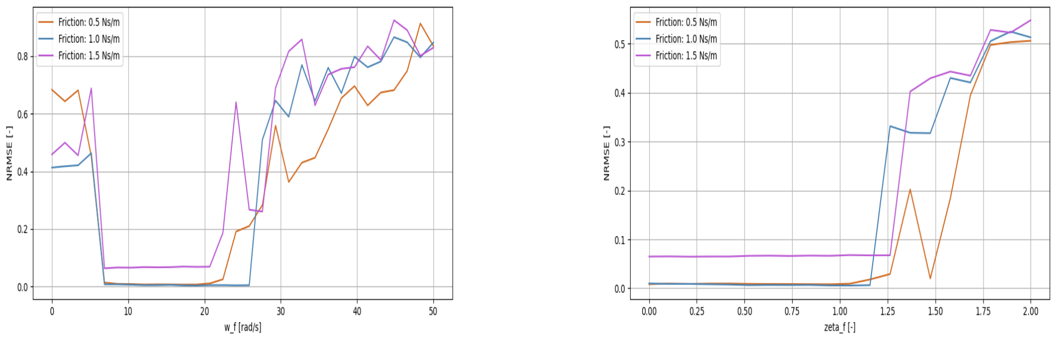

(a) Effect of ω_{foot} on NRMSE

(b) Effect of ζ_{foot} on NRMSE

Figure 5.15: Effect of ω_{foot} and ζ_{foot} on NRMSE of actual jump height compared to desired jump height

5.5 Simulation of trajectory following

The continuous jumping controller described in Section 5.4 can be extended to follow a desired height trajectory. This trajectory tracking simulation provides valuable insights into the control parameter K_{rel}, which is dynamically updated using the following relation:

$$K_{rel} = \frac{E_{desired}}{E_{previous}}$$

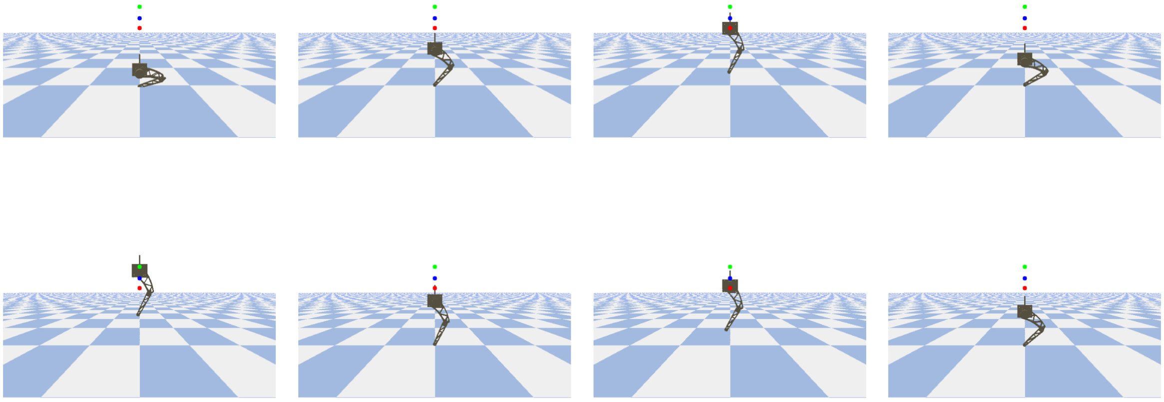

Figure 5.16: Trajectory following simulation visualized as a GIF

The desired jumping height trajectory for this simulation is defined as:

$$y_{desired} = \begin{cases} 1.1 \text{ m}, & 0 \leq t < \frac{T}{3} \\ 1.5 \text{ m}, & \frac{T}{3} \leq t < \frac{2T}{3} \\ 1.3 \text{ m}, & \frac{2T}{3} \leq t < T \end{cases}$$

with T the duration of the simulation.

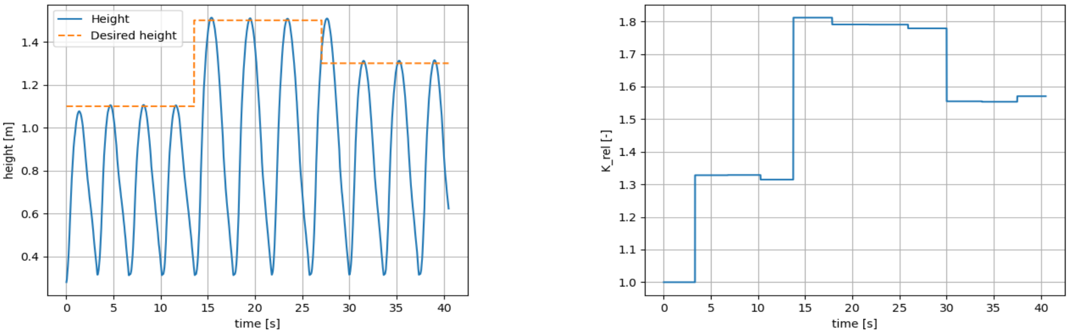

(a) Jumping heights during trajectory following simulation

(b) K_{rel} values during trajectory following simulation

Figure 5.17: Jumping heights and K_{rel} in the trajectory following simulation

In the animation (Figure 5.16), the hopper first jumps to the red dot (1.1 m), then to the blue dot (1.5 m), and finally to the green dot (1.3 m). The resulting jump heights and corresponding K_{rel} values are shown in Figures 5.17a and 5.17b, respectively.

As observed in Figure 5.17a, the abrupt step change in desired jumping height causes one overshoot, where the actual height temporarily exceeds the desired value. While this could be avoided by using a smoother reference trajectory, such a modification is not essential for the purpose of analyzing K_{rel}.

Figure 5.17b further reveals that higher desired jumping heights correspond to higher values of K_{rel}. Additionally, the plot shows that the controller makes small real-time adjustments to K_{rel} to better track the desired height.

5.6 Simulation maximum drop height

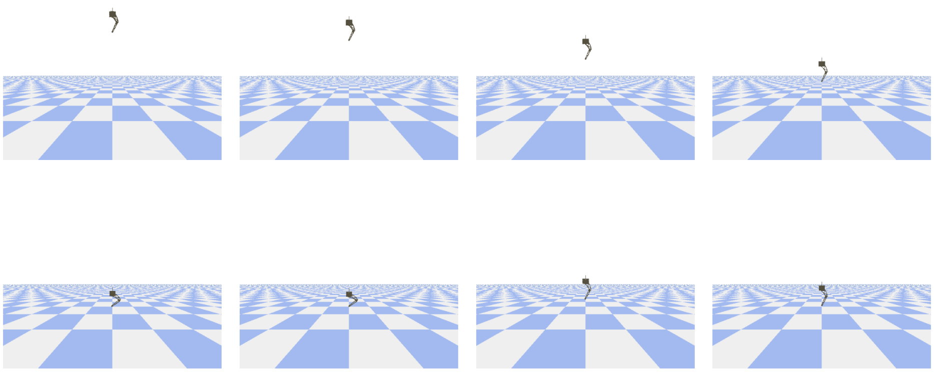

Figure 5.18: GIF of maximum drop height simulation

This simulation aims to determine the maximum height from which the hopper can be dropped such that it can land and perform a controlled jump afterward—meaning the hopper should touch down without slipping. The simulation varies the initial value of y_{hip} and fixes the desired jumping height at 1.5 m. Multiple experiments were conducted with different linear rail friction values and added masses. Table 5.3 summarizes the maximum drop heights obtained under these conditions. Figure 5.18 illustrates simulation number 3 from the table, with a dropping height of 4 m.

Table 5.3: Experimental results of maximum drop height simulations

Nr.	**Linear rail friction [Ns/m]**	**Mass [kg]**	**Max drop height [m]**	**Used drop height [m]**
1	0	0	3.2	3.2
2	0	15	1.5	1.5
3	0.5	0	∞	2.5
4	0.5	15	∞	2.5
5	0.5	32	1.5	1.5

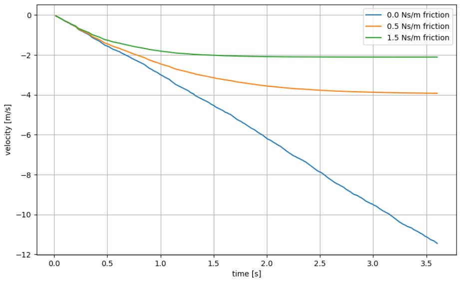

Figure 5.19: Velocity profile for different linear friction values

A key observation from Table 5.3 is that increased linear friction allows for a significantly greater maximum drop height compared to the no-friction case. Without linear rail friction, the falling velocity continuously increases, and the impact velocity is directly given by $v_{impact} = \sqrt{2gh_{initial}}$. Consequently, a higher initial drop height requires more energy to be converted from kinetic energy into virtual spring energy during the buffering phase. However, in the presence of nonzero linear friction, the velocity saturates at a terminal value determined by the system's mass and friction. As shown in Figure 5.19, this leads to a lower impact velocity compared to the frictionless case, even when dropped from greater heights.

To reduce the need for extreme heights, added mass is introduced to reach higher impact energies within reasonable drop heights. This also serves to test the limits of the actuators, as they must absorb more energy during buffering.

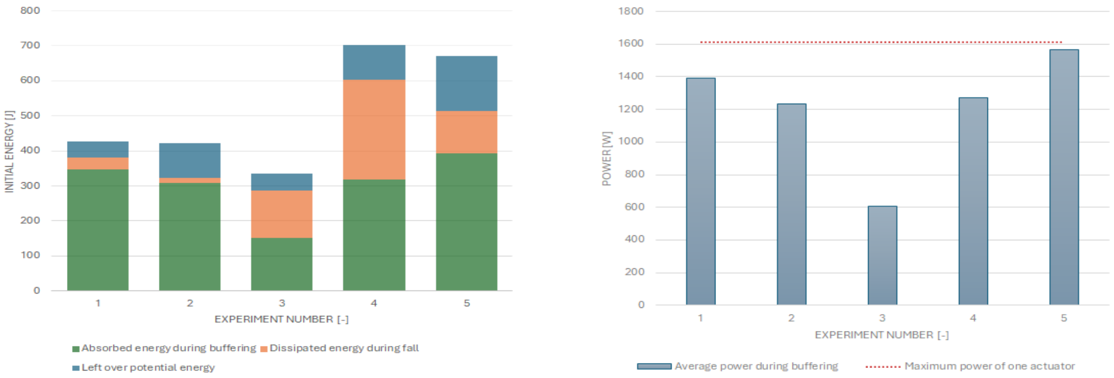

(a) Energy breakdown per experiment

(b) Average power during buffering phase

Figure 5.20: Analysis of maximum drop simulations

The energy and average power plots in Figure 5.20 provide further insight into the system's behavior. In each experiment, the initial gravitational potential energy is transformed into energy stored in the virtual spring-damper system, energy dissipated through friction, and the remaining gravitational potential energy at the lowest point. For cases where the drop height could theoretically be increased indefinitely, a drop height of 2.5 m was selected for the subsequent analysis. In all other cases, the maximum feasible drop height was used. These values are also presented in the last column of Table 5.3.

In Experiments 1 and 2, the initial gravitational potential energy is nearly the same: Experiment 1 uses a higher drop height, while Experiment 2 compensates with greater mass. Minimal energy is lost to friction, as both have zero rail friction. Minor losses shown are most likely due to phase distinction errors and numerical errors. The average power during buffering is near the actuators' maximum, indicating the drop height was well-tuned.

Experiment 3 introduces friction without added mass. The lower initial energy and reduced impact velocity result in less absorbed energy and a lower amount of needed average power during buffering—suggesting the actuator limit was not yet reached.

Experiment 4 builds on this with a 15 kg mass. Although velocity is still capped by friction, the added mass increases kinetic energy at impact. This requires greater energy absorption, reflected in a higher average buffering power.

In the final experiment, an additional 17 kg (32 kg total) is added, further raising the initial energy. The buffering system absorbs the highest energy yet, with average power nearing actuator limits—thus identifying a practical limit for safe landing and controlled jumping.

5.7 Simulation continuous jumping on trampoline

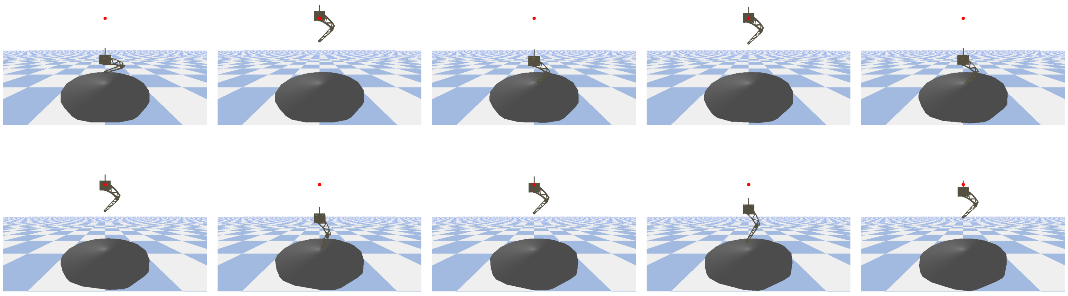

Figure 5.21: GIF of maximum drop height simulation

This simulation is used to evaluate the extended control algorithm proposed in Section 4.2 and its effects on various control parameters. Figure 5.21 shows the GIF of a continuous jumping simulation performed on a trampoline, with the red dot being the desired height.

5.7.1 Evaluation control algorithm with added spring

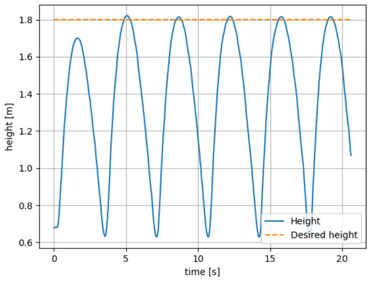

Figure 5.22: Jumping height when applying extended controller

Once the trampoline is incorporated into the control algorithm as described in Section 4.2, the continuous jumping experiment is repeated. The resulting animation is shown in Figure 5.21, and the corresponding jumping heights are depicted in Figure 5.22. As demonstrated in Figure 5.22, the desired jumping height is tracked with high accuracy, indicating that the modified controller for jumping on a trampoline (or linear spring surface) performs as expected. This simulation is further repeated for various values of trampoline spring stiffness, and the resulting maximum jumping heights are compared to those achieved on rigid ground. The outcomes are presented in Figure 5.23, which shows a clear trend: as spring stiffness increases, the improvement in jumping height also increases. The improvement characteristic is calculated by

$$\text{percentage of improvement} = \frac{\text{max height trampoline - max height ground}}{\text{max height ground}} \cdot 100$$

with *max height trampoline* the maximum jumping height of the hopper on a trampoline and *max height ground* the maximum jumping height of the same hopper on the ground.

Low spring stiffness leads to larger trampoline displacements upon contact. For displacements exceeding $x = \frac{mg}{k} = 0.2\,\text{m}$, the leg touches the ground. To maintain a safety margin of $10\,\text{cm}$—i.e., allowing a maximum trampoline displacement of $0.1\,\text{m}$—the minimum required stiffness is approximately $k = 1336\,\text{N/m}$. This value closely corresponds to the point where the improvement curve transitions to positive values. Additionally, at lower stiffness values, the contact time between the leg and the trampoline is longer. This results in a lower peak contact force, causing the leg to lose energy to the spring instead of efficiently utilizing it within the energy shaping control framework.

Although the ground is theoretically modeled by infinite stiffness (and one might expect the improvement curve to eventually decline), this trend was not observed in the simulation. Instead, higher stiffness values continued to yield better jumping performance. This anomaly could stem from simulation errors or the use of a time step that is too large. A smaller simulation step size would allow for more accurate ground contact detection and help prevent the leg from sinking below the surface between simulation steps. Nevertheless, such numerical inaccuracies are inherent and cannot be completely eliminated, even with minimal time steps.

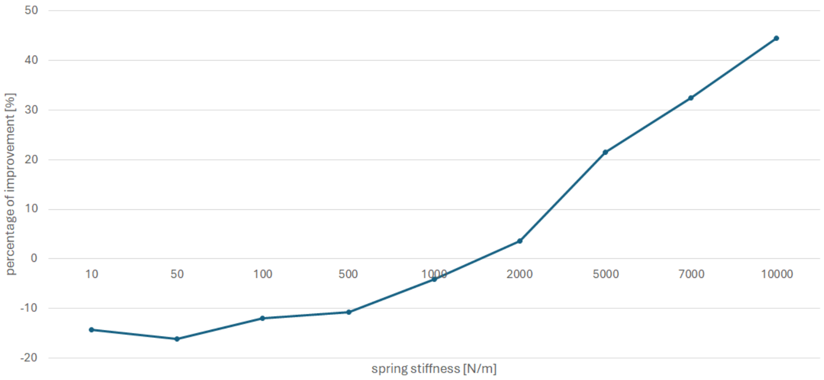

Figure 5.23: Improvement of maximum jump height for different values of ground stiffness

5.7.2 Effect of ground stiffness

As mentioned in Section 5.7.1, a smaller ground stiffness results in a longer contact duration between the leg and the trampoline. This effect is also clearly illustrated in Figure 5.24. A higher ground stiffness leads to a larger ground reaction force concentrated over a shorter time span, while a lower stiffness results in a smaller force distributed over a longer period. This phenomenon is depicted in Figure 5.24a. Figure 5.24b further supports this observation by displaying the relative duration of different control phases for various ground stiffness values. It is evident that as ground stiffness increases, the proportion of time spent in the touchdown and lift-off phases—i.e., the phases involving ground contact—decreases.

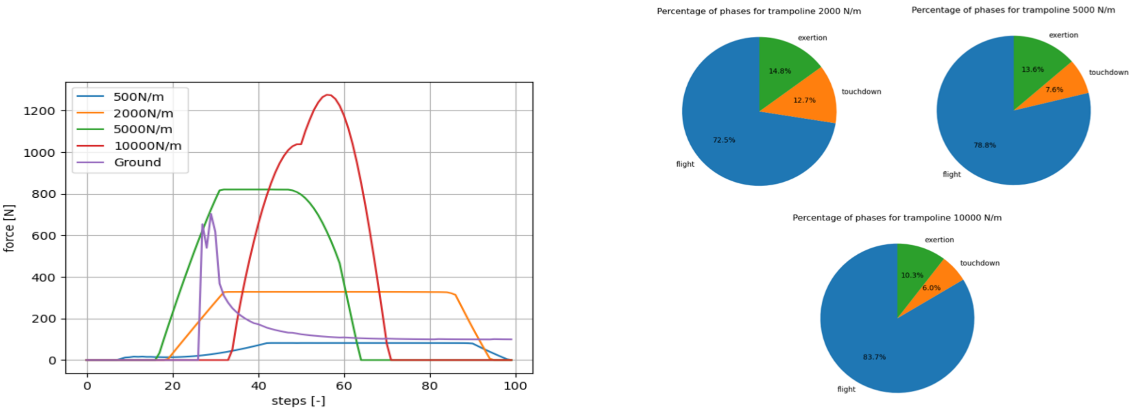

(a) Ground reaction forces for different values of ground stiffness

(b) Phases for different values of ground stiffness

Figure 5.24: Characteristics of interaction between leg and trampoline

5.7.3 Effect control parameters impedance control

Similarly to the analysis in Section 5.4, the effect of different control parameters can be evaluated. This paragraph focuses on the evaluation of the impedance control parameters during touchdown, namely ω_{td} and ζ_{td}, using their recalculated forms K_{td} and D_{td}. This choice is made because it is more intuitive to compare the effects of the virtual spring-damper parameters to results obtained without an elastic ground.

As concluded in Section 5.4, higher jumping heights require more energy for both jumping and landing. This observation is reaffirmed in the present analysis, as illustrated in Figure 5.25. Moreover, Figure 5.23 demonstrated that higher ground stiffness results in higher achievable jumps. Consequently, the required values of the virtual spring constant K_{td} and damping coefficient D_{td} also increase with ground stiffness to adequately manage the increased energy during touchdown.

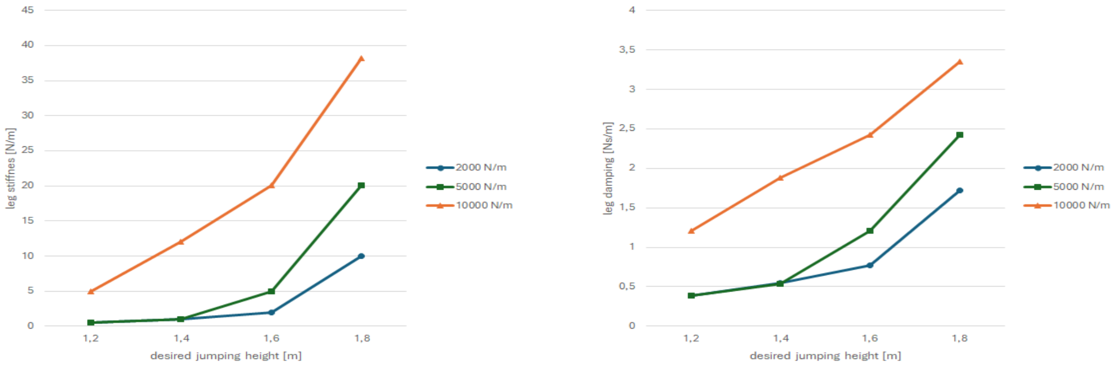

(a) Effect of K_{td}

(b) Effect of D_{td}

Figure 5.25: Needed values of K_{td} and D_{td} for continuous jumping experiments on trampoline for different values of desired jumping height and ground stiffness

5.7.4 Effect control parameter E_{mult}

Next, the effect of the control parameter E_{mult} on the trampoline control algorithm is studied. In the case without a trampoline, lowering E_{mult} led to higher jumping heights. Figure 5.26 illustrates that the same effect occurs in the presence of a trampoline. However, for higher spring stiffness values, reaching the desired heights becomes easier, and thus no underestimation of the energy during the lift-off phase is necessary. On the contrary, for lower stiffness values, achieving the desired jumping heights requires a significant decrease in E_{mult}.

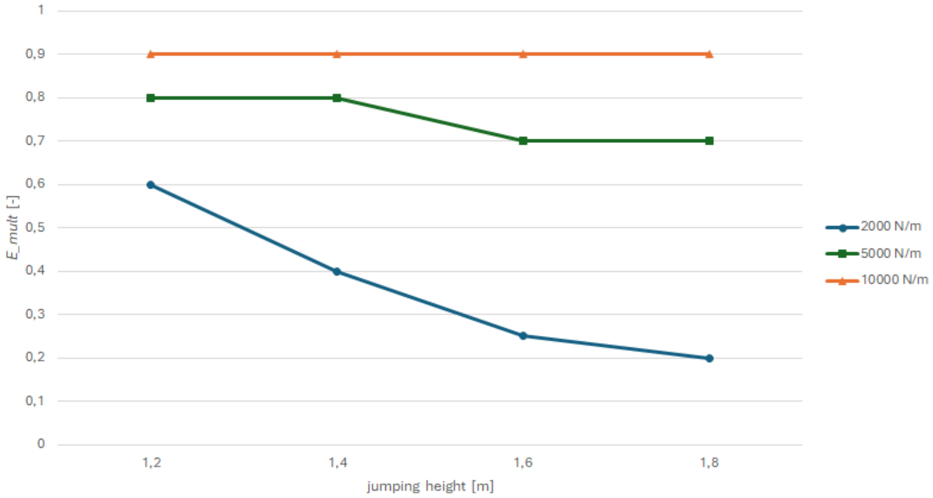

Figure 5.26: Effect E_{mult}

5.7.5 Effect start and flight angle

This paragraph studies the effect of the leg angles. In the case without an added spring under the foot, it was observed that a larger start angle improved jump control, while lower flight angles contributed to more stable landings. However, the influence of the flight angle was considerably smaller compared to the effect of the start angle. This analysis is now repeated by evaluating the maximum controllable jumping height for different combinations of start and flight angles, under ground stiffness values of 2000 N/m and 10000 N/m.

Figure 5.27a and Figure 5.27b illustrate the effects of the start and flight angles in the case of an added spring. The analysis demonstrates that for both considered stiffness values, the maximum controllable jump height increases with increasing start angle and decreases with increasing flight angle. Intuitively, this behavior aligns with human jumping dynamics: initiating a jump with more bent knees enables greater propulsion, while landing with slightly bent knees provides a longer duration for buffering the impact.

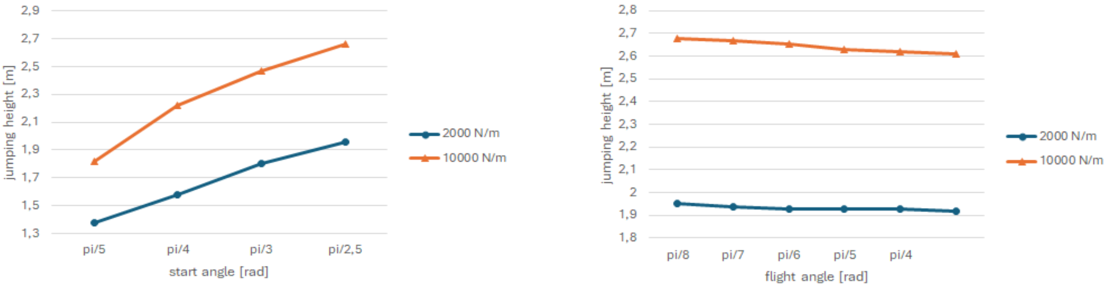

(a) Effect start angle

(b) Effect flight angle

Figure 5.27: Effect of start and flight angle on maximum jumping height

5.8 Conclusions from simulations

The goal of the simulations was to evaluate the control algorithms, analyze the effects of different control parameters, and assess whether the newly designed actuators could outperform the state-of-the-art. The results showed that increased friction, smaller starting angles, and larger flight angles led to lower jumping heights. On the contrary, decreasing E_{mult} resulted in higher jumping heights. Furthermore, higher jumping heights required larger values of K_{td} and D_{td}, while also considering the stable intervals of ω_{td} and ζ_{td}. The foot position during control should ideally be underneath the hip or slightly moved toward the center of gravity, in the direction of the knee. For this control, the stable intervals of ω_{foot} and ζ_{foot} should also be taken into account. All these findings hold true for both control scenarios, with and without the trampoline.

When compared with the state-of-the-art, the maximum jumping height relative to leg length could be either higher or lower, depending on the specific friction value. Therefore, simulations alone cannot conclusively determine this measure unless the linear rail friction is precisely known. Nevertheless, the maximum dimensionless stiffness determined in the simulations was 14.25, which is larger than the maximum value reported in the literature. This suggests that the newly designed actuators may provide superior buffering performance compared to the current state-of-the-art.

Chapter 6

Experimental validation

The goal of the experimental part of this thesis is to validate the results found in simulation. The experiments are executed on two setups: one designed in Chapter 2 and the other at the Deutsches Forschungszentrum für Künstliche Intelligenz (DFKI) in Bremen. The first setup is used to validate the improved value of dimensionless stiffness with respect to the state-of-the-art and to determine the limits of the newly designed actuators. The second setup is used to evaluate whether a spring would indeed increase the jumping height.

6.1 Experimental setup Ghent

The experimental setup consists of the hopper designed in Chapter 2, controlled by a programmable logic controller (PLC). The PLC, implemented using Twincat Beckhoff, connects with the robot leg and operates at a control frequency of 1 kHz. It translates structured text code into actuator movements. The actuators are powered by a 230 VAC source, which is converted to a single-phase power. This entire setup is connected to an emergency stop button for safety.

As the code is written in structured text, no simulations can be run on the hardware. Therefore, several steps were taken to avoid unsafe situations. Initially, a position control experiment was conducted using two dummy motors. Subsequently, one of the dummy motors was replaced with an actual actuator connected to the hopper, but without the full leg attached. The same experiment was then performed with the complete leg assembly, where the two actuators were placed at the center of the rails with the leg hanging. Finally, the leg setup was placed on the ground, and experiments for comparison with the state-of-the-art were conducted.

In what follows, the results of the multiple position control experiments will be analyzed. Furthermore, an experiment is utilized to analyze the linear rail friction. Next, the final experiment will be compared with a position control simulation, such as the one described in Section 5.3.2, to validate those simulation results.

6.1.1 Experiment 1: two dummy actuators

The first experiment is a position control test of two dummy actuators each connected to a lever, as shown in Figure 6.1a.

Figure 6.1b shows the different joint positions during the experiment. Initially, the levers are programmed to move to a starting position, which later serves as the initial position for the actuators such that the leg lifts off from its resting point. The levers then transition to a first desired position, followed by a second, and finally return to the initial position. This sequence mimics the final position control logic to be used with the complete leg setup: transitioning between predefined positions, with the final one held until interrupted via the control code.

The control system is programmed to move on to the next target only if both levers have reached their current desired positions. For the first target, the system proceeds immediately; for the second, it must hold the position for several seconds. The final target (which is the same as the initial one) is held

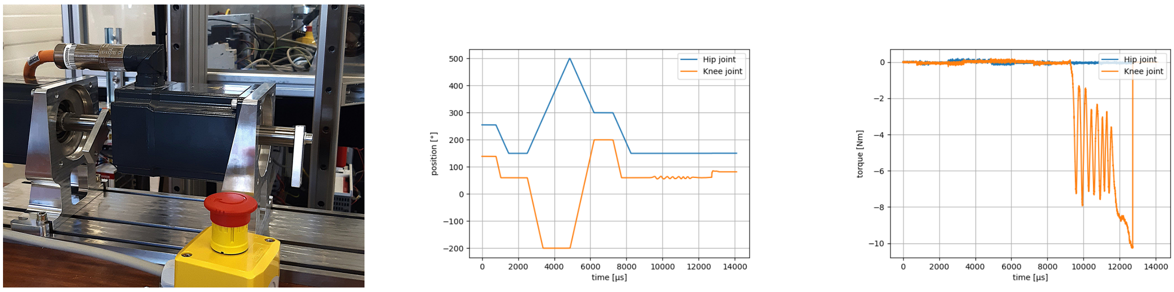

(a) Setup (b) Joint positions (c) Joint torques

Figure 6.1: Experiment 1: position control using two dummy actuators

indefinitely until explicitly stopped.

This final holding phase is critical to test the safety features of the system. As previously mentioned, the multi-step validation process ensures safe operation before moving to the full actuator setup. To complement the emergency stop button, additional software safety measures are implemented and tested in this and the following setups. These include position, velocity, and torque limits.

To validate the torque limit function, the knee lever is manually pulled while in the final position, simulating a scenario where the leg encounters unexpected resistance. The torque threshold for this test is set to 10 Nm. Figure 6.1c confirms that the actuator output torque drops to 0 Nm when the threshold is exceeded, demonstrating that the safety system is functioning as intended and that the experimental setup is safe to be upgraded.

6.1.2 Experiment 2: one dummy actuator and one actual actuator

Figure 6.2 depicts the upgraded experimental setup. In this configuration, the hip dummy actuator is replaced by the actual actuator intended for use in the final leg assembly, while the knee joint still employs a dummy motor.

As in Experiment 1, the actuator and dummy motor are programmed to follow a predefined position pattern, starting and ending at a desired initial state. In this setup, the dummy motor is connected to a lever, and the actual actuator drives half of the upper leg structure. This arrangement is used to test whether exceeding the torque threshold triggers the correct safety response, specifically ending the control.

An additional improvement in this experiment is the synchronization of the movements of the hip and knee actuators. Synchronization is essential in the final configuration to ensure stable and coordinated leg motion. Figure 6.3a confirms the synchronized joint trajectories.

To test the torque safety function, the maximum torque of the hip actuator is set to 1 Nm. During the final hold phase of the position pattern, the upper leg is manually pulled, causing the measured torque to exceed this threshold. As a result, both joints are commanded to apply 0 Nm torque, deactivating further control actions. This behavior is confirmed in Figure 6.3b, verifying that the implemented safety mechanism operates as intended.

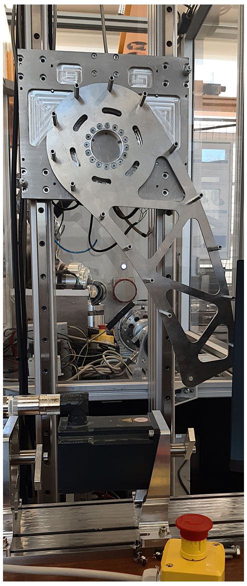

Figure 6.2: Setup 2

6.1.3 Experiment 3: two actual actuators

Figure 6.5 shows the upgraded experimental setup, in which both actuators are those intended for the final leg design, while the leg remains suspended from the rails.

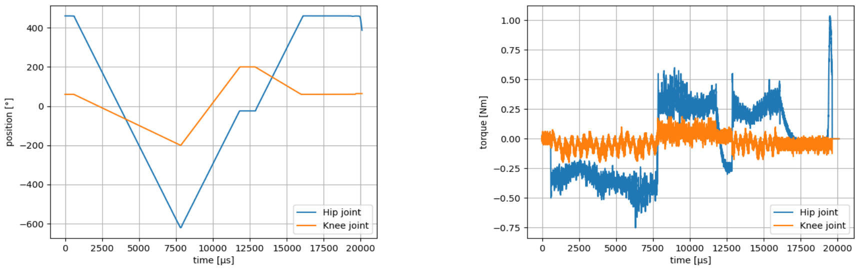

(a) Joint positions

(b) Joint torques

Figure 6.3: Setup 2 experimental results

As in the previous setups, the actuators are programmed to follow a predefined position trajectory, beginning and ending at a desired initial state. The leg first moves to an almost fully stretched position, followed by a transition to its most bent configuration. Subsequently, it moves to an intermediate position before returning to the initial, nearly fully extended state. During the entire motion, the two actuators operate synchronously to ensure coordinated leg behavior. Figure 6.4a illustrates this smooth and synchronized position control.

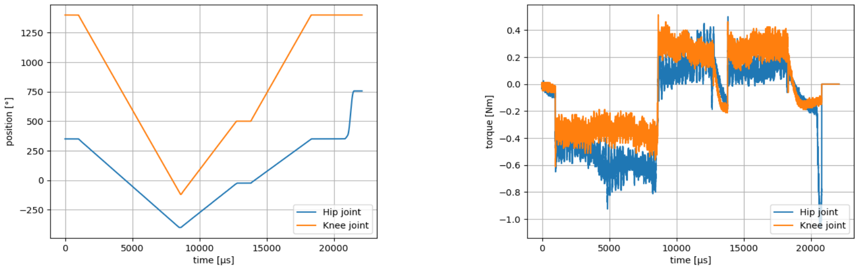

(a) Joint positions

(b) Joint torques

Figure 6.4: Setup 3 experimental results

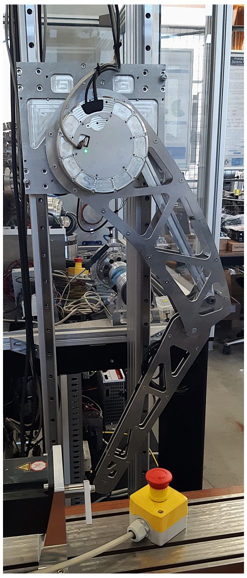

Figure 6.5: Setup 3

To verify the torque safety mechanism, the maximum torque limit for both actuators is set to 1 Nm. During the final position hold, an external disturbance is applied by manually pulling the lower leg. This disturbance causes the measured torque to exceed the predefined threshold, which correctly triggers the safety mechanism and results in both joints being commanded to 0 Nm. Figure 6.4b confirms this behavior.

The successful activation of the safety response in this final configuration, combined with the validated results of the previous setups, demonstrates the reliability and robustness of the control algorithm. In particular, it confirms that the system is safe for progression to the final experimental phase.

6.1.4 Experimental analysis of linear rail friction

In Section 5.8, it was stated that no conclusive statement could be made regarding the improvement of the dimensionless jumping height due to the unknown linear rail friction. To address this, data from a position control experiment is used to estimate the linear rail friction. The objective of the experiment was to determine whether a simple position control strategy could enable the hopper to jump by increasing acceleration and jerk without exceeding a torque limit of 200 Nm for safety.

The highest actuator acceleration obtained without exceeding the torque limit was 199000°/s² at the motor output. Despite this, the hopper did not achieve lift-off, making this dataset suitable for estimating the linear rail friction. This estimation can subsequently be used to predict the achievable jumping height and assess whether it surpasses the performance of state-of-the-art systems.

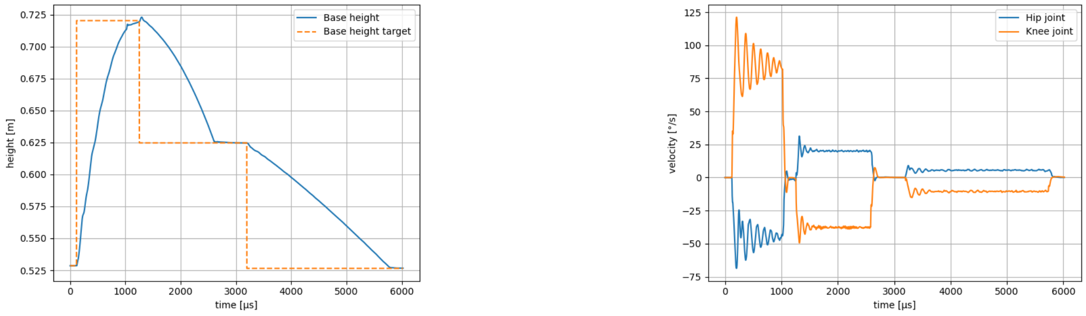

(a) Base height

(b) Joint velocities

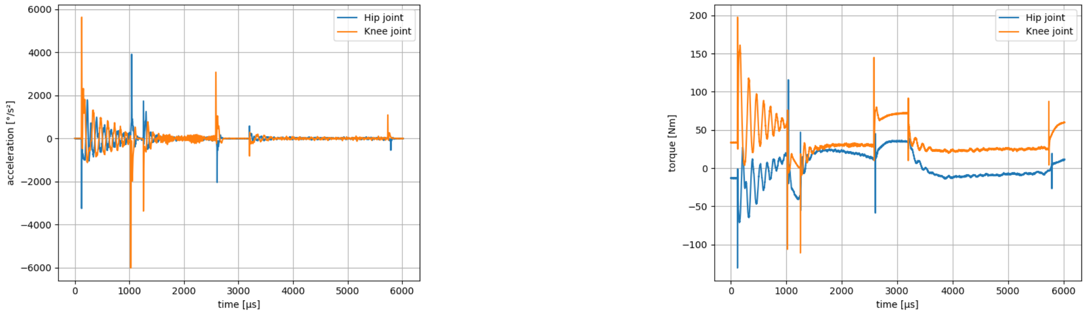

(c) Joint accelerations

(d) Joint torques

Figure 6.6: Data ground test for linear rail friction estimation

As in previous experiments, the actuators follow a predefined position trajectory. The initial posture is a low, bent configuration near the ground to ensure safety—any instability would lead to downward collapse, minimizing mechanical risk. This pose also corresponds to the passive configuration under gravity. The trajectory involves extending the leg to a nearly straight position, moving into a squat-like pose, and returning to the fully bent state.

Figure 6.6 presents the data from this experiment. Unlike previous sections, which reported motor output data, the plots here reflect values at the actuator output, accounting for the gear ratio of 1:19. The conversions are given by:

$$\begin{aligned}\text{position}_{\text{act}} &= \frac{\text{position}_{\text{motor}}}{19}\\ \text{velocity}_{\text{act}} &= \frac{\text{velocity}_{\text{motor}}}{19}\\ \text{acceleration}_{\text{act}} &= \frac{\text{acceleration}_{\text{motor}}}{19}\\ \text{torque}_{\text{act}} &= \text{torque}_{\text{motor}} \cdot 19\end{aligned}$$

The hip base height and vertical velocity are computed as (see also Equation 3.2 and 3.3):

$$y_{\text{hip}} = l_{\text{upp}} \cos(\theta_{\text{hip}}) + l_{\text{low}} \cos(\theta_{\text{hip}} + \theta_{\text{knee}})$$

$$v_{y,\text{hip}} = -l_{\text{upp}} \dot{\theta}_{\text{hip}} \sin(\theta_{\text{hip}}) - l_{\text{low}} (\dot{\theta}_{\text{hip}} + \dot{\theta}_{\text{knee}}) \sin(\theta_{\text{hip}} + \theta_{\text{knee}})$$

Using this data, a power balance is performed:

$$P_{\text{act}} = P_{\text{jointFrictions}} + P_{\text{jointInertias}} + P_{\text{gravity}} + P_{\text{railFriction}}$$

with:

- $P_{\text{act}} = P_{hip} + P_{knee} = \tau_{hip} \cdot \dot{\theta}_{hip} + \tau_{knee} \cdot \dot{\theta}_{knee}$, the sum of the powers delivered by the two actuators
- $P_{\text{jointFrictions}} = c_{act} \cdot (\dot{\theta}^2_{hip} + \dot{\theta}^2_{knee})$, the sum of the lost power in the actuators due to joint friction, with $c_{act} = 5\,\text{Nms/rad}$ the joint friction
- $P_{\text{jointInertias}} = I_{act} \cdot (\ddot{\theta}_{hip} \cdot \dot{\theta}_{hip} + \ddot{\theta}_{knee} \cdot \dot{\theta}_{knee})$, the sum of the power going to the inertia of the actuators, with $I_{act} = 0.43\,\text{kgm}^2$
- $P_{\text{gravity}} = \frac{dE_{\text{grav}}}{dt}$, the power needed to change the hip base height from one gravitational potential energy to the next
- $P_{\text{railFriction}} = -b_{rail} \cdot v^2_{hip}$, the power lost to linear rail friction with b_{rail} the linear rail friction value

When for every timestep those powers are calculated, an estimation of the linear friction value is made at every point in time by:

$$b_{rail,i} = -\frac{P_{\text{act},i} - P_{\text{jointFrictions},i} - P_{\text{jointInertias},i} - P_{\text{gravity},i}}{v^2_{hip,i}}$$

when $v_{hip,i} \neq 0$ and using $b_{rail,i} = 0$ when $v_{hip,i} = 0$.

After applying smoothing techniques to reduce numerical noise, the estimated rail friction is plotted in Figure 6.7a. The average value is found to be 2.28 Ns/m, which is then used in simulation to estimate the hopper's performance. The resulting maximum jumping height is 1.15 m, yielding a dimensionless jumping height of:

$$\bar{h} = \frac{1.15\,\text{m}}{0.9\,\text{m}} = 1.28$$

The relatively high friction can be attributed to several assembly choices. In the first assembly, the linear rails were mounted using only two bolts, leaving much of the middle section free to vibrate. Additionally, the cable routing was not yet optimized for dynamic motion, introducing further resistance.

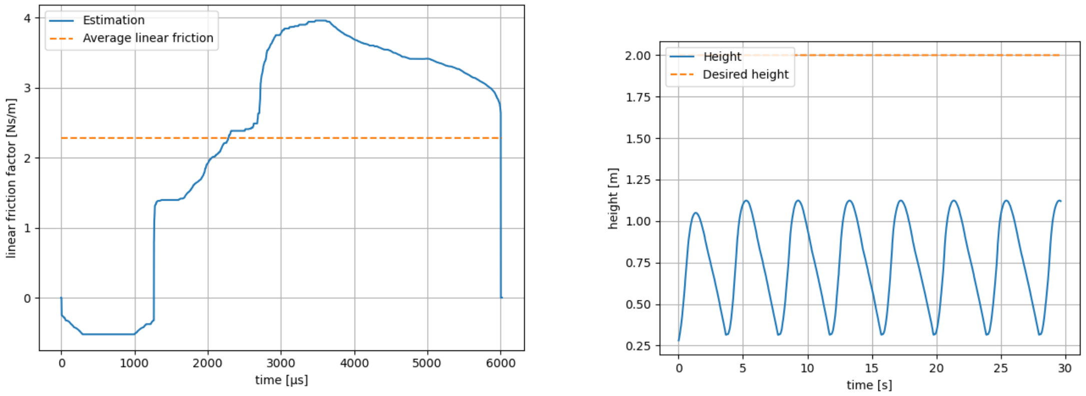

(a) Estimation

(b) Simulated maximum height

Figure 6.7: Linear rail friction estimation

The value of 2.28 Ns/m will be used in subsequent simulations to assess improvements in dimensionless maximum stiffness relative to the state-of-the-art.

6.1.5 Experimental validation of simulation results

To compare the performance of the newly developed actuators with the state-of-the-art, the maximum achievable impedance limits must be determined experimentally, following a similar approach as described in the simulation study in Section 5.3.2. However, due to the unavailability of weights up to 50 kg, a direct comparison under full loading conditions is not feasible. Instead, validation is performed by comparing the impedance control simulation without added mass to an experimental position control scenario under the same unloaded condition.

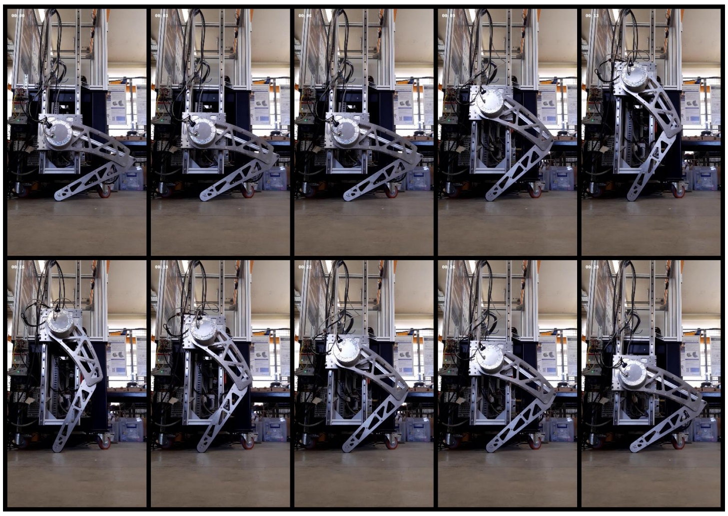

Figure 6.8: Screenshots from video experiment

A similar experiment to the one described in Section 6.1.4 is performed, in which the position controller begins from a bent configuration, transitions to an almost fully extended posture, and then returns to the initial bent position. A short pause is introduced in the squatted and extended configuration. To ensure safe and stable operation during the entire trajectory, the maximum commanded joint velocity is constrained to 200°/s at the motor shaft.

Figure 6.8 shows screenshots taken from the video of the experimental execution. The same motion trajectory is replicated in simulation to allow for comparison of joint torque profiles and hip height evolution.

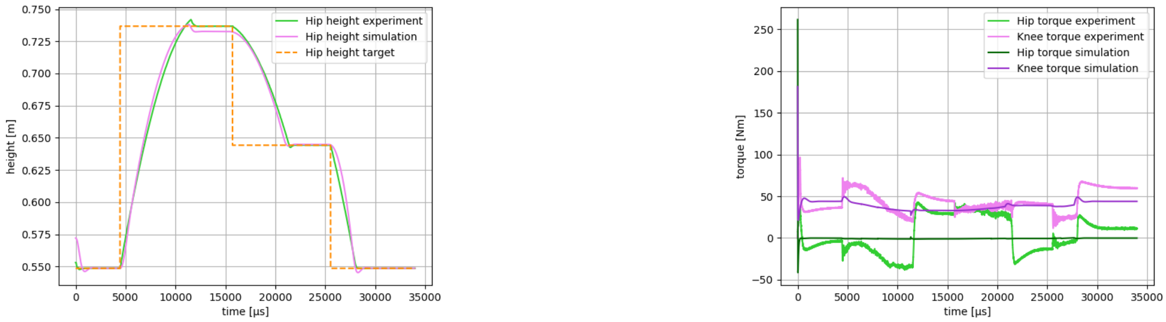

(a) Heights

(b) Torques

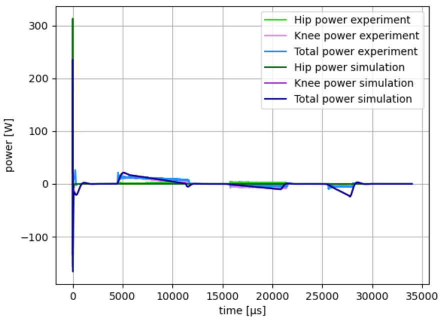

(c) Powers

Figure 6.9: Comparison between simulation and experimental results

Figure 6.9 presents a direct comparison between the experimental and simulated results, including joint torques, joint powers, and hip base heights throughout the trajectory. While the simulation demonstrates smoother transitions in joint torque, the general trends of torque increase and decrease closely match those observed in the experiment. Notably, the experimental data shows a more balanced torque distribution between the hip and knee joints, whereas the simulation results suggest a greater load carried by the knee joint. This distinction is further reflected in the power plot, where power generation in the simulation is dominated by the knee joint, while in the experiment, both the hip and knee contribute significantly.

Although the simulated torques are slightly lower than those measured experimentally, this difference may be partially attributed to Coulomb friction present in the physical system, which was not explicitly modeled in the simulation. The simulation uses a viscous friction coefficient of 5 Nms/rad, which may not capture the full resistive forces encountered in the joints. The real system's frictional effects could result in higher measured torques, especially during low-speed or direction-changing phases of motion. Despite this, the total actuator power required in the experiment is found to be lower than in the simulation, suggesting that the real system may achieve similar or improved dimensionless stiffness values compared to the simulated model. These findings support the hypothesis that the newly developed actuators could offer enhanced performance relative to existing state-of-the-art solutions.

6.1.6 Challenges in experiments

Several challenges arose during the experimental phase. Firstly, determining an appropriate maximum torque value proved difficult. A compromise had to be made between ensuring safety and providing sufficient acceleration to reach the desired joint velocities. Secondly, achieving consistent synchronization between the two leg segments was particularly challenging. Precise coordination is crucial for stable and symmetric movement.

6.2 Experimental setup DFKI

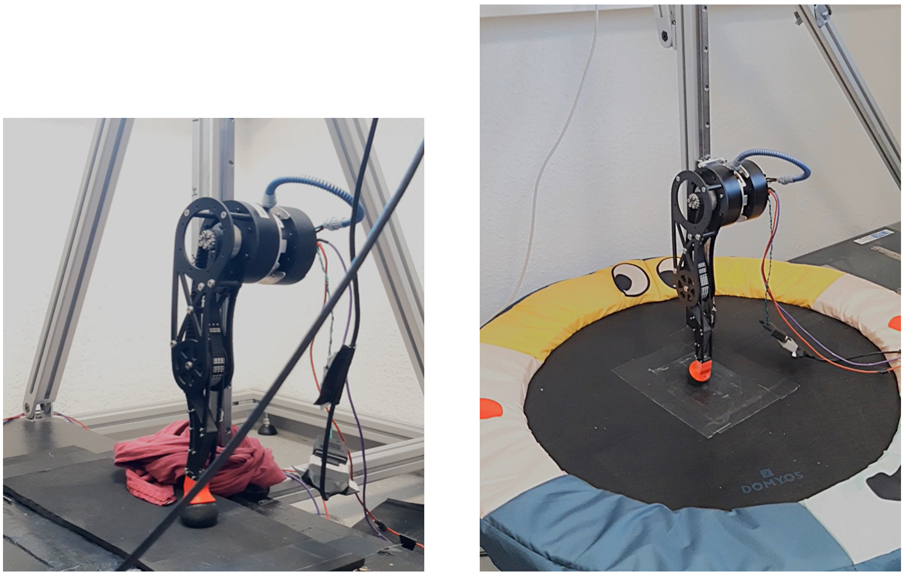

(a) Original setup

(b) Adapted setup

Figure 6.10: Different setups at DFKI

To validate the performance improvement provided by placing a spring (trampoline) under the foot, experiments were conducted using the setup at DFKI. The original DFKI configuration, shown in Figure 6.10a, consists of a single vertical rail supporting a hopper robot. The actuators used are two quasi-direct drives (*mjbots qdd100*) located at the hip, with motion transmitted to the knee joint via a belt. Communication between the actuators and the control system is handled through CAN cables.

Additionally, each actuator is equipped with a position encoder and a torque sensor. The model parameters for the DFKI hopper are listed in the second column of Table 3.1. The most notable parameters are the mass, which is equal to 2.32 kg, and the hopper height, which is equal to 0.29 m.

Since the setup lacks a linear encoder, absolute jumping heights could not be directly measured. However, visual markers were added to the rail at 5 cm intervals to provide a rough estimation of jumping height. This method was used to compare three different experimental configurations:

1. The hopper on the ground with the original energy shaping control algorithm, as described in [2].
2. The hopper on a trampoline but still using the ground control algorithm.
3. The hopper on the trampoline with a modified controller adapted to account for the trampoline dynamics.

Before conducting trampoline-based experiments, it was necessary to estimate the trampoline's stiffness. Two methods were used, as shown in Figure 6.11. In the first method (Figure 6.11a), large weights were placed on the trampoline, and deflection was measured. This yielded an almost linear deflection-mass relationship, suggesting that the trampoline behaves linearly. To confirm this in the operating range relevant to the 2.32 kg hopper, a second test using smaller weights was performed (Figure 6.11b). This method confirmed the linear behavior and yielded similar results. The estimated stiffness was 2564 N/m from the large-weight method and 2560 N/m from the precise method, as summarized in Figure 6.11c.

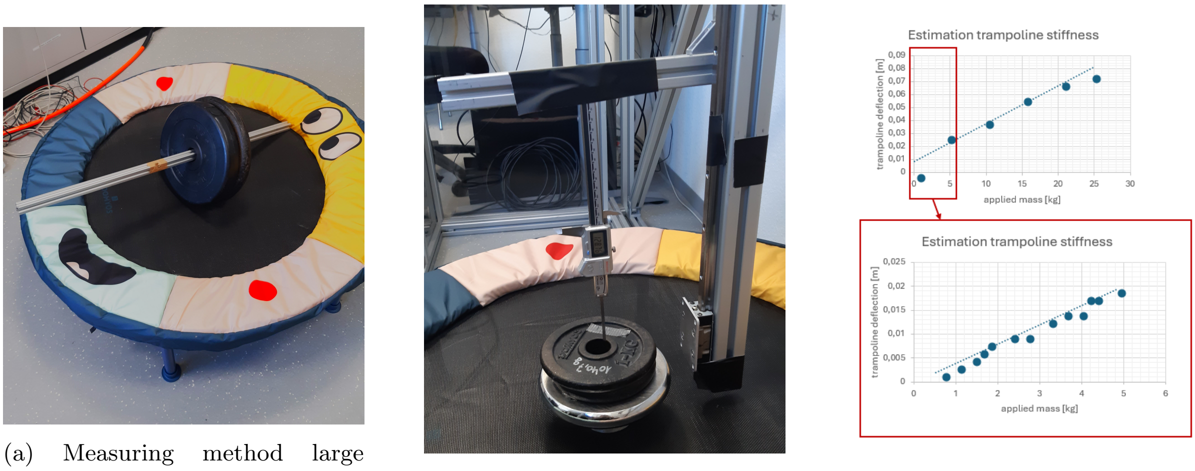

(a) Measuring method large weights

(b) Precise measuring method

(c) Stiffness estimation

Figure 6.11: Trampoline stiffness measurement methods

The results from the jumping experiments are displayed in Figure 6.12a and are as follows:

- On the ground with the original controller, the hopper achieved a maximum height of 30 cm, almost equal to its initial standing height.
- On the trampoline, using the same controller, the hopper reached 40 cm—a noticeable improvement.
- Finally, with the adapted control algorithm on the trampoline, a maximum jump height of 42.5 cm was achieved.

While the increase from 40 cm to 42.5 cm is modest, it still indicates a performance gain. This improvement is also visible in Figure 6.12b, where the hopper uses the ground-tuned controller for the first five jumps and the adapted trampoline controller for the last two. The increased jump heights in the final two jumps clearly illustrate the benefit of accounting for the trampoline in the control strategy.

However, the experiments were not without challenges. A notable issue was the discrepancy between the estimated and visually observed jumping heights. These inconsistencies, combined with challenges related to ground detection due to the lack of ground detection sensors, presented significant difficulties during testing.

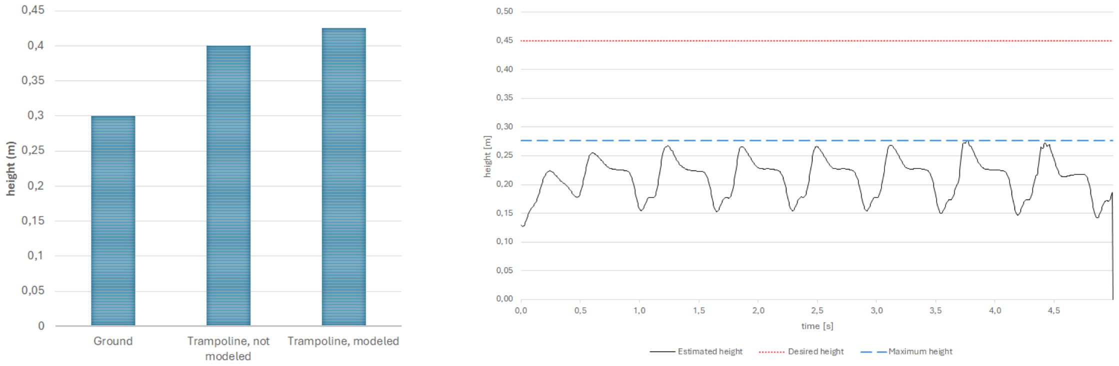

(a) Experimental results hopper DFKI

(b) Jumping heights trampoline experiment

Figure 6.12: Experimental results DFKI

Chapter 7

Future work

Future work could expand on several aspects of this master's thesis.

Firstly, improvements to the mechanical design may enhance performance and robustness. As discussed in Chapter 2, certain challenges regarding the sensing system remain and should be addressed in future iterations. Additionally, reinforcing the connection between the knee axis and the upper leg could reduce unwanted vibrations during the high-dynamic motions of hopping. Based on the results observed when using compliant ground surfaces, integrating a spring element into the foot could also be a promising design direction to further optimize energy storage and return. Furthermore, improving the rigidity of the linear rail attachment is expected to reduce the linear friction value, thereby enhancing system performance.

Secondly, future work should focus on completing the experimental validation of the simulated scenarios investigated in this thesis. In particular, experiments related to maximum drop height and continuous jumping could be further developed and executed to assess performance more comprehensively and verify the simulated predictions.

Lastly, future work could address the challenges encountered during the experiments, such as developing an improved state estimation method.

Chapter 8

Conclusion

This master's thesis presented the complete design and control process of a hopper robot, including the implementation of newly designed series clutched actuators. The work progressed from conceptual design, as outlined in Chapter 2, to the successful experimental validation of the system.

The proposed mechanical design, with a mass of 13.62 kg and height of 0.9 m, was fully assembled and validated through experiments. However, for future iterations, improvements are recommended in the mechanical integration of components. Specifically, a more robust method for attaching the contact switches to the foot should be considered, as well as a more stable connection between the knee axis and upper leg to ensure structural stiffness. Despite these minor challenges, the assembled design demonstrated reliable performance during testing.

The control strategy combined impedance control during touchdown, energy shaping during lift-off, and a PD controller for the flight phase. These were first implemented in simulation, allowing for thorough investigation of the effects of various control parameters. Simulations showed that lower values of the energy multiplication factor E_{mult} and lower friction coefficients led to increased jumping heights. Additionally, combinations of small flight angles, large start angles, and small foot offsets towards the knee resulted in lower normalized root mean square errors (NRMSE) between desired and achieved jumping heights. As expected from human jumping dynamics, achieving higher jumps required increased virtual leg stiffness and damping.

In continuous jumping simulations, jumping performance was found to vary significantly with rail friction. Thus, a definitive comparison to the state-of-the-art required an estimation of the linear rail friction. Using experimental data, an estimated linear rail friction value of 2.28 N s/m was determined. In simulations, this value corresponds to a maximum jumping height of 1.15 m and a maximum dimensionless jumping height of 1.28. Although this value is lower than some found in the literature—such as 2.4 in [4] and 1.57 in [3]—it still outperforms other setups, like the 1.14 reported in [19]. Therefore, it can be concluded that the linear rail friction must be reduced through improved assembly choices for the system to consistently surpass the state-of-the-art, though it already performs better than certain existing implementations.

When using only the impedance controller in simulation, a maximum dimensionless stiffness of 14.25 was achieved. This surpasses the current state-of-the-art value of 10.8, as reported in [14], indicating a meaningful improvement in actuator performance. Experimental validation of these simulation results was conducted via several tests. A position control experiment was compared to an impedance control simulation, showing similar torque profiles and lower power profiles, which supports the simulation claim of improved dimensionless stiffness.

Simulations involving a trampoline beneath the hopper showed that jumping height improved when the trampoline stiffness exceeded a certain threshold. While theory suggests an optimal stiffness exists (with the ground being the limiting case of infinite stiffness), numerical instability in the simulation made it challenging to identify this optimum. Experiments with the hopper placed on a trampoline confirmed this increase in jumping height when an elastic surface was used. This insight presents a potential avenue for future design enhancements, suggesting the inclusion of compliant elements under the foot could further improve performance.

To summarize, the answer to the research question "How to design an underactuated hopping leg moving in the 2-DOF plane based on in-house developed series clutched actuators, and how can the resulting hopper be controlled? Is the resulting leg more impact-resilient, and can it jump higher than the state-of-the-art?" is as follows:

> *The design of a hopper robot with series clutched actuators should prioritize low weight and low-inertia links while ensuring sufficient structural strength to withstand impacts during dynamic hopping motion. This can be achieved by positioning both actuators at the hip joint, using a rigid link to transmit motion, and enclosing the system in an aluminium frame with triangular cutouts to reduce mass.*
>
> *The resulting system can be controlled through multiple phases, each using a different control strategy: a PD controller for the flight phase, an impedance controller for the touchdown phase, and an energy-shaping controller for the lift-off phase. By combining this design and control architecture in simulations and experiments, several conclusions were drawn. First, due to a relatively high linear rail friction value of 2.28 N s/m, determined experimentally, the maximum dimensionless jumping height* $\bar{h} = 1.28$ *is moderate compared to the state-of-the-art, where [4] reports* $\bar{h} = 2.4$*, and [19] reports* $\bar{h} = 1.14$*.*
>
> *On the other hand, a significant improvement in dimensionless stiffness was observed, with the new design achieving a value of 14.25, compared to the state-of-the-art value of 10.8 in [14]. This suggests the proposed hopper design performs better during the touchdown phases of jumping, offering enhanced impact resilience. This conclusion is supported by experimental validation, further indicating the effectiveness of the proposed approach.*

Chapter 9

Societal reflection

This chapter provides a societal reflection on the work carried out during this master's thesis, including its potential applications. It covers sustainability considerations, ethical implications, and the alignment of the thesis with various Sustainable Development Goals (SDGs).

9.1 Sustainability considerations

The most significant impact on sustainability in this thesis lies in the design of the robotic system. Specifically, material choices and production methods were key factors that influenced the environmental footprint of the design.

9.1.1 Used materials

The majority of the components in the robot are made from aluminum. Although aluminum extraction is an energy-intensive process with a high carbon footprint, aluminum is highly recyclable. Nearly 100% of aluminum can be recycled, and the recycling process consumes far less energy than primary extraction. Furthermore, aluminum can be recycled indefinitely without any loss of quality. This makes aluminum an excellent material for sustainable product design.

While the specific aluminum used in the project may or may not have been previously recycled, all components of the design are recyclable at the end of the system's life cycle. This contributes to the overall sustainability of the design.

9.1.2 Production methods

The production of the robot components involved two primary manufacturing processes: laser cutting and turning.

Laser cutting is the more sustainable of the two methods. It generates minimal material waste due to its precision and efficiency. Furthermore, by cutting all components from the same plate, material waste was reduced even further. However, laser cutting does require significant power consumption, which is a consideration from an energy use perspective.

Turning, on the other hand, generates more material waste. Additionally, turning requires the use of water, which poses an environmental concern. Despite this, any leftover aluminum material can be recycled, thus minimizing waste.

9.1.3 Series clutched actuators

Another sustainable feature of the design is the use of series clutched actuators. These actuators include a decoupling system that protects the gearbox from impacts beyond its capacity. By incorporating this feature, the lifespan of the actuators is increased, reducing the risk of premature failure and electronic waste (e-waste). This contributes to the sustainability of the hopper system by extending its operational life.

9.2 Ethical considerations

The primary ethical considerations of this master's thesis revolve around the potential future applications of the technology, particularly in humanoid robots. The integration of humanoid robots into society could lead to significant ethical dilemmas.

On one hand, humanoid robots might replace human workers, potentially leading to job displacement. This raises concerns about the ethics of using robots to replace humans in certain industries, particularly if it leads to unemployment or social inequalities.

On the other hand, humanoid robots could be employed in roles that are hazardous or unhealthy for humans. For example, robots could perform tasks in dangerous environments, such as working in toxic environments or undertaking high-risk rescue missions. In these scenarios, humanoid robots could significantly reduce the risks to human workers and could help to save lives in emergency situations.

9.3 Links with Sustainable Development Goals (SDGs)

This thesis is closely linked to several Sustainable Development Goals (SDGs), which aim to promote a better and more sustainable world:

- SDG 9 - Industry, Innovation, and Infrastructure: The advancements made in the field of robotics through this thesis contribute to innovations in humanoid robot design and the broader field of robotics.
- SDG 12 - Responsible Consumption and Production: The use of aluminum, a highly recyclable material, ensures that the design is durable and minimizes waste. This supports more responsible consumption and production practices.
- SDG 8 - Decent Work and Economic Growth: The development of robotics opens new job opportunities in robotics-related industries. Furthermore, humanoid robots could help improve economic growth by taking on tasks that are dangerous or undesirable for human workers.

Chapter 10

Use of Generative AI in this master's thesis

During this master's thesis, Generative AI was used for five main purposes:

1. During the research phase of the thesis, ChatGPT and Copilot were utilized to assist in plotting methods and in selecting the most useful plots to extract meaningful information from.
2. During the experimental phase, ChatGPT helped with solving errors from the code.
3. During the writing phase, ChatGPT was employed to correct grammar and spelling mistakes in the written text.
4. During the writing phase, ChatGPT helped improve writing style.
5. During the writing phase, ChatGPT helped convert information into LaTeX writing style, such as tables and equations.

Bibliography

[1] Maximilian Albracht et al. “Model Predictive Parkour Control of a Monoped Hopper in Dynamically Changing Environments”. In: *IEEE Robotics and Automation Letters* 9.10 (Oct. 2024), pp. 8507–8514. ISSN: 2377-3766, 2377-3774. DOI: `10.1109/LRA.2024.3445668`. URL: `https://ieeexplore.ieee.org/document/10638672/` (visited on 10/11/2024).

[2] Raghav Soni et al. “End-to-End Reinforcement Learning for Torque Based Variable Height Hopping”. In: *2023 IEEE/RSJ International Conference on Intelligent Robots and Systems (IROS)*. 2023 IEEE/RSJ International Conference on Intelligent Robots and Systems (IROS). Detroit, MI, USA: IEEE, Oct. 1, 2023, pp. 7531–7538. ISBN: 978-1-6654-9190-7. DOI: `10.1109/IROS55552.2023.10342187`. URL: `https://ieeexplore.ieee.org/document/10342187/` (visited on 10/01/2024).

[3] Jinzhu Zhang et al. “Research on Bionic Jumping and Soft Landing of Single Leg System in Quadruped Robot”. In: *Journal of Bionic Engineering* 20.5 (Sept. 2023), pp. 2088–2107. ISSN: 1672-6529, 2543-2141. DOI: `10.1007/s42235-023-00360-y`. URL: `https://link.springer.com/10.1007/s42235-023-00360-y` (visited on 10/01/2024).

[4] Yanran Ding and Hae-Won Park. “Design and Experimental Implementation of a Quasi-Direct-Drive Leg for Optimized Jumping”. In: *2017 IEEE/RSJ International Conference on Intelligent Robots and Systems (IROS)*. 2017 IEEE/RSJ International Conference on Intelligent Robots and Systems (IROS). Vancouver, BC: IEEE, Sept. 2017, pp. 300–305. ISBN: 978-1-5386-2682-5. DOI: `10.1109/IROS.2017.8202172`. URL: `http://ieeexplore.ieee.org/document/8202172/` (visited on 10/01/2024).

[5] Jemin Hwangbo et al. “Cable-Driven Actuation for Highly Dynamic Robotic Systems”. In: *2018 IEEE/RSJ International Conference on Intelligent Robots and Systems (IROS)*. 2018 IEEE/RSJ International Conference on Intelligent Robots and Systems (IROS). Madrid: IEEE, Oct. 2018, pp. 8543–8550. ISBN: 978-1-5386-8094-0. DOI: `10.1109/IROS.2018.8593569`. URL: `https://ieeexplore.ieee.org/document/8593569/` (visited on 10/01/2024).

[6] Sangok Seok et al. “Actuator Design for High Force Proprioceptive Control in Fast Legged Locomotion”. In: *2012 IEEE/RSJ International Conference on Intelligent Robots and Systems*. 2012 IEEE/RSJ International Conference on Intelligent Robots and Systems (IROS 2012). Vilamoura-Algarve, Portugal: IEEE, Oct. 2012, pp. 1970–1975. ISBN: 978-1-4673-1736-8 978-1-4673-1737-5 978-1-4673-1735-1. DOI: `10.1109/IROS.2012.6386252`. URL: `http://ieeexplore.ieee.org/document/6386252/` (visited on 10/04/2024).

[7] Akash Singh, Navvab Kashiri, and Nikolaos Tsagarakis. “Design of a Quasi-Direct-Drive Actuator for Dynamic Motions”. In: *The 1st International Electronic Conference on Actuator Technology: Materials, Devices and Applications*. The 1st International Electronic Conference on Actuator Technology: Materials, Devices and Applications. MDPI, Nov. 21, 2020, p. 11. DOI: `10.3390/IeCAT2020-08516`. URL: `https://www.mdpi.com/2504-3900/64/1/11` (visited on 10/01/2024).

[8] Frederik Ostyn. “Impact-Resilient High Performance Robot Actuators via Lightweight Overload Clutch Design with Wedged Rollers”. In: *2024 IEEE-RAS 23rd International Conference on Humanoid Robots (Humanoids)*. 2024 IEEE-RAS 23rd International Conference on Humanoid Robots (Humanoids). Nancy, France: IEEE, Nov. 22, 2024, pp. 32–36. ISBN: 979-8-3503-7357-8. DOI: `10.1109/Humanoids58906.2024.10769823`. URL: `https://ieeexplore.ieee.org/document/10769823/` (visited on 12/13/2024).

[9] Joao Ramos et al. “Facilitating Model-Based Control Through Software-Hardware Co-Design”. In: *2018 IEEE International Conference on Robotics and Automation (ICRA)*. 2018 IEEE International Conference on Robotics and Automation (ICRA). Brisbane, QLD: IEEE, May 2018, pp. 566–572. ISBN: 978-1-5386-3081-5. DOI: `10.1109/ICRA.2018.8460575`. URL: `https://ieeexplore.ieee.org/document/8460575/` (visited on 10/02/2024).

[10] Gerardo Bledt et al. “MIT Cheetah 3: Design and Control of a Robust, Dynamic Quadruped Robot”. In: *2018 IEEE/RSJ International Conference on Intelligent Robots and Systems (IROS)*. 2018 IEEE/RSJ International Conference on Intelligent Robots and Systems (IROS). Madrid: IEEE, Oct. 2018, pp. 2245–2252. ISBN: 978-1-5386-8094-0. DOI: `10.1109/IROS.2018.8593885`. URL: `https://ieeexplore.ieee.org/document/8593885/` (visited on 10/25/2024).

[11] Youngwoo Sim and Joao Ramos. “Tello Leg: The Study of Design Principles and Metrics for Dynamic Humanoid Robots”. In: *IEEE Robotics and Automation Letters* 7.4 (Oct. 2022), pp. 9318–9325. ISSN: 2377-3766, 2377-3774. DOI: `10.1109/LRA.2022.3188122`. URL: `https://ieeexplore.ieee.org/document/9813569/` (visited on 11/16/2024).

[12] Jun He and Feng Gao. “Mechanism, Actuation, Perception, and Control of Highly Dynamic Multilegged Robots: A Review”. In: *Chinese Journal of Mechanical Engineering* 33.1 (Dec. 2020), p. 79. ISSN: 1000-9345, 2192-8258. DOI: `10.1186/s10033-020-00485-9`. URL: `https://cjme.springeropen.com/articles/10.1186/s10033-020-00485-9` (visited on 11/11/2024).

[13] Ryuki Sato et al. “Development of Robot Legs Inspired by Bi-Articular Muscle-Tendon Complex of Cats”. In: *2015 IEEE/RSJ International Conference on Intelligent Robots and Systems (IROS)*. 2015 IEEE/RSJ International Conference on Intelligent Robots and Systems (IROS). Hamburg, Germany: IEEE, Sept. 2015, pp. 1552–1557. ISBN: 978-1-4799-9994-1. DOI: `10.1109/IROS.2015.7353574`. URL: `http://ieeexplore.ieee.org/document/7353574/` (visited on 10/02/2024).

[14] Felix Grimminger et al. “An Open Torque-Controlled Modular Robot Architecture for Legged Locomotion Research”. In: *IEEE Robotics and Automation Letters* 5.2 (Apr. 2020), pp. 3650–3657. ISSN: 2377-3766, 2377-3774. DOI: `10.1109/LRA.2020.2976639`. URL: `https://ieeexplore.ieee.org/document/9015985/` (visited on 10/01/2024).

[15] Meng Yee Chuah and Sangbae Kim. “Enabling Force Sensing During Ground Locomotion: A Bio-Inspired, Multi-Axis, Composite Force Sensor Using Discrete Pressure Mapping”. In: *IEEE Sensors Journal* 14.5 (May 2014), pp. 1693–1703. ISSN: 1530-437X, 1558-1748. DOI: `10.1109/JSEN.2014.2299805`. URL: `http://ieeexplore.ieee.org/document/6714415/` (visited on 11/16/2024).

[16] “RABBIT: A Testbed for Advanced Control Theory”. In: *IEEE Control Systems* 23.5 (Oct. 2003), pp. 57–79. ISSN: 1066-033X, 1941-000X. DOI: `10.1109/MCS.2003.1234651`. URL: `https://ieeexplore.ieee.org/document/1234651/` (visited on 11/17/2024).

[17] Sangok Seok et al. “Design Principles for Energy-Efficient Legged Locomotion and Implementation on the MIT Cheetah Robot”. In: *IEEE/ASME Transactions on Mechatronics* 20.3 (June 2015), pp. 1117–1129. ISSN: 1083-4435, 1941-014X. DOI: `10.1109/TMECH.2014.2339013`. URL: `https://ieeexplore.ieee.org/document/6880316/` (visited on 11/05/2024).

[18] Frank Peuker, Andre Seyfarth, and Sten Grimmer. “Inheritance of SLIP Running Stability to a Single-Legged and Bipedal Model with Leg Mass and Damping”. In: *2012 4th IEEE RAS & EMBS International Conference on Biomedical Robotics and Biomechatronics (BioRob)*. 2012 4th IEEE RAS & EMBS International Conference on Biomedical Robotics and Biomechatronics (BioRob 2012). Rome, Italy: IEEE, June 2012, pp. 395–400. ISBN: 978-1-4577-1200-5 978-1-4577-1199-2 978-1-4577-1198-5. DOI: `10.1109/BioRob.2012.6290742`. URL: `http://ieeexplore.ieee.org/document/6290742/` (visited on 10/11/2024).

[19] Amin Khakpour Komarsofla, Ehsan Azadi Yazdi, and Mohammad Eghtesad. “Dynamic Modeling and Control of a Novel One-Legged Hopping Robot”. In: *Robotica* 39.9 (Sept. 2021), pp. 1692–1710. ISSN: 0263-5747, 1469-8668. DOI: `10.1017/S0263574720001447`. URL: `https://www.cambridge.org/core/product/identifier/S0263574720001447/type/journal_article` (visited on 10/25/2024).

Appendix A

Bill Of Materials (BOM)

ITEM NO.	PART NAME	DESCRIPTION	QTY.
1	CPGA	In house	2
2	LowerLeg	LaserCut	2
3	ProtectionFoot	3D-print	1
4	ConnectingRodsLowerLeg1	Buy	8
5	ContactSensorSupport	3D-print	1
6	Countersunk screw ISO 10642 M5x12 51060_050_012(High)	Buy/In house	46
7	KneeStabilityPart	Turning	1
8	Countersunk screw ISO 10642 M4x10 51060_040_010(High)	Buy/In house	16
9	TurningCircleHip	LaserCut	2
10	TurningRod	Turning	1
11	HipConnectorPlate	Turning	1
12a	LLTHCS15A1T0-82P5D011-BODY	-	4
12b	LLTHS15A1-82011-SUPPPLATE	-	8
12	LLTHZ15NIPPLE	Buy	4
15	LinearGuideRail	Buy	2
16	AlExtrusions	Buy	2
17	M8ShoulderBolt1	Buy	2
18	Glijschijf	Buy	4
19	LegHip	LaserCut	1
20	LegHip - kopie	LaserCut	1
21	ConnectingRodsUpperLeg	Buy	15
22	weightblock	Turning	1
23	WeightRod	In house	1
24	Cylinder head screw DIN 912 M5x22 51050_050_022(High)	Buy/In house	6
25	Cylinder head screw DIN 912 M5x14 51050_050_014(High)	Buy/In house	12
26	Cylinder head screw DIN 912 M6x20 51050_060_020(High)	Buy/In house	16

27	Hexagon head screws ISO 4014 (DIN 931) M5x40 55000_050_040(High)	Buy/In house	16
28	SpacerHip	Turning	2
29	Countersunk screw ISO 10642 M5x25 51060_050_025(High)	Buy/In house	16
30	SpacerHip5mm	LaserCut	3
31	Countersunk screw ISO 10642 M5x14 55060_050_014(High)	Buy/In house	12
32	Bushing101212	Buy	2
33	Hexagon nut DIN 934 M8 01300_080_001(High)	Buy/In house	2
34	ibh_H1FM-1416-12_20241210_161_model	Buy	2
35	Axis	Turning	1
36	Countersunk screw ISO 10642 M8x18 55060_080_018(High)	Buy/In house	2
37	Hexagon nut DIN 934 M4 01300_040_001(High)	Buy/In house	3
38	Hexagon bolts ISO4017_DIN933 M4x12 51010_040_012 (High)	Buy/In house	3
39	ContactSensor	Buy	1

Appendix B

Parts drawing

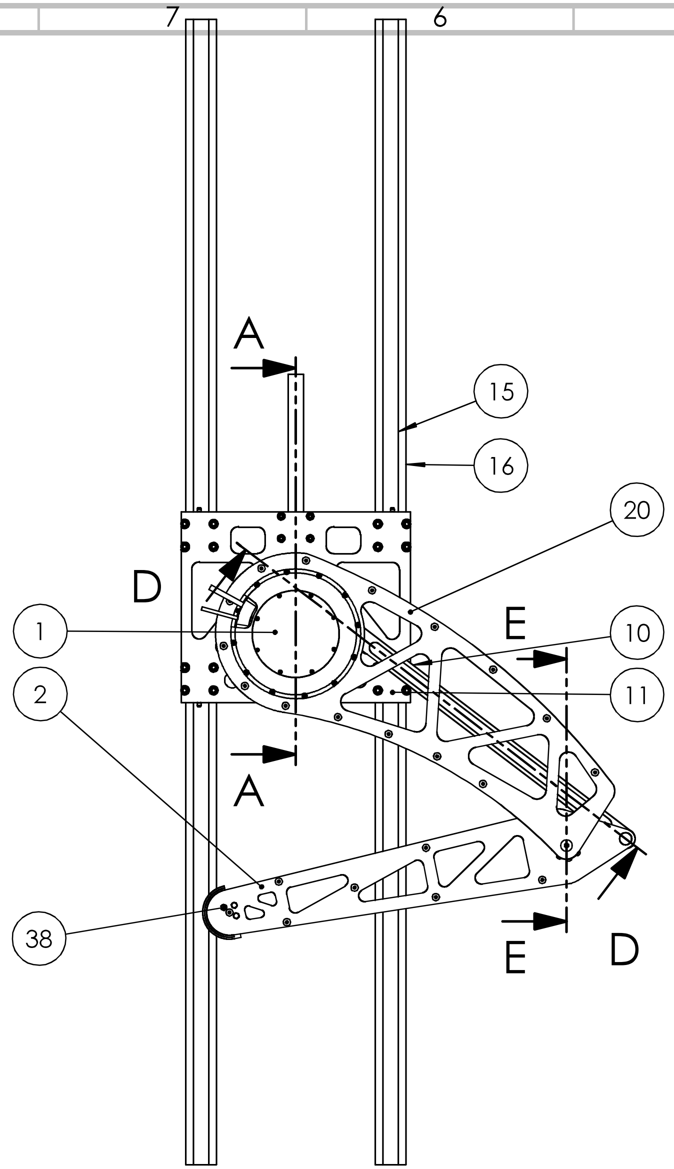

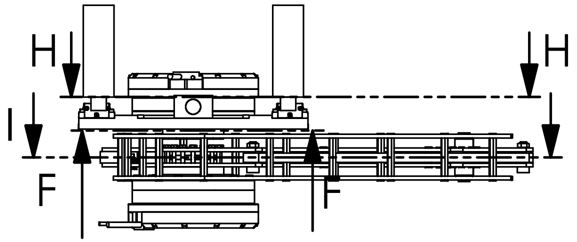

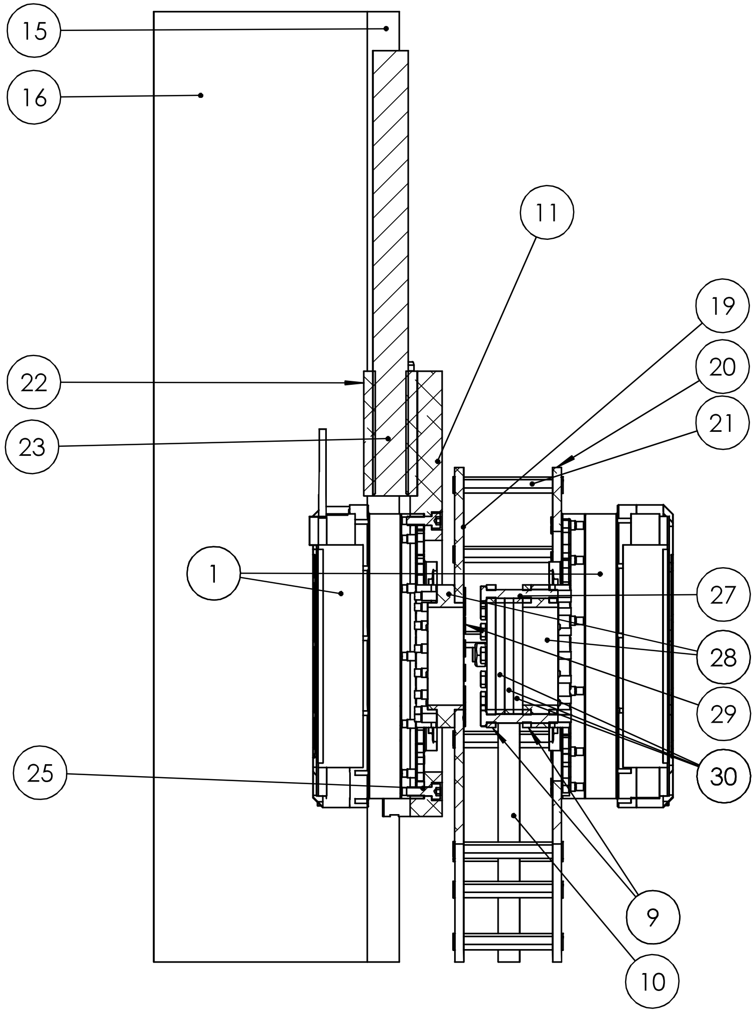

SECTION A-A

SCALE 1 : 3

MACHINING: ISO 2768-mH
WELDING: ISO 13920-BF
BENDING: DIN 6935

THIS DRAWING IS PROPERTY OF GHENT UNIVERSITY, NO REPRODUCTION OR ACCESS TO THIRD PARTY IS ALLOWED WITHOUT WRITTEN PERMISSION

DEBURR AND BREAK SHARP EDGES

FINISH:

	DESIGN	DATE	COMMENT
A	FOST		
B			
C			
D			

TITLE:

WEIGHT:

MATERIAL:

DWG NO.

Leg

REV.
A

SCALE:1:1

SHEET 1 OF 4

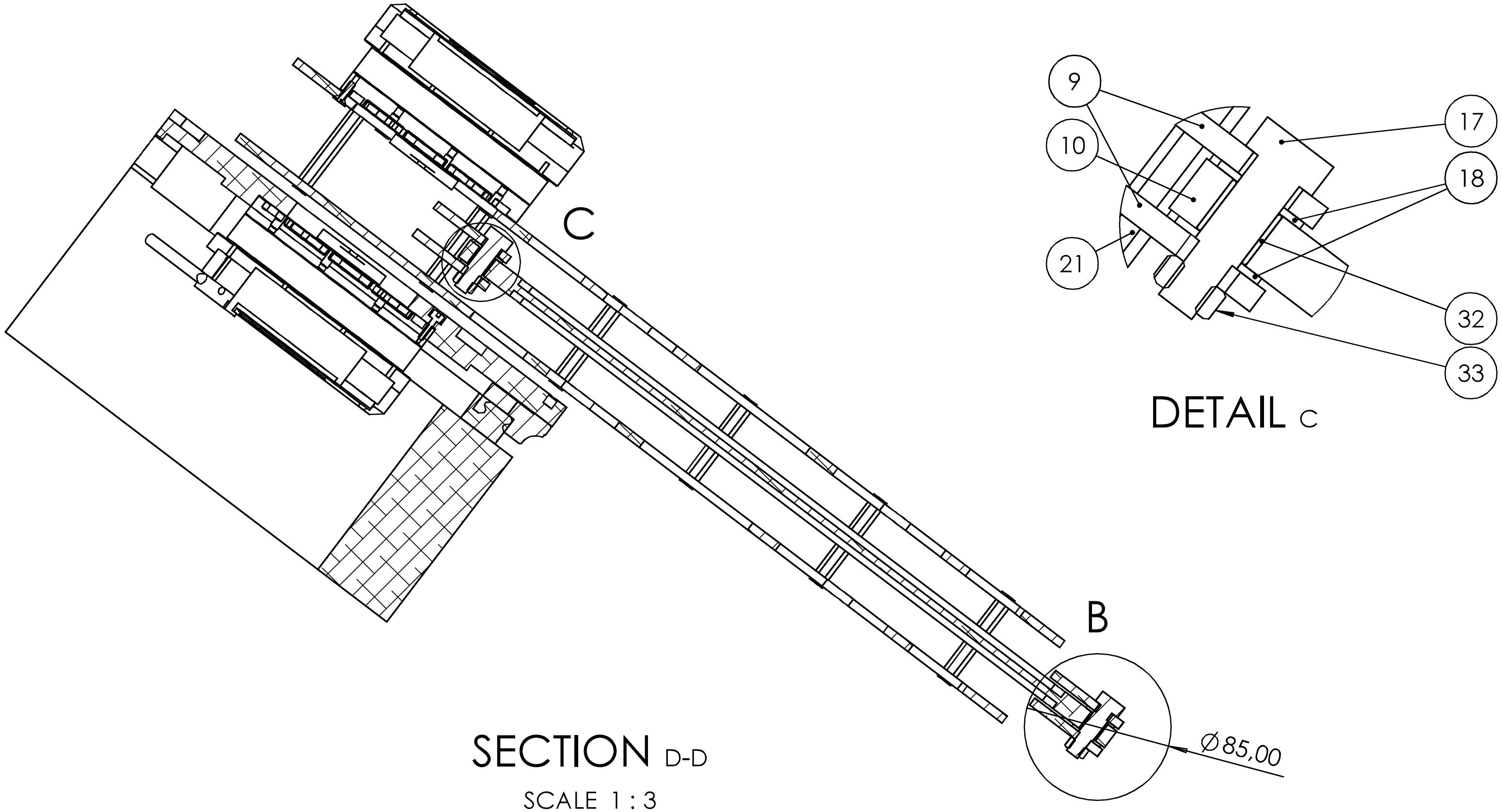

SECTION D-D
SCALE 1 : 3

DETAIL C

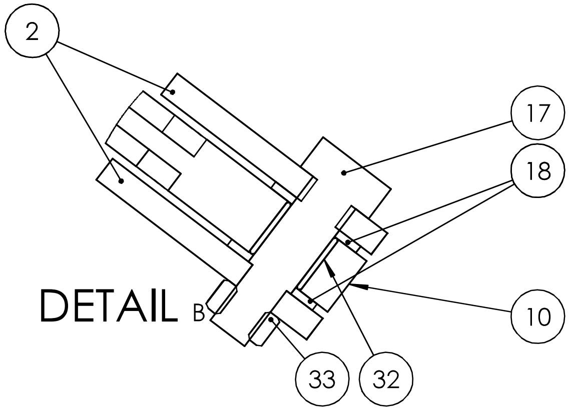

DETAIL B

MACHINING: ISO 2768-mH WELDING: ISO 13920-BF BENDING: DIN 6935	THIS DRAWING IS PROPERTY OF GHENT UNIVERSITY, NO REPRODUCTION OR ACCESS TO THIRD PARTY IS ALLOWED WITHOUT WRITTEN PERMISSION	DEBURR AND BREAK SHARP EDGES	FINISH:

	DESIGN	DATE	COMMENT
A	FOST		
B			
C			
D			

TITLE:

WEIGHT:

MATERIAL:

DWG NO.

Leg

REV.
A

SCALE:1:1

SHEET 2 OF 4

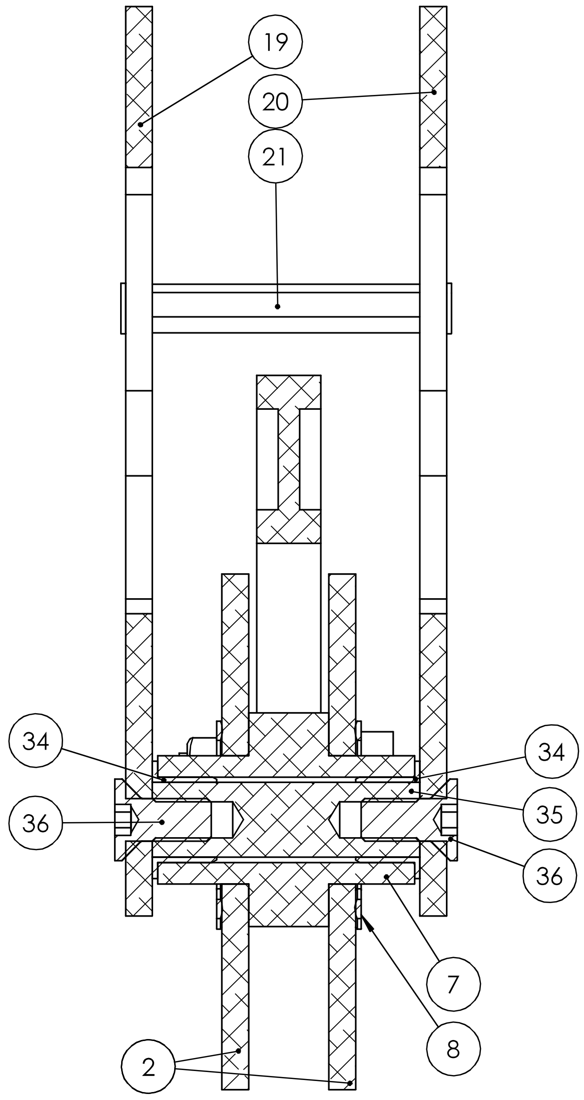

SECTION E-E

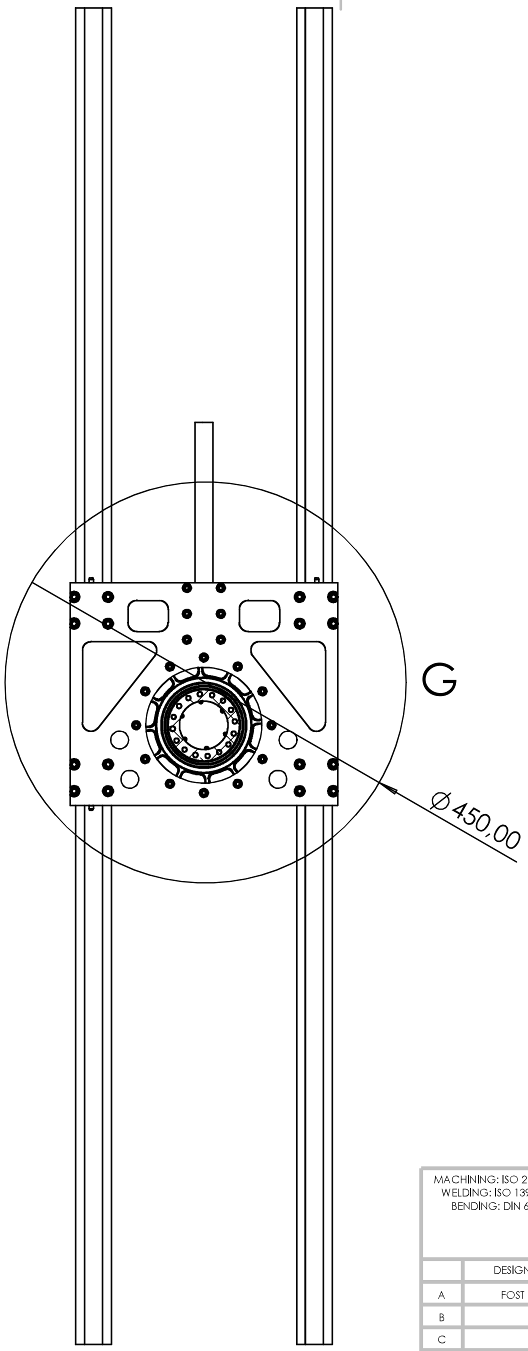

SECTION F-F

SCALE 1 : 6

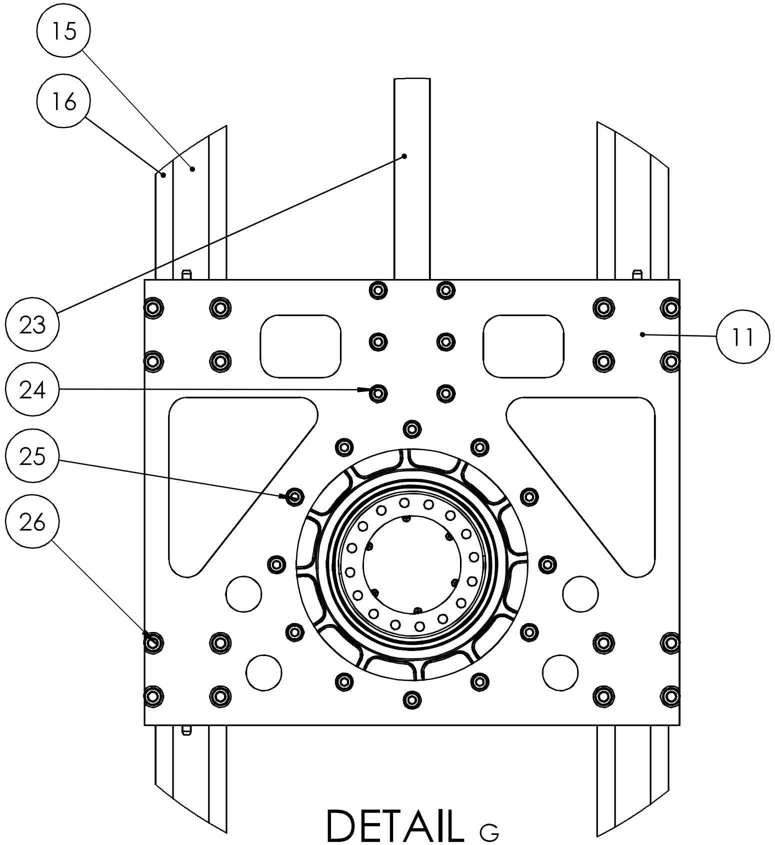

DETAIL G

SCALE 1 : 3

MACHINING: ISO 2768-mH WELDING: ISO 13920-BF BENDING: DIN 6935	THIS DRAWING IS PROPERTY OF GHENT UNIVERSITY, NO REPRODUCTION OR ACCESS TO THIRD PARTY IS ALLOWED WITHOUT WRITTEN PERMISSION	DEBURR AND BREAK SHARP EDGES	FINISH:

	DESIGN	DATE	COMMENT
A	FOST		
B			
C			
D			

TITLE:

WEIGHT:

MATERIAL:

DWG NO.

Leg

REV.
A

SCALE:1:1

SHEET 3 OF 4

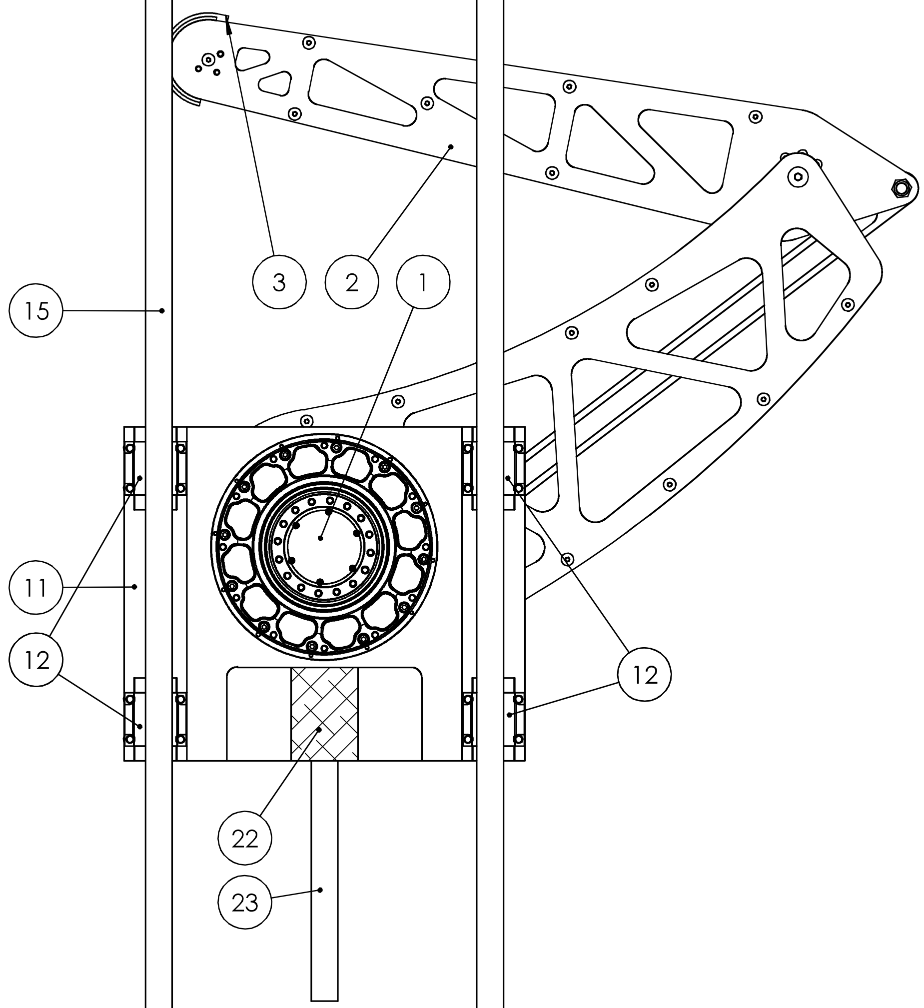

SECTION H-H

SCALE 1 : 4

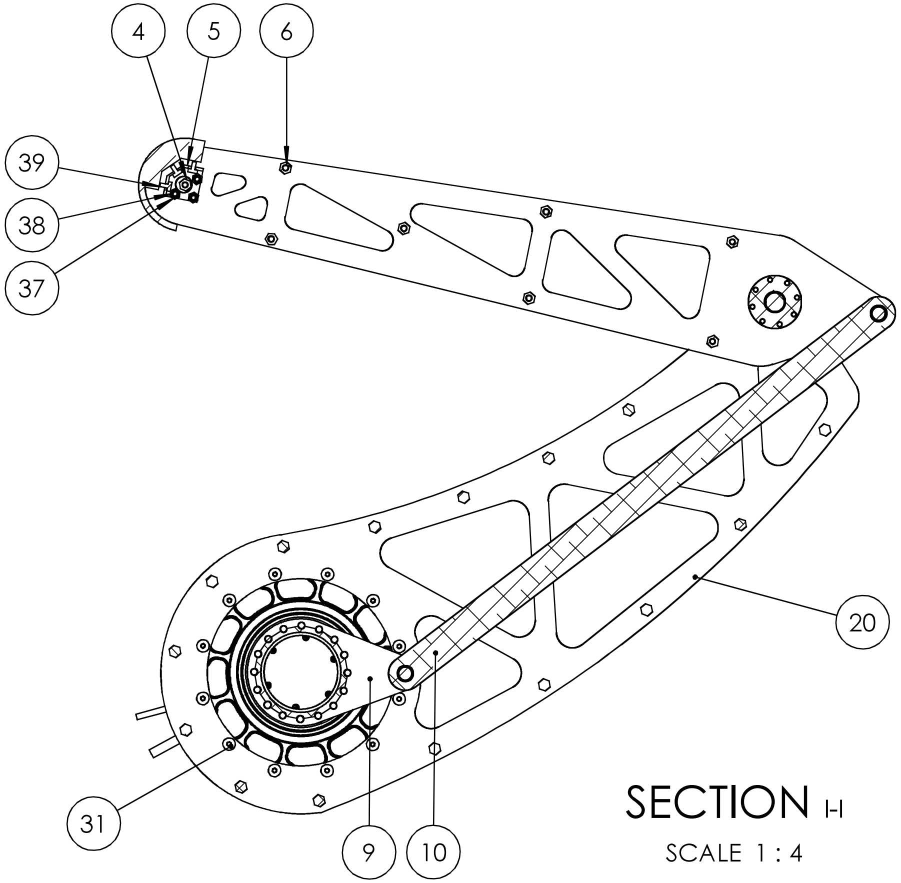

SECTION I-I

SCALE 1 : 4

MACHINING: ISO 2768-mH
WELDING: ISO 13920-BF
BENDING: DIN 6935

THIS DRAWING IS PROPERTY OF GHENT UNIVERSITY, NO REPRODUCTION OR ACCESS TO THIRD PARTY IS ALLOWED WITHOUT WRITTEN PERMISSION

DEBURR AND BREAK SHARP EDGES

FINISH:

	DESIGN	DATE	COMMENT
A	FOST		
B			
C			
D			

TITLE:

WEIGHT:

MATERIAL:

DWG NO.

Leg

REV.
A

SCALE:1:1

SHEET 4 OF 4

Appendix C

Technical drawing - hip base

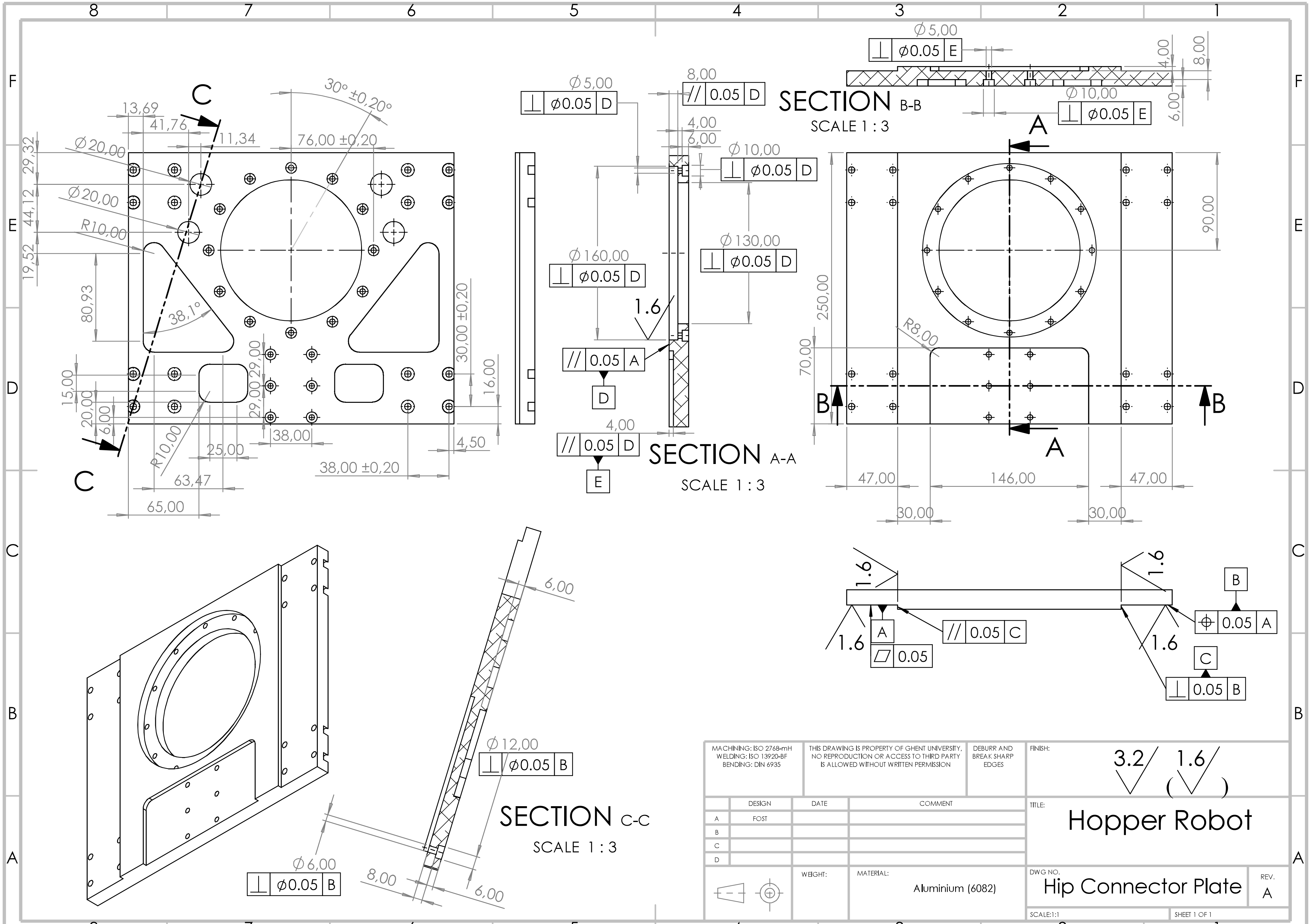

MACHINING: ISO 2768-mH
WELDING: ISO 13920-BF
BENDING: DIN 6935

THIS DRAWING IS PROPERTY OF GHENT UNIVERSITY, NO REPRODUCTION OR ACCESS TO THIRD PARTY IS ALLOWED WITHOUT WRITTEN PERMISSION

DEBURR AND BREAK SHARP EDGES

FINISH: 3.2 (1.6)

	DESIGN	DATE	COMMENT
A	FOST		
B			
C			
D			

TITLE: Hopper Robot

WEIGHT:

MATERIAL: Aluminium (6082)

DWG NO. Hip Connector Plate

REV. A

SCALE:1:1

SHEET 1 OF 1

Appendix D

Technical drawing - weight block

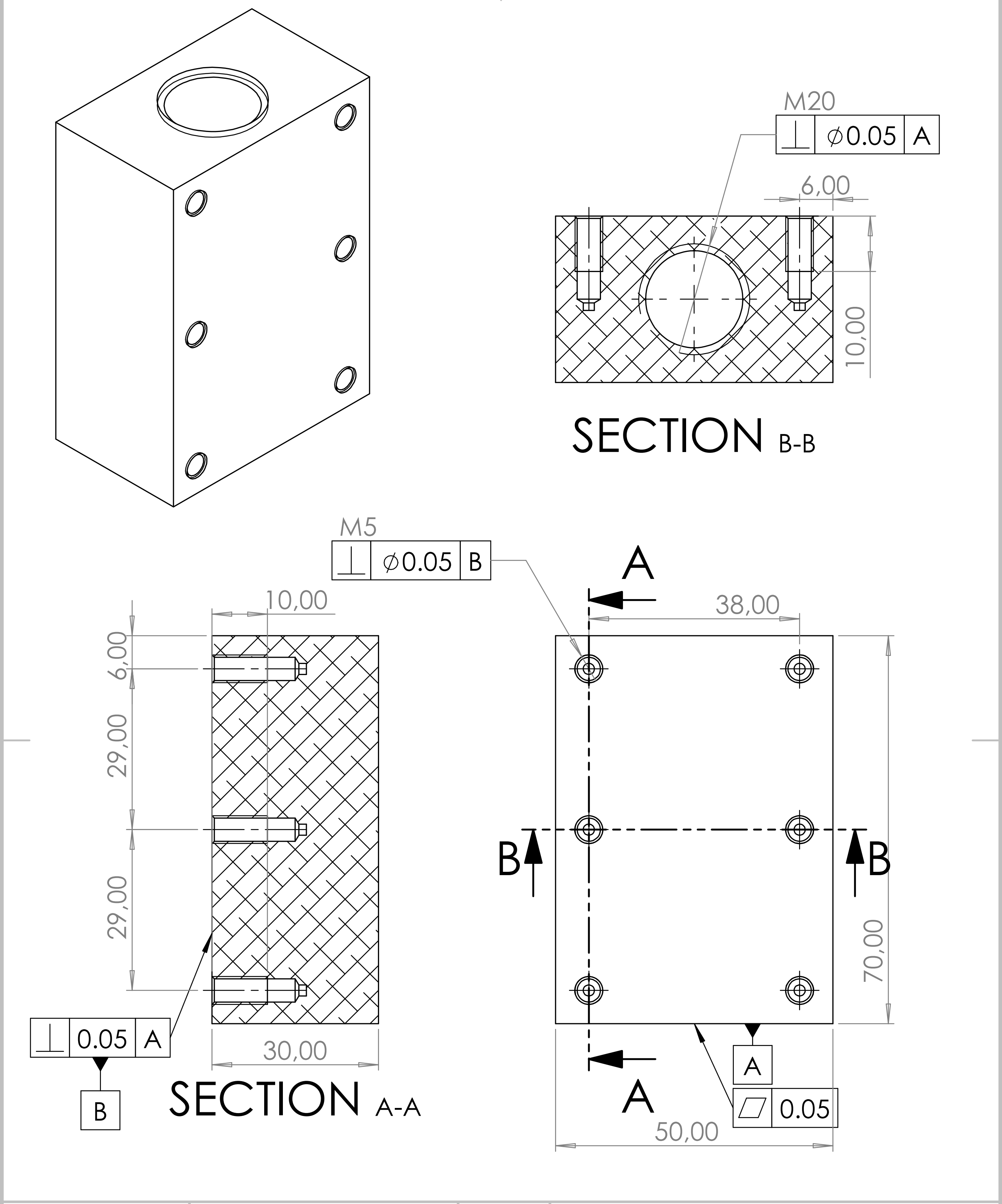

MACHINING: ISO 2768-mH
WELDING: ISO 13920-BF
BENDING: DIN 6935

PROPERTY OF GHENT UNIVERSITY, NO REPRODUCTION OR ACCES TO THIRD PARTY IS ALLOWED WITHOUT WRITTEN PERMISSION

DEBURR AND BREAK SHARP EDGES

FINISH: 3.2

REV.	DESIGN	DATE	COMMENT
A	FOST		NEW DRAWING
B			
C			
D			

TITLE: Hopper Robot

WEIGHT:

MATERIAL: Aluminium (6082)

DWG NO. weightblock

REV. A

SCALE:1:1

SHEET 1 OF 1

Appendix E

Technical drawing - hip spacer

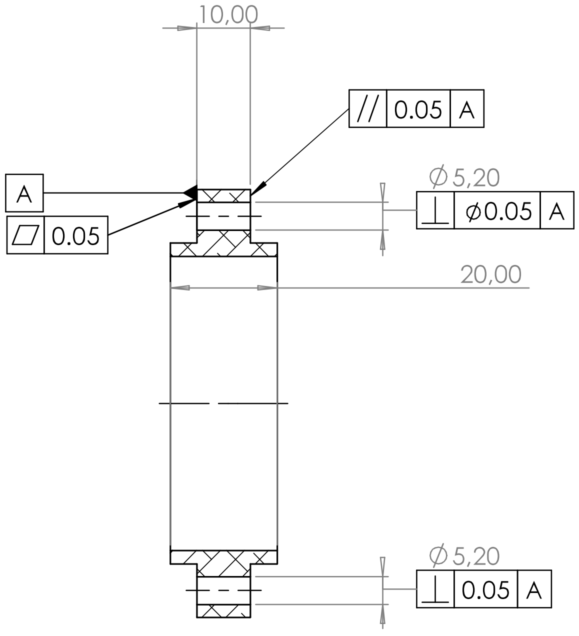

SECTION A-A

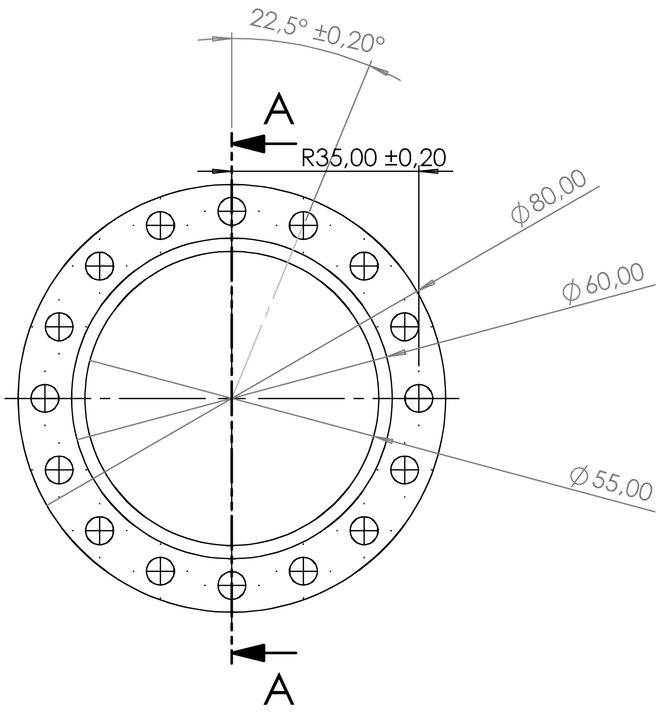

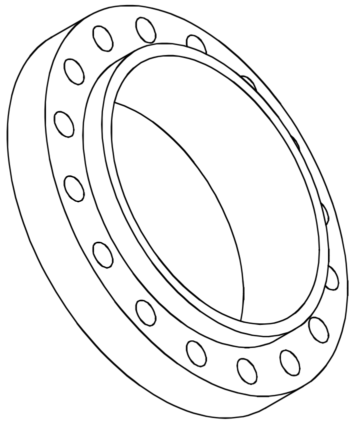

MACHINING: ISO 2768-mH WELDING: ISO 13920-BF BENDING: DIN 6935	THIS DRAWING IS PROPERTY OF GHENT UNIVERSITY, NO REPRODUCTION OR ACCESS TO THIRD PARTY IS ALLOWED WITHOUT WRITTEN PERMISSION	DEBURR AND BREAK SHARP EDGES	FINISH: 3.2

	DESIGN	DATE	COMMENT
A	FOST		
B			
C			
D			

TITLE: Hopper Robot

WEIGHT:

MATERIAL: Aluminium (6082)

DWG NO. SpacerHipDrawing

REV. A

SCALE:1:1

SHEET 1 OF 1

Appendix F

Technical drawing - turning rod

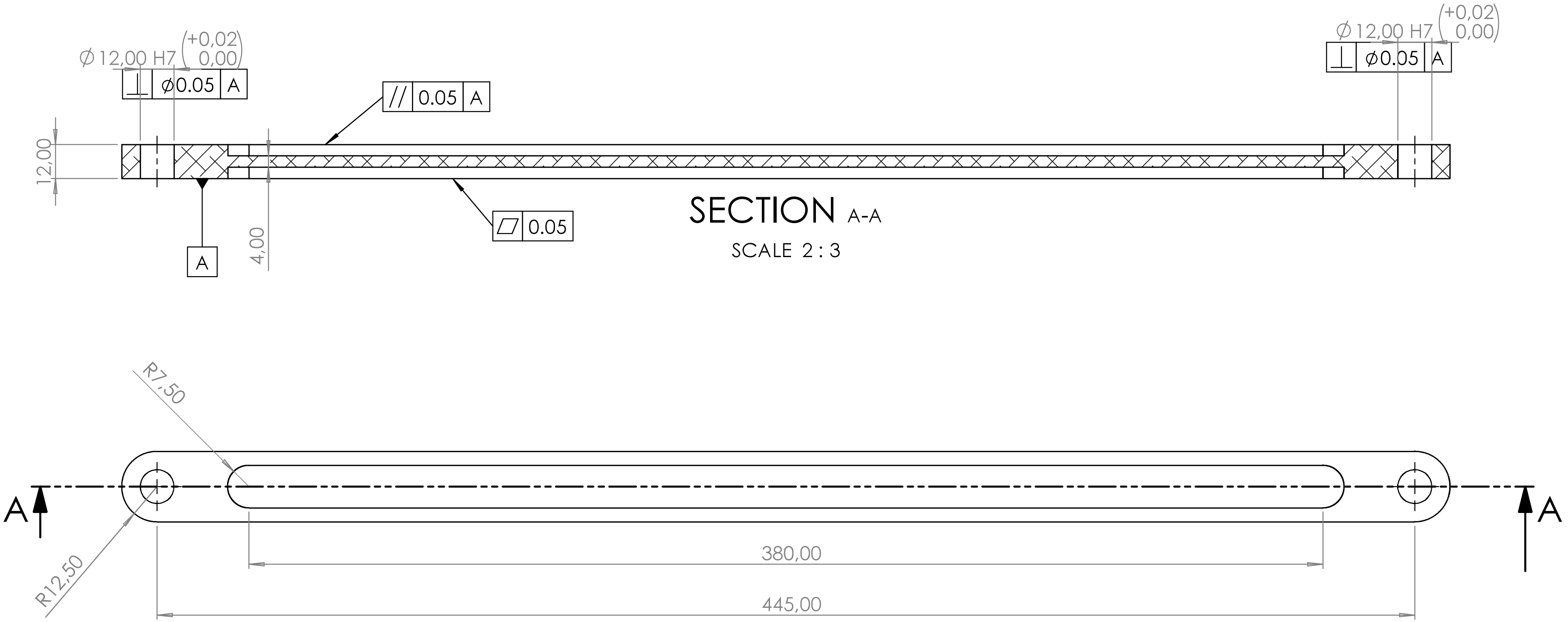

SECTION A-A
SCALE 2 : 3

MACHINING: ISO 2768-mH
WELDING: ISO 13920-BF
BENDING: DIN 6935

THIS DRAWING IS PROPERTY OF GHENT UNIVERSITY, NO REPRODUCTION OR ACCESS TO THIRD PARTY IS ALLOWED WITHOUT WRITTEN PERMISSION

DEBURR AND BREAK SHARP EDGES

FINISH: 3.2

	DESIGN	DATE	COMMENT
A	FOST		
B			
C			
D			

TITLE:
Hopping Robot

WEIGHT:

MATERIAL:
Aluminium (6082)

DWG NO.
TurningRod

REV.
A

SCALE:2:3

SHEET 1 OF 1

Appendix G

Technical drawing - knee axis

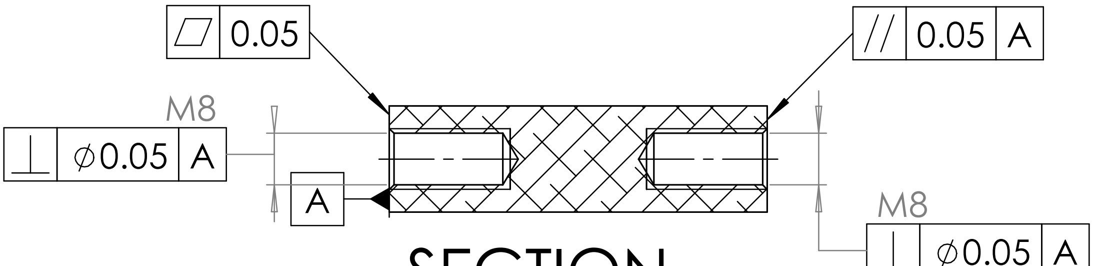

SECTION A-A

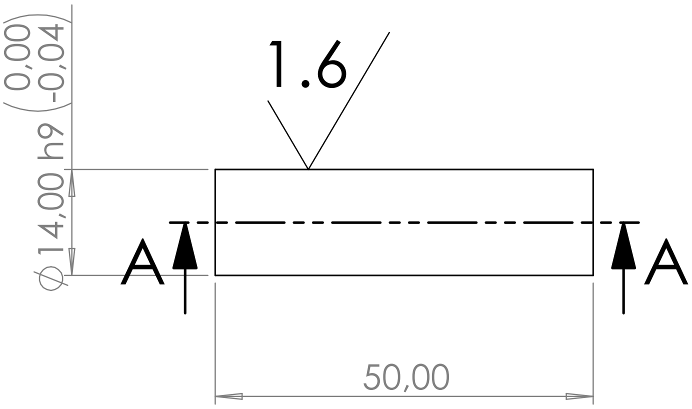

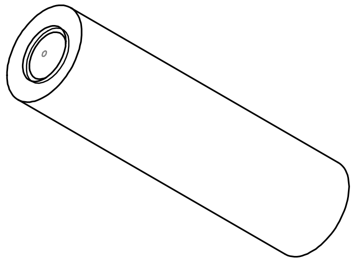

MACHINING: ISO 2768-mH WELDING: ISO 13920-BF BENDING: DIN 6935	PROPERTY OF GHENT UNIVERSITY, NO REPRODUCTION OR ACCES TO THIRD PARTY IS ALLOWED WITHOUT WRITTEN PERMISSION	DEBURR AND BREAK SHARP EDGES	FINISH: 3.2 (1.6)

REV.	DESIGN	DATE	COMMENT
A	FOST		NEW DRAWING
B			
C			
D			

TITLE: Hopper Robot

WEIGHT:

MATERIAL: Aluminium (6082)

DWG NO. Axis

REV. A

SCALE:1:1

SHEET 1 OF 1

Appendix H

Technical drawing - knee stability part

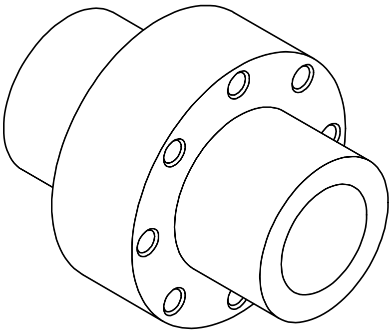

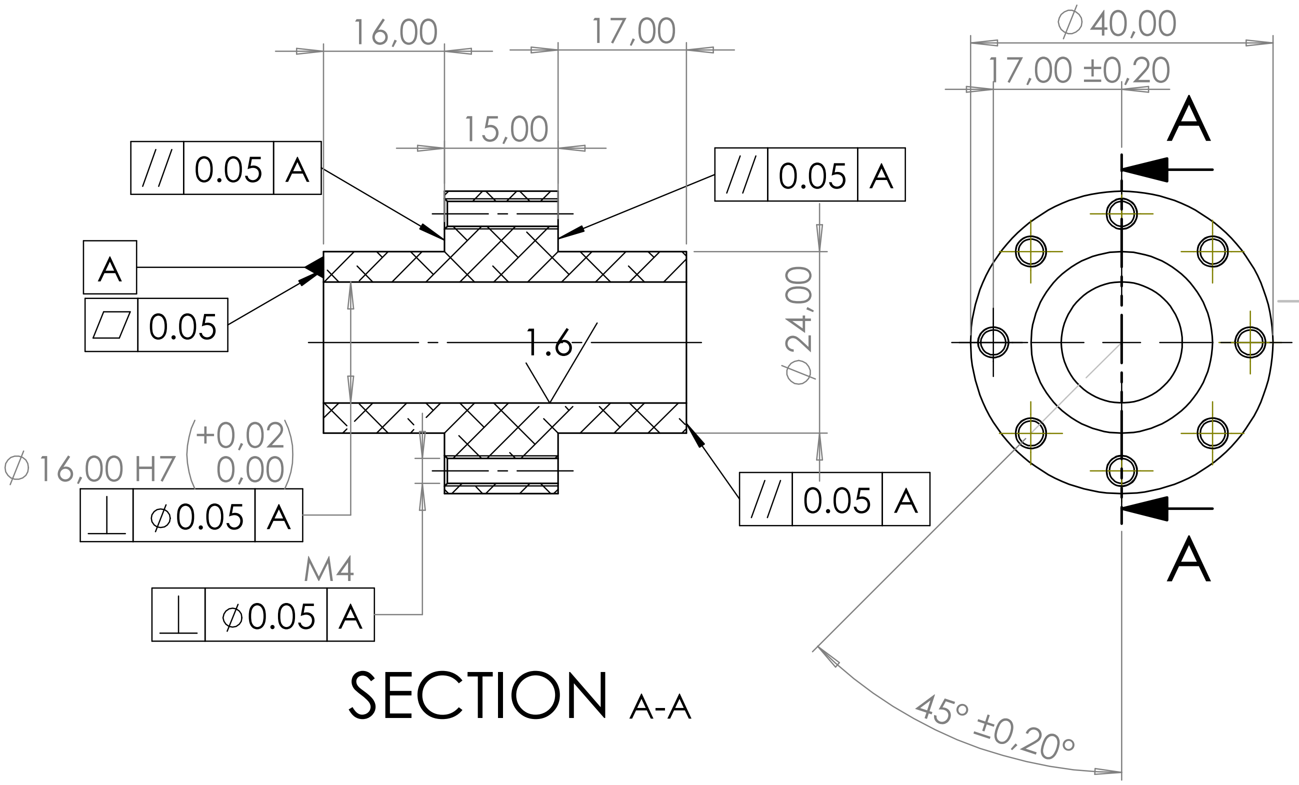

SECTION A-A

MACHINING: ISO 2768-mH WELDING: ISO 13920-BF BENDING: DIN 6935	PROPERTY OF GHENT UNIVERSITY, NO REPRODUCTION OR ACCES TO THIRD PARTY IS ALLOWED WITHOUT WRITTEN PERMISSION	DEBURR AND BREAK SHARP EDGES	FINISH: 3.2 (1.6)

REV.	DESIGN	DATE	COMMENT
A	FOST		NEW DRAWING
B			
C			
D			

TITLE: Hopper Robot

WEIGHT:

MATERIAL: Aluminium (6082)

DWG NO. KneeStabilityPart

REV. A

SCALE:1:1

SHEET 1 OF 1